THE UNIVERSITY *of* EDINBURGH

Analysis of Laboratory and Field Measurements of Directionally Spread Nonlinear Ocean Waves

Mark Laing McAllister

THE UNIVERSITY
of EDINBURGH

Thesis submitted in fulfilment of
the requirements for the degree of
Doctor of Philosophy
to the
University of Edinburgh — 2017

Declaration

I declare that this thesis has been composed solely by myself and that it has not been submitted, either in whole or in part, in any previous application for a degree. Except where otherwise acknowledged, the work presented is entirely my own.

Mark Laing McAllister

October 2017

Abstract

Surface gravity waves exist in the oceans as multi-directional nonlinear phenomena. Understanding how these two properties interact is intrinsically important in itself. Furthermore, an understanding of this relationship may be used to gain insight into other oceanic phenomena. This thesis first describes an experimental investigation into the relationship between directionality and non-linearity (Part I). This relationship was then used as a tool to estimate the directional spreading of field data (Part II).

Experiments have been conducted in which directionally spread focused wave groups were created in a wave tank. The relationship between the degree of directional spreading and the second-order bound harmonics of the wave groups was examined, in particular the formation of a 'set-up'. These measurements were then compared to predictions from second-order theories, finding good agreement. The two-dimensional structure of the bound waves was explored giving new insight into the underlying physics. Experiments were then carried out for directionally spread crossing wave groups. It is believed that the crossing of two sufficiently separated wave groups may be the cause of an anomalous set-up in the second-order bound waves observed for some extreme and potentially freak waves. This set-up is reproduced experimentally. Again, the results of these test agreed very well when compared to second-order theory.

The insight gained from the foregoing experiments was then utilised in the analysis of field data. A method, which requires only a single measurement to estimate the observed degree of directional spreading, was applied to a large dataset of field measurements from the North Alwyn platform in the North Sea. This method was then compared to conventional approaches, which require multiple concurrent measurements. The method that requires only a single measurement was shown to be effective, and presents a promising approach to gaining additional insight about the directional spreading of point observations.

Acknowledgements

Firstly, I must acknowledge my supervisors; Dr Vengatesen Venugopal, Professor Alistair Borthwick, and Dr Ton van den Bremer, who each played pivotal roles in my PhD. Thanks to Venki, for granting me with this opportunity, and your continued support and guidance throughout the duration of my studies. I would like to thank Alistair for his help with work carried out in Part II, his wise words, and endeavours to improve my grammar. I would like to thank, Ton for his invaluable involvement in the work carried out in Part I, and for helping secure the funding for the experimental testing at FloWave. The FloWave facility was funded by the UK's Engineering and Physical Sciences Research Council under grant EP/I02932X/1. I have also received support and help from many of my colleagues within the Institute for Energy Systems, to whom I am exceptionally grateful.

I would also like to extend my gratitude to Professors Paul Taylor and Tom Adcock of the University of Oxford, for their collaboration in the work carried out in Chapter Part I, and for providing me with the potential flow data used for validation in Chapter 2. It would not have been possible to carry out the experiments in Part I with such success without the help of Dr Sam Draycott, Dr Tom Davey, and the staff at FloWave. Finally I would like to thank my parents, family, and friends for their support during my studies.

Contents

List of Tables

List of Figures

Acronyms

BBC	Bottom Boundary Condition.
CDIP	Coastal Data Information Program.
DFSBC	Dynamic Free Surface Boundary Condition.
ECMWF	European Centre for Medium-Range Weather Forecasts.
FFT	Fast Fourier Transform.
FRF	Field Research Facility.
IMLM	Iterative Maximum Likelihood Method.
IOC	International Ocean Commission.
IOOS	Integrated Ocean Observing System.
JONSWAP	Joint North Sea Wave Project.
KFSBC	Kinematic Free Surface Boundary Condition.
LWM	Long-Wave Method.
NAA	North Alwyn A.
NAB	North Alwyn B.
NW	New Wave.
QARTOD	Qauality Assurance of Real Time Ocean Data.
RMS	Root-Mean-Squared.

Nomenclature

A	Amplitude envelope function	(m).
a	Wave amplitude	(m).
a_0	Amplitude at focus	(m).
a^-	Amplitude of difference waves	(m).
a^+	Amplitude of sum waves	(m).
$\bar{a}$	RMS amplitude	(m).
a_{MP}	Maximum probable amplitude	(m).
B	Self interaction kernel.	
B^+	Difference interaction kernel.	
B^-	Sum interaction kernel.	
$c_{g,0}$	Group velocity	(ms^{-1}).
D	Frequency independent spreading function.	
F	Mean flow forcing	(ms^{-1}).
f_p	Peak frequency	(Hz).
g	Gravity	(ms^{-2}).
H	Wave Height	(m).
h	Water depth	(m).
H_s	Significant wave height	(m).
k	Wavenumber magnitude $k = \lvert\mathbf{k}\rvert$	(m^{-1}).
$\mathbf{k}$	Wavenumber vector	(m^{-1}).
k_0	Carrier wavenumber	(m^{-1}).
N_z	Number of zero-crossing waves.	
R	Wave group aspect ratio.	
S	Amplitude spectrum	(m).

S_{22}	Stokes parameter.	
S_y	Quality control, limiting rate of change (ms^{-1}).	
T	Wave period	(s).
t	Time	(s).
T_p	Peak period	(s).
T_z	Zero-crossing mean period	(s).
$\mathbf{x}$	Position vector	(m).
x	Stream-wise Cartesian coordinate	(m).
y	Span-wise Cartesian coordinate	(m).
z	Vertical Cartesian coordinate	(m).
α	Wave steepness.	
γ	Skewness.	
Δk	Wavenumber spectral bandwidth parameter (m^{-1}).	
Δ_{lw}	Long wave difference.	
$\Delta\theta$	Crossing angle	(.deg).
$\Delta\sigma_\theta^\star$	Error in spreading estimation	(.deg).
$\Delta\eta_{I-IV}$	Estimated sources of error in experiments	(m).
ϵ	Group bandwidth parameter.	
η	Free surface elevation	(m).
η_0	Crest-focused free surface elevation	(m).
η_{180}	Trough-focused free surface elevation	(m).
η_{even}	Harmonic components of even powers	(m).
$\eta^{(1)}$	Linear free surface elevation	(m).
η_{odd}	Harmonic components of odd powers	(m).
$\eta_+^{(2)}$	Second-order sum terms	(m).
$\eta_-^{(2)}$	Second-order difference terms	(m).
θ_0	Mean wave direction	(.deg).
μ	Sample mean.	
ρ	Correlation coefficient.	
σ	Standard deviation.	
σ_θ	Degree of directional spreading	(.deg).
σ_x	Real space group bandwidth parameter	(m).
σ_y	Real space orthogonal group bandwidth parameter	(m).
φ	Phase	(rad).
$\boldsymbol{\phi}$	Velocity potential	($\mathrm{m}^2\mathrm{s}^{-1}$).
ω	Natural frequency	(rad s^{-1}).

ω_0	Carrier wave frequency	(m^{-1}).

Chapter 1

Introduction

1.1 Background

Much of our understanding of ocean gravity waves is built upon unidirectional, and often linear wave theories. In the laboratory it is only possible to model fully waves that travel in all directions in a small number of specialist test facilities, and the numerical modelling of fully nonlinear fully directional waves is a complex task, which can be difficult to validate. Waves in the oceans are composed of components propagating in all directions. For small amplitude waves, multidirectional conditions can be expressed as a linear superposition of multiple unidirectional wave components [Airy, 1841]. However, as waves become large they become nonlinear and this is no longer the case as. This nonlinearity can be expressed as a Stokes-type perturbation expansion in steepness $\alpha = a|\mathbf{k}|$ where the free surface elevation is decomposed into a series of terms of increasing order [Stokes, 1847]:

$$\eta = \eta^{(1)} + \alpha\eta^{(2)} + \alpha^2\eta^{(3)} + \cdots + \alpha^{j-1}\eta^{(j)}. \tag{1.1}$$

There exists a complex relationship between wave nonlinearity and directionality. Therefore, disparities arise when extending theories based on an assumption of unidirectionality to the nonlinear ocean enviroment. Herein, a brief non-exhaustive discussion is presented on the effect of directionality on ocean waves, from linear to second-order and beyond. This highlights the combined importance of directionality and nonlinearity in better understanding ocean processes and provides the motivations for this work.

1.1.1 Linear waves

At first order, the directionality of waves mainly affects their kinematics. When considering fixed and floating bodies in the oceans wave directionality has a significant effect on the forces that these bodies experience. Under unidirectional conditions ocean structures will experience maximum loads for a given wave height. Under directional conditions the maximum forces encountered at an equivalent wave height are reduced. However, considerable loading transverse to the mean directions of the waves is now experienced [Sharma and Dean, 1981]. These differing loading regimes have significant impact on aspects of structural design such as fatigue loading [Marshall, 1976].

A reduction in the maximum wave loading of ocean structures is a welcome result of directional spreading. Conversely, when considering the extraction of wave power from the oceans, this is an undesirable effect for certain wave power devices. Generally, the effects of directional spreading reduce the amount of power that can be extracted by wave devices with a directional bias. A global resource assessment by Gunn and Stock-Williams [2012] found that that failure to include directionality could lead to overestimation of extractable power by 15-20%. Folley and Whittaker [2009] discuss the extraction of wave power in the nearshore region; here the narrowing of the directional spectrum in this region is identified as an

advantage for power extraction. However, this is a largely under-appreciated effect with few authors directly addressing the topic.

1.1.2 Second-order waves

Beyond the spreading of energy in multiple directions experienced at first order, at second-order weak nonlinearity and directionality introduce a new range of issues for floating and fixed structures in the oceans. The most apparent of these, for structures in irregular weakly nonlinear, waves are wave drift, and springing. Wave drift occurs when low-frequency sub-harmonic second-order terms excite mainly horizontal motion of floating structures [Eatock Taylor and Kernot, 1999]. Wave drift can affect mooring loads for structures such as floating wind turbines [Lopez-Pavon et al., 2015] as well as semi-submersible drilling rigs and a floating production storage and offloading vessels [Fonseca et al., 2016]. Conversely, springing occurs for high-frequency super-harmonic terms where vertical motion is excited [Eatock Taylor and Kernot, 1999] in floating structures such as ships [Oberhagemann and El Moctar, 2011]. When modelling forces on piles, Sharma and Dean [1981] compare Stokes' second-order unidirectional theory to second-order calculations for irregular directional waves and find Stokes' theory significantly overestimates the resulting forces.

Second-order modification of linear waves produces waves with wider troughs and sharper peaks [Stokes, 1847]. This in turn affects crest height statistics. Forristall [2000] implements second-order theory to produce crest height distributions for two- and three-dimensional cases, finding good agreement with observations. A slight reduction of about 2% is noted for three-dimensional crest high predictions with directional spreading. The results presented by Forristall [2000] assume a fixed degree of directional spreading. Adcock and Draper [2015] address the effects of varying directional spreading on the second-order contribution to crest height

of focused wave groups, and find the second-order contribution to crest height to be independent of spreading for moderate degrees of spreading.

Where the degree of directional spreading is large or the crossing of wave groups occurs, second-order components vary more drastically from unidirectional conditions. Under unidirectional and narrow-banded directional spreading conditions second-order interactions cause a 'set-down' in the wave-average surface elevation under large waves or groups, as first discovered by Longuet-Higgins and Stewart [1962]. If the degree of spreading is increased beyond $30 - 40^0$, this set-down can change to form a 'set-up'. Such broad-banded directional conditions are unlikely [Forristall and Ewans, 1998] and hence a set-down is expected for the majority of conditions experienced in the oceans. However, for a number of *in situ* observations a set-up in wave-averaged surface elevation has been observed with measurements of large waves [Walker et al., 2004, Toffoli et al., 2007]. A prominent example is the 1995 New Year wave recorded at the Draupner platform in the North Sea, which displayed a set-up of approximate amplitude 0.4 m [Walker et al., 2004]. However, for the reported spreading conditions a set-down of the same magnitude would be expected [Adcock et al., 2011]. In this case, it is thought that the crossing of wave groups caused the anomalous set-up which had the effect of increasing the overall wave height by $O(1\text{ m})$. The set-up of the wave-averaged free surface in crossing seas is thus seen as an important potential contribution to the crest height of freak waves [Adcock et al., 2011, Adcock and Taylor, 2014, Fedele et al., 2016].

1.1.3 Higher-order waves

As the steepness of waves increases, higher-order nonlinear effects occur which too are affected by directionality. At second-order and beyond, ringing, and slamming may be observed. Ringing is the resonant excitation of stiff structures,

and slamming occurs when a structure is accelerated through the free surface [Eatock Taylor and Kernot, 1999].

For higher-order wave-wave interactions, an alternative explanation in the formation of freak waves to the constructive interference and weak nonlinearity of crossing waves, is modulational or Benjamin-Feir instability [Benjamin and Feir, 1967]. Benjamin-Feir instability is a nonlinear effect whereby side-bands draw energy from a dominant carrier wave resulting in the potential growth of a large steep wave. This instability has been shown to exist analytically in the form of 'breather' solutions to the Nonlinear Schrödinger equations [Ma, 1979], and in unidirectional wave flume experiments [Chabchoub et al., 2011, 2012a,b]. However, two independent experimental studies carried out by Onorato et al. [2009], have shown that directional spreading has the effect of 'quenching' modulational instability. This limits the applicability of this instability to sea conditions with very narrow degrees of directional spreading.

Wave breaking provides an upper limit to wave steepness and therefore height. Accordingly, breaking is a highly nonlinear wave phenomenon. Johannessen and Swan [2001] examine the relationship between directional spreading and wave breaking. These authors create moderately directionally spread wave groups in a wave tank, increasing the steepness of waves until breaking occurs. They show that the spreading of energy that results from directionality suppresses wave breaking, and steeper waves may exist for higher degrees of spreading. When considering crest height statistics for experimentally generated steep directionally spread irregular waves, Latheef et al. [2013] observed a strong dependence on directionality, where the competing phenomena of wave breaking and nonlinear amplification dictate the maximum crest height. Besides limiting height, wave breaking and hence directional spreading of steep waves also affects the spectral dissipation of energetic seas due to white-capping [Hasselmann, 1974, Cavaleri et al., 2007].

1.2 Aim and objectives

This thesis aims to examine the combined effect of leading-order nonlinearity and directional spreading, in laboratory and field measurements. This is achieved through the following objectives:

- To create a reliable and efficient numerical implementation for performing second-order wave calculations, based on Dalzell [1999] (Chapter 2),
- To validate experimentally the theory behind the set-up of highly directionally spread wave groups (Chapter 4),
- To demonstrate experimentally crossing of wave groups as a mechanism for the formation of a set-up (Chapter 5),
- To develop a tool for directional spreading estimation based on the second-order implementation (Chapter 7),
- To apply the spreading estimation tool to field measurements (North Alwyn dataset) and assess its effectiveness (Chapter 7).

1.3 Synopsis

This thesis comprises two parts, Part I (Chapters 3-5) concerns a detailed series of laboratory experiments which examine the relationship between directional spreading and the second-order nonlinearity of focused wave groups. Part II (Chapters 6,7) of this thesis applies a novel means of estimating directional spreading for individual Eulerian measurements, based on relationship between nonlinearity and directionality explored in Part I, to a large dataset. Below, the contribution made in the individual chapters is outlined.

Chapter 2: Second-Order wave model

Chapter 2 presents the fundamentals of linear wave theory and its extension to second-order, supplemented by a deterministic verification case. The chosen multicomponent method is also validated using real sea measurements and found to give similar results to other studies. A numerical implementation of second-order wave model used herein is outlined. The implementation significantly reduced the computational time required to perform second-order calculations, making possible the work carried out in subsequent chapters.

Part I: The set-up/down of directionally spread focused waves groups

Chapter 3: Introduction and experimental method

Chapter 3 outlines the detailed experimental test series conducted in Part I. These tests were carried out at the FloWave Ocean Research Facility, a state of the

art circular wave tank that allows for the creation of waves that travel in all directions. An in-depth discussion is given of the underlying physics behind the set-up and down of the wave-averaged free surface. Then, details are presented of the experimental test campaign, and the methodology of the experimental procedure used in Chapters 4 and 5.

Chapter 4: Directionally spread focused wave groups

Results from the first set of experimental tests are presented in Chapter 4. Here, single focused wave groups are created with spreading ranging from unidirectional to axisymmetric. In doing so, the formation of a set-up in wave-averaged surface elevation under a focused wave group is confirmed experimentally for the first time, for degrees of directional spreading greater than $30 - 40°$. Tests are also presented where the spatial structure of the wave-averaged surface elevation is captured. These tests give new insight into the physics behind the formation of a set-up, which behaves like a partial standing wave unlike the set-down which travels with the wave group.

Chapter 5: Crossing wave groups

Chapter 5 presents results from the second set of experimental examining the wave-averaged surface elevation of crossing wave groups. A set-up under two crossing wave groups forms when the groups are separated by an angle of 50-70° and above. The phenomenon of two crossing wave groups at large angles of separation presents an explanation for the formation of a set-up under large waves that is realisable in extra-tropical storms, in contrast to highly spread individual wave groups, which are unlikely to occur in reality. The spatial structure of the

wave-averaged surface elevation for crossing wave groups is also shown to differ significantly from that created by a single group.

Part I is based upon a paper entitled "The set-down and set-up of directionally spread and crossing surface gravity wave groups" co-authored with T.A.A. Adcock and P.H. Taylor and T.S. van den Bremer submitted to the Journal of Fluid Mechanics

Part II: Directional estimation of ocean measurements

Chapter 6: Field data and quality control

Chapter 6 details the acquisition and quality control of the field measurements used in Chapter 7. A brief description is given of the North Alwyn platform, and the instrumentation installed on the platform. Quality control procedures used in the processing of free surface elevation measurement are reviewed, and the analysis procedure for the North Alwyn dataset is outlined. The results of the quality control process are then summarised.

Chapter 7: Estimation of directional spreading from point measurements

In Chapter 7 the second-order wave model implemented in Chapter 2, and extensively validated in Chapters 2 to 5, is applied to *in situ* free surface elevation measurements. Here, the model is used as a tool to estimate the degree of directional spreading of the measurements, named the 'Long-Wave Method'. This method allows the estimation of the degree of directional spreading using only a single Eulerian measurement. This method is applied to the North Alwyn

dataset presented in Chapter 6. The accuracy of the method is assessed through comparison against conventional spreading estimation techniques and hindcast data. It is found that the method is capable of accurately estimating spreading from noisy, chaotic real sea data, proving the method to be a useful tool for recovering information of wave spreading from single point measurements.

Part II is based upon a paper entitled "Wave Directional Spreading From Point Field Measurements" co-authored with V. Venugopal and A.G.L Borthwick and published in Proceedings of the Royal Society A (2017, Volume 473, 20160781)

Chapter 8: Conclusions

Finally, Chapter 8 summarises the results and lists the conclusions of the previous chapters. Plans and recommendations for further development of the work presented herein are also discussed.

Chapter 2

Second-order wave model

Linear wave theory is often used to model waves in the ocean, as it provides a good first approximation to most aspects of wave motion. However, as the steepness of waves increases or water depth decreases, higher order nonlinear effects become more prevalent. Herein, attention is focused on waves in deep water. Therefore, having first introduced linear wave theory, second-order theory based on Stokes-type perturbation expansions is discussed. Comparison is then drawn between separation-of-scales and multi-component interaction kernel-based approaches of modelling second-order wave-wave interactions. The latter approach is computationally costly. However, it offers the ability to model a more broadbanded and directionally spread spectrum. A numeral implementation that reduces this cost significantly is outlined, and the results validated using a series of examples.

2.1 Introduction

Surface gravity waves are governed by the Laplace equation to which the application of appropriate boundary conditions and approximations gives rise to a number of solutions or wave theories. The different regimes under which these theories are valid is shown in Figure 2.1, for non-dimensional wave height H/gT^2 (proportional to steepness α), as a function of non-dimensional water depth h/gT^2. Here, H is wave height, T is wave period, h is water depth, and g is gravity. In deep water, a Stokes-type perturbation approach of increasing orders of steepness is valid (Figure 2.1). Whereas in shallow water canonical and stream function theories are applicable. Small waves of low steepness may be modelled to a reasonable degree of accuracy using linear wave theory, as higher-order effects are small in comparison. However, to capture fully the dynamics of ocean waves, it is necessary to implement higher-order models. As a first approximation, second-order theory can account for the majority of nonlinear dynamics associated with surface gravity waves observed in the ocean.

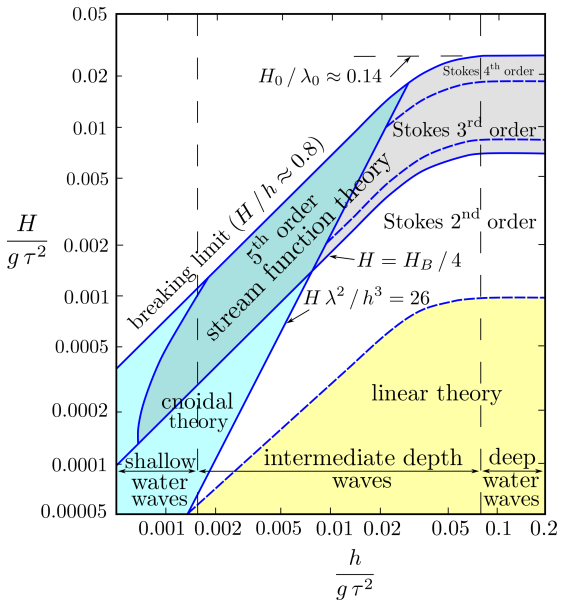

Figure 2.1. Validity of water wave theories (reproduced from Le Méhauté [1976]). showing non dimensional wave heigh as a function of non-dimensional water depth

In this chapter, the principles that underpin second-order theory and the wave models used herein are introduced. A brief discussion on the numerical implementation of the model is presented, alongside validation cases.

2.2 Theory

Laplace equation

When modelling surface gravity waves, it is assumed that the fluid motion is irrotational, and incompressible. Hence, the motion can be described by a velocity potential $\boldsymbol{u} = \nabla\boldsymbol{\phi}$, which must satisfy continuity $\nabla\cdot\boldsymbol{u} = 0$. Therefore, $\nabla\cdot\nabla\boldsymbol{\phi} = 0$ and the fluid also satisfies the Laplace equation

$$\nabla^2\boldsymbol{\phi} = \frac{\partial\boldsymbol{\phi}^2}{\partial x^2} + \frac{\partial\boldsymbol{\phi}^2}{\partial y^2} + \frac{\partial\boldsymbol{\phi}^2}{\partial z^2} = 0. \tag{2.1}$$

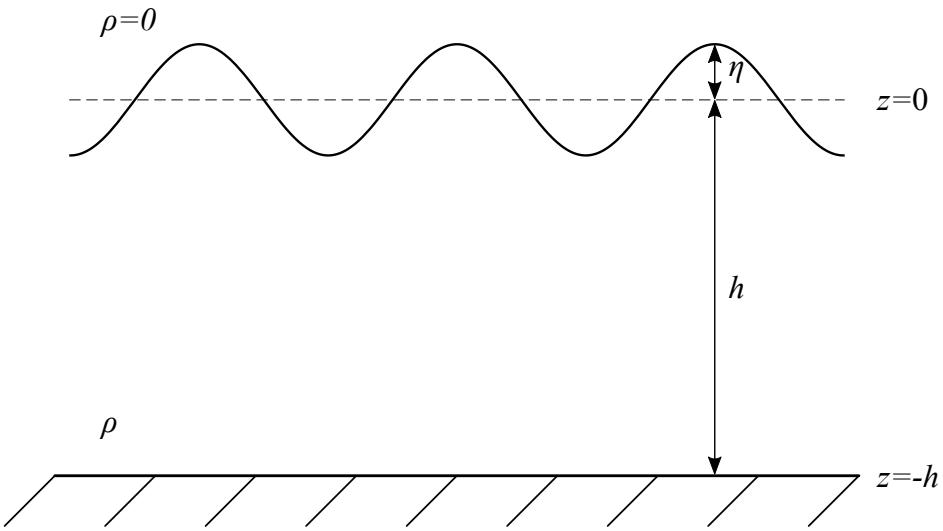

Figure 2.2 Wave definition schematic

Solutions to this governing equation, may be sought by the application of appropriate boundary conditions. Here, x, y, and z are standard Cartesian coordinates, with z defined positively upwards from the mean water level, and t is time.

Kinematic Free Surface Boundary Condition (KFSBC)

For fluid interfaces to exist, there must be zero flow across them. Hence at the free surface boundary a kinematic free surface boundary condition must be satisfied, which states that a particle on the free surface η must remain so.

$$\frac{\partial \eta}{\partial t} + \frac{\partial \boldsymbol{\phi}}{\partial x}\frac{\partial \eta}{\partial x} + \frac{\partial \boldsymbol{\phi}}{\partial y}\frac{\partial \eta}{\partial y} - \frac{\partial \boldsymbol{\phi}}{\partial z} = 0 \qquad \text{on} \qquad z = \eta(x, y, t). \tag{2.2}$$

Bottom Boundary Condition (BBC)

Similarly, at the bottom boundary, for water depth h, there can be no flow orthogonal to the boundary giving the bottom boundary condition

$$\frac{\partial \boldsymbol{\phi}}{\partial z} = 0 \qquad \text{on} \qquad z = -h, \tag{2.3}$$

given that for constant depth $h \neq h(x, y, t)$.

Dynamic Free Surface Boundary Condition (DFSBC)

Unlike a fixed interface, the free surface is able to deform and thus cannot support variations in pressure. Therefore, the dynamic free surface boundary condition states that there is zero pressure on the free surface:

$$2g\eta + \frac{2\partial \boldsymbol{\phi}}{\partial t} + (\nabla \boldsymbol{\phi})^2 = 0 \qquad \text{on} \qquad z = \eta. \tag{2.4}$$

Both (2.2) and (2.4) are evaluated at η, which is often unknown. Therefore the boundary conditions are expressed as a Taylor series about $z = 0$. Taking terms to second order gives:

$$\frac{\partial \eta}{\partial t} + \frac{\partial \boldsymbol{\phi}}{\partial x}\frac{\partial \eta}{\partial x} + \frac{\partial \boldsymbol{\phi}}{\partial y}\frac{\partial \eta}{\partial y} - \frac{\partial \boldsymbol{\phi}}{\partial z} - \eta\frac{\partial^2 \boldsymbol{\phi}}{\partial z^2} = 0 \qquad \text{on} \qquad z = 0, \tag{2.5}$$

and

$$2g\eta + \frac{2\partial \boldsymbol{\phi}}{\partial t} + 2\eta\frac{\partial^2 \boldsymbol{\phi}}{\partial z t} + \nabla^2 \boldsymbol{\phi} = 0 \qquad \text{on} \qquad z = 0. \tag{2.6}$$

2.2.1 Linear waves

Considering only the linear terms of equations (2.5) and (2.6), gives:

$$\frac{\partial \eta}{\partial t} - \frac{\partial \boldsymbol{\phi}}{\partial z} = 0 \qquad \text{on} \qquad z = 0, \tag{2.7}$$

and

$$\frac{\partial \boldsymbol{\phi}}{\partial t} + g\eta = 0 \qquad \text{on} \qquad z = 0. \tag{2.8}$$

The linear solution for a freely propagating monochromatic wave of amplitude a is

$$\eta = a\cos(\varphi), \qquad \text{where} \qquad \varphi = \mathbf{k}\cdot\mathbf{x} - \omega t \tag{2.9}$$

the phase of the wave is φ, $\mathbf{k}$ is the wavenumber vector, and $\mathbf{x}$ is the Cartesian position vector. The magnitude of the wavenumber vector $|\mathbf{k}|$ is related to natural frequency ω by the linear dispersion relation,

$$\omega^2 = |\mathbf{k}| g \tanh(|\mathbf{k}|h). \tag{2.10}$$

Using this linear solution, multi-directional multi-chromatic waves can be modelled using a linear summation of N individual monochromatic plane waves as follows:

$$\eta(x, y, t) = \sum_{n=1}^{N} a_n \cos(\mathbf{k}_n \cdot \mathbf{x}_n - \omega_n t). \tag{2.11}$$

2.2.2 Nonlinear waves

At higher orders, a simple Fourier-based summation is not possible. A perturbation expansion in steepness $\alpha = a|\mathbf{k}|$ can be used to decompose the free surface

into a series of terms of increasing order [Stokes, 1847]:

$$\eta = \eta^{(1)} + \alpha\eta^{(2)} + \alpha^2\eta^{(3)} + \cdots + \alpha^{j-1}\eta^{(j)}. \tag{2.12}$$

A truncated version of this perturbation series may be used to create a linear second-order PDE with a nonlinear inhomogeneous part based on the first-order solution. In addition to the self-interaction terms of a monochromatic wave (2.12), waves of different frequencies will interact resulting in bound harmonics. Up to second-order these occur at the sum frequencies

$$\eta_+^{(2)} = a_1 a_2 B^+ \cos(\varphi_1 + \varphi_2), \tag{2.13}$$

and the difference frequencies

$$\eta_-^{(2)} = a_1 a_2 B^- cos(\varphi_1 - \varphi_2), \tag{2.14}$$

of the two interacting parent waves, also often referred to as sub- and super-harmonic terms. The interaction of free waves to produce bound harmonics was first derived by Longuet-Higgins and Stewart [1962] for deep water. This theory was first extended to finite depth by Hasselmann [1962] and later more explicitly by Sharma and Dean [1981]. Corrections were then made by Dalzell [1999] and Forristall [2000]. Using these solutions, multi-directional multi-chromatic non-linear free surface waves can be expressed to second-order as a summation of uni-directional linear waves and their bound interactions:

$$\eta = \underbrace{\sum_{n=1}^{2} a_n \cos\varphi_n}_{O(\alpha)} + \underbrace{\sum_{n=1}^{2} a_n^2 B \cos(2\varphi_n)}_{O(\alpha^2)\text{ self interaction}} + \underbrace{a_1 a_2 B^+ \cos(\varphi_1+\varphi_2) + a_1 a_2 B^- \cos(\varphi_1-\varphi_2)}_{O(\alpha^2)}, \quad (2.15)$$

where B, B^-, and B^+ used herein are the self, sum, and difference interaction kernels derived by Dalzell [1999] for finite depth.

2.2.3 Second-order interaction kernels

Here, we discuss the calculation of second-order difference waves, as they are of primary interest in the following chapters. However, second-order sum waves may be calculated in the same manner. Starting with the linear spectrum expressed as a complex Fourier series:

$$\eta^{(1)} = \sum_{n=1}^{n=N} \hat{\eta}_n \exp\left(\imath\omega_n t\right), \quad (2.16)$$

in which $\hat{\eta}_n$ is the n-th constituent of the complex vector $\hat{\eta}$ generated by performing a Fast Fourier Transform (FFT) on the free surface elevation time series, and ω_n is the angular frequency of the n-th constituent. Calculating the interaction of each wave pair gives the second-order difference waves

$$\eta_-^{(2)} = \sum_{i=1}^{N_\theta}\sum_{j=1}^{N_\theta}\sum_{n=1}^{N_\omega}\sum_{m=1}^{N_\omega} D(\theta_i)D(\theta_j)\hat{\eta}_n\hat{\eta}_m B^-\left(\mathbf{k}_{n,i}, \mathbf{k}_{m,j}, \omega_n, \omega_m, h\right)\exp\left(\imath\left(\omega_n-\omega_m\right)t\right), \quad (2.17)$$

where D is the assumed spreading function, dependent on wave incidence angle θ, and B^- is the interaction kernel for difference terms. B^- is a function of ω, θ, h, and $\mathbf{k}$, and is defined as [Dalzell, 1999]:

$$
\begin{aligned}
B^{-} = & \frac{\omega_n^2 + \omega_m^2}{2g} + \frac{\omega_n \omega_m}{2g}\left(1 + \frac{\cos(\theta_i - \theta_j)}{\tanh(|\mathbf{k}_{n,i}|h)\tanh(|\mathbf{k}_{m,j}|h)}\right) \\
& \times \left(\frac{(\omega_n - \omega_m)^2 + g|\mathbf{k}_{n,i} - \mathbf{k}_{m,j}|\tanh\left(|\mathbf{k}_{n,i} - \mathbf{k}_{m,j}|h\right)}{C^{-}\left(\mathbf{k}_{n,i}, \mathbf{k}_{m,j}, \omega_n, \omega_m, h\right)}\right) \\
& + \frac{(\omega_n - \omega_m)}{2gC^{-}\left(\mathbf{k}_{n,i}, \mathbf{k}_{m,j}, \omega_n, \omega_m, h\right)}\left[\frac{\omega_n^3}{\sinh^2(|\mathbf{k}_{n,i}|h)} - \frac{\omega_m^3}{\sinh^2(|\mathbf{k}_m|h)}\right],
\end{aligned}
\tag{2.18}
$$

where

$$
C^{-} = (\omega_n - \omega_m)^2 - g|\mathbf{k}_{n,i} - \mathbf{k}_{m,j}|\tanh\left(|\mathbf{k}_{n,i} - \mathbf{k}_{m,j}|h\right). \tag{2.19}
$$

2.2.4 Separation-of-scales

Calculating the interaction of individual waves is a computationally intensive process. When sufficiently narrow-banded in frequency and direction ($\epsilon \to 0$, $\sigma_\theta \to 0$), a separation-of-scales approach may be used, where waves are modelled as a 'fast' carrier wave of frequency ω_0 and wavenumber k_0 which is modulated by 'slow' wave envelope A.

$$
\eta^{(1)} = A(X, Y)\exp(\imath(k_0 x - \omega_0 t)) \tag{2.20}
$$

The slow scales of the wave envelope are related to fast scales x, and t by

$$
X = \epsilon_x(x - c_{g,0}t), \qquad Y = \epsilon_y y, \tag{2.21}
$$

where ϵ is a small parameter that relates the length scales of the fast carrier wave and the slow modulation of the group. In a similar manner to the approach above, this linear solution may be used as a forcing to produce a second-order response

(in α):

$$\eta_{-}^{(2)} = \frac{-|a_0|^2\sigma_x\sigma_y}{16\pi}\int_{-\infty}^{\infty}\int_{-\infty}^{\infty}\frac{\kappa^2}{\sqrt{\kappa^2+\lambda^2}\tanh\left(\sqrt{\kappa^2+\lambda^2}h\right)}e^{-(\kappa\sigma_x)^2/4-(\lambda\sigma_y)^2/4}e^{\imath(\kappa\tilde{x}+\lambda\tilde{y})}d\kappa d\lambda. \tag{2.22}$$

where the wavenumber is normalised by $\hat{\kappa} = k\sigma_x$ and $\hat{\lambda} = \lambda\sigma_y$. This solution has been derived[1] for the difference waves or wave-averaged surface elevation of a Gaussian wave envelope

$$A = a_0^2\exp(-\frac{x^2}{2\sigma_x^2} - \frac{y^2}{2\sigma_y^2}) \tag{2.23}$$

where the Gaussian half-width is defined by $\sigma_x = 1/k_0\epsilon_x$, the amplitude at focus by a_0, and group velocity by $c_{g,0}$. Here, directional spreading is captured by the slow variation of the envelope in the spanwise direction. Where $R = \sigma_x/\sigma_y$ is the aspect ratio of the group. A Gaussian wave envelope is used here as this pertains to the validation case below and experiments carried out in Chapter 3. However, this approach is not limited to such a form.

2.3 Numerical implementation

While (2.22) can be implemented using 2D numerical integration which takes a few seconds on a desktop PC (16 GB RAM, 3.4 GHz), (2.17) involves a quadruple summation over both frequency and direction. This incurs large computational cost, which was reduced through the creation of a number of simplifications implemented in the following procedure. Dropping the exponential term in (2.17),

[1]The author is grateful to van den Bremer (personal communication) for the derivation of the results, which is based on an extension of van den Bremer and Taylor [2015]. The derivation is reproduced in Appendix A

the complex vector that represents the difference waves may be expressed as

$$\hat{\eta}_{-}^{(2)} = \sum_{i=1}^{N_\theta}\sum_{j=1}^{N_\theta}\sum_{n=1}^{N_\omega}\sum_{m=1}^{N_\omega} D(\theta_i)D(\theta_j)\hat{\eta}_n\hat{\eta}_m B^{-}. \tag{2.24}$$

For a given time series $D(\theta)$ is the only independent variable, therefore B^{-} can be expressed as an element of the $N_\omega \times N_\omega$ matrix $\mathbf{B^{-}}(\theta_\delta)$, where θ_δ is the angle between interacting wave pairs. Hence, for frequency independent cases $\eta_n\eta_m$ the interaction of all frequencies can be expressed in matrix form as

$$\mathbf{H}(n,m) = \hat{\eta}^T\hat{\eta}, \tag{2.25}$$

$$\mathbf{H}(n,m) = \begin{bmatrix} \hat{\eta}_1\hat{\eta}_1 & \hat{\eta}_1\hat{\eta}_2 & \hat{\eta}_1\hat{\eta}_3 & \cdots & & \\ \hat{\eta}_2\hat{\eta}_1 & \hat{\eta}_2\hat{\eta}_2 & & & & \\ \hat{\eta}_3\hat{\eta}_1 & & \ddots & & & \vdots \\ \vdots & & & \ddots & & \hat{\eta}_{N-2}\hat{\eta}_N \\ & & & & \hat{\eta}_N\hat{\eta}_N & \hat{\eta}_{N-1}\hat{\eta}_N \\ & & \cdots & \hat{\eta}_N\hat{\eta}_{N-2} & \hat{\eta}_N\hat{\eta}_{N-1} & \hat{\eta}_N\hat{\eta}_N \end{bmatrix} \tag{2.26}$$

and similarly the interaction of all directional pairs $D(\theta_i)D(\theta_j)$

$$\mathbf{D^{\star}}(i,j) = \mathbf{D}^T\mathbf{D}. \tag{2.27}$$

The diagonal elements of $\mathbf{D^{\star}}$ correspond to components of equal separation $\theta_i - \theta_j$. Therefore $\mathbf{D^{\star}}$ can be transformed to a function of $\theta_\delta = \theta_i - \theta_j$, by summation over its diagonals

$$\mathbf{D}^{\star}(\theta_\delta) = \sum_{i-j=0}^{i-j=N_\theta} D_{ij}^{\star}. \tag{2.28}$$

As $\mathbf{D}^{\star}(\theta_\delta)$ and $\mathbf{B^{-}}(\theta_\delta)$ can be expressed as functions of θ_δ, the interaction of all frequency pairs over all directional pairs may now be reduced to summation over

equal angles of separation θ_δ

$$\mathbf{H}_{-}^{(2)}(n,m) = \sum_{\delta=0}^{N_\theta} \mathbf{D}^{\star}(\theta_\delta)\mathbf{HB}^{-}(\theta_\delta). \tag{2.29}$$

Diagonal elements of this matrix represent values of equal resultant frequency $\omega_{2-} = \omega_n - \omega_m$ therefore summation over diagonals provides the complex vector $\hat{\eta}_{-}^{(2)}$ from

$$\hat{\eta}_{-}^{(2)} = \sum_{n-m=0}^{n-m=N_\omega} H_{-nm}^{(2)}, \tag{2.30}$$

Finally performing the inverse FFT on $\hat{\eta}_{-}^{(2)}$, gives the second-order difference waves as:

$$\eta_{-}^{(2)} = \sum_{n=1}^{N_\omega} \hat{\eta}_{-n}^{(2)} \exp(\imath\omega_{2-_n} t), \tag{2.31}$$

in which $\omega_{2-,n}$ is the n-th difference frequency.

2.4 Validation

The above method was tested against fully nonlinear potential flow simulations of focused NewWave groups on water of infinite depth carried out by Gibbs and Taylor [2005], using a numerical solver developed by Bateman et al. [2001]. In addition to this, a narrow-banded separation-of-scales approximation (2.22) is used to here predict $\eta_{T-}^{(2)}(\epsilon \to 0)$. Figure 2.3 shows the linear free surface for unidirectional and $\sigma_\theta = 15^\circ$ spread simulations (panels a and b), where σ_θ is the degree of directional spreading for a Gaussian distribution. The corresponding bound difference waves obtained using the multi-component interaction kernel method, and the narrow-banded approximation based are compared to the results of Gibbs and Taylor [2005]. For the unidirectional case (panels a and c) excellent agreement is shown between all three methods, with the separation-of-scales

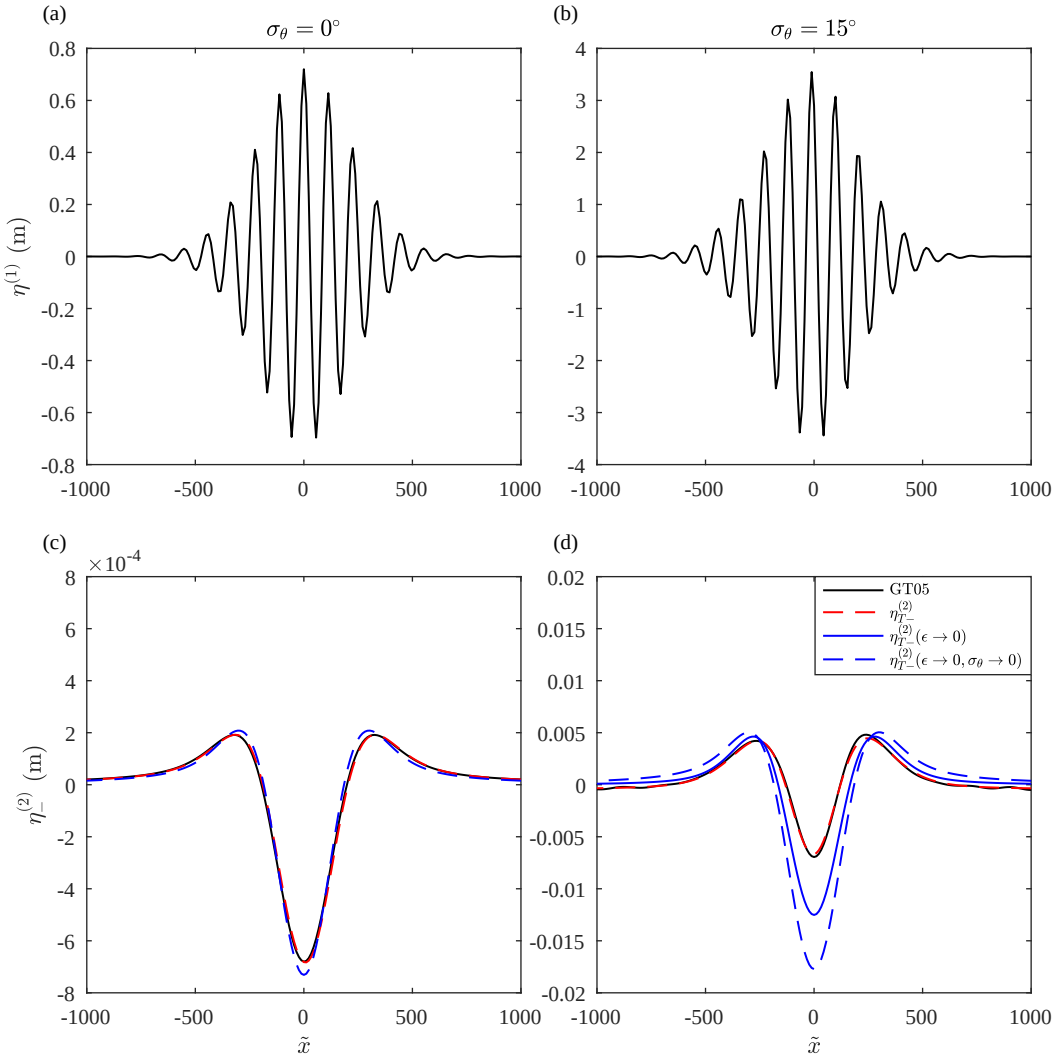

Figure 2.3. Focused NewWave group; linear free surface elevation $\eta^{(1)}$ at $x = 0$, panel a unidirectional, and panel b σ_θ=15°. Corresponding second-order difference waves (panels d and c); fully nonlinear potential flow (solid black line) from (GT05), interaction kernels (dashed red line), and separation-of-scales approximation (blue lines).

slightly over predicting the amplitude of the set-down. As spreading is increased (panels b and d) the narrow-banded separation-of-scales approximation begins to diverge from the potential flow and interaction kernel results, which again show excellent agreement. This is an expected result of the broadening of the directional spectrum, and the limitations of the narrow-banded assumption. These effects

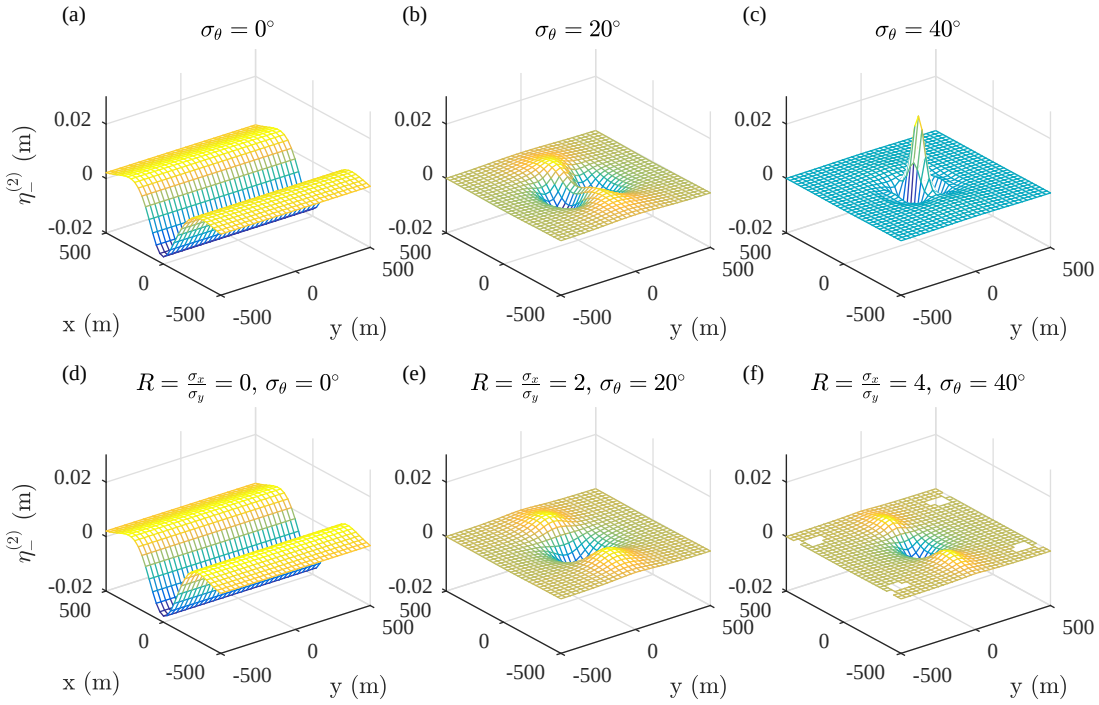

Figure 2.4. Separation-of-scales comparison, mesh plots show 2D surface of calculated second-order difference waves $\eta_{T-}^{(2)}$; produced using interaction kernels (panels a to c), and separation-of-scales method (panels d to f). The panels correspond to increasing degree of directional spreading, with σ_θ =0-360°.

are illustrated in figure 2.4, $\eta_{T-}^{(2)}(x, y)$ is calculated for the wave group shown in figure 2.3b with increasing degrees of directional spreading. Panels a to c show the difference waves calculated using interaction kernels. Initially a large set-down is predicted; as the degree of spreading increases, 'crossing' waves interacting at large angles of incidence begin to form a set-up. This is clearly shown in panel b near $x = 0$ $y = 0$ the set-up starts to reduce the magnitude of the set-down. Finally, as the degree of spreading is increased further, the set-down at $x = 0$ $y = 0$ no longer exist and the set-up caused by crossing wave components dominates. The separation-of-scales calculations initially predict a set-down too. However, as the degree of spreading is increased the amplitude of the set-down decreases but it is clear that the effects of the set-up are not observed. This is owing to the means by which spreading is implemented in the separation-of-scales

method. Here, the wave propagates in the x direction, and spreading is modelled by varying the orthogonal group shape R. This means that despite the linear wave group possessing the correct envelope structure, the crossing of waves is not modelled. Therefore, when spreading is increased the total amplitude of the set-down decreases as energy is spread out directionally, however, the coupled effect of the set-up is not modelled.

Both approaches of calculating $\eta^{(2)}_{T-}$ have been shown to agree well under narrow-banded conditions in both frequency and direction. Similarly both approaches have their own merits. However, herein experiments and *in situ* measurements are analysed, where narrow-banded conditions are no longer experienced. Thus the interaction kernels method is used to calculate $\eta^{(2)}_{T-}$. The separation-of-scales approach is revisited for crossing wave groups in Chapter 3.

Figure 2.5 panel a shows the Draupner time series containing the measurement of the seminal freak wave observed on the 1st of January 1995. The theoretically predicted difference waves $\eta^{(2)}_{T-}$ for an assumed spreading of 20° are presented in panel b. The Draupner time series was linearised using the method presented by Walker et al. [2004], before calculating $\eta^{(2)}_{T-}$ (see Chapter 7). These results are consistent with the results of Adcock and Taylor [2009], and Adcock et al. [2011], where the predicted difference waves excluding those around the freak wave itself match the observed waves very well. These results provide validation that the present implementation can be used to predict accurately and recreate observed difference waves $\eta^{(2)}_{M-}$. This finding is rigorously tested experimentally in a physical laboratory environment in Part I, and utilised as a means of spreading estimation of field measurements in Chapter 7.

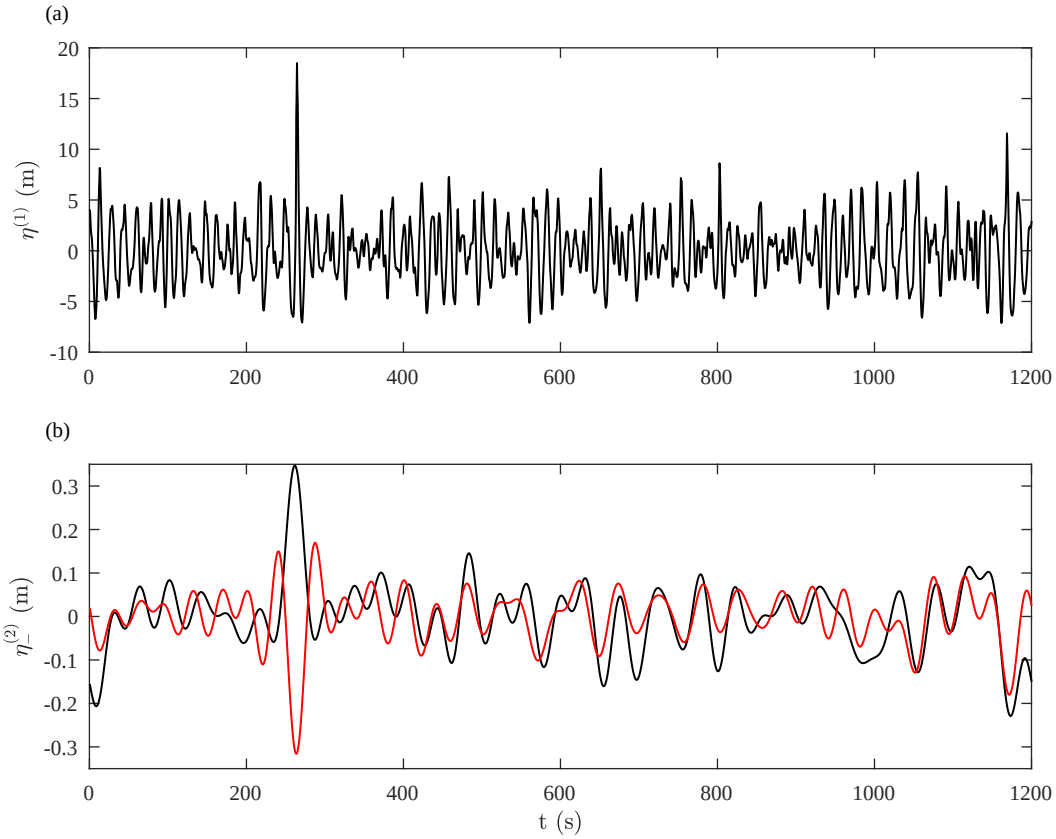

Figure 2.5. Draupner time series recorded on at 15:20 in the 1st of January 1995, panel a shows the measured free surface elevation, and panel b shows the corresponding observed second-order difference waves $\eta^{(2)}_{M-}$ (black line), and the theoretically predicted $\eta^{(2)}_{T-}$ difference waves for an assumed spreading of 20° (red line).

2.5 Discussion

Using the numerical implementation developed above, a theoretical model capable of calculating the second-order bound harmonics for a given linear time series was implemented. The model compares well to a series of validation cases and other second-order models. The implementation described above also allows for a significant reduction in the associated computational cost. The data analysed in Chapter 7 consists of over 20,000, 1,200 s duration time series sampled at 6,000 discrete points. Calculating the second-order difference waves $\eta^{(2)}_{T}-$ using

the quadruple sum shown in (2.17) takes approximately half an hour, on a standard desktop computer (16 GB RAM, 3.4 GHz). However, using the improved numerical implementation the same calculations take less than a second. The importance of this reduction is twofold. Firstly, it makes the analysis of such a large data set possible, reducing the total computational time to a few hours. Secondly, these savings mean that the long-wave spreading method presented in Chapter 7 can be carried out on a time scale comparable to that of other spreading estimation methods.

2.6 Conclusions

A brief overview of the wave models used herein is presented. Significant savings in computation were achieved using the above numerical scheme. Savings made in computational time made possible the analysis of the North Alwyn Dataset presented in Chapter 7, which otherwise would have been prohibitively time consuming. The validation of the numerical scheme shows excellent agreement with potential flow calculations. The accuracy of the model is further illustrated in Part I where comparison is made with physical tests.

Part I

The set-up/down of directionally spread focused wave groups

Chapter 3

Introduction and experimental method

For sufficiently directionally spread surface gravity wave groups, the set-down of the wave-averaged free surface, first described by Longuet-Higgins and Stewart [1962], can turn into a set-up. The structure and magnitude of this wave-averaged set-up is examined, which behaves as a partial standing wave: in space, it consists of a rapidly varying standing-wave pattern slowly modulated by the product of the envelopes of the two groups; in time, it grows and decays on the slow time scale associated with the translation of the groups. Whether this 'set-up' actually enhances the surface elevation at the point of focus depends crucially on the phases of the linear wave groups, unlike the set-down, which is always negative and inherits the spatial structure of the underlying group(s). Detailed laboratory measurements of the wave-averaged free surface are presented, examining both single wave groups, varying the degree of spreading from small to very large, and the interaction between two wave groups, varying both the degree of spreading and the crossing angle between the groups.

3.1 Introduction

In order to satisfy the non-linear kinematic and dynamic free surface boundary conditions, linear freely propagating surface gravity waves are accompanied by non-linear bound waves. For periodic waves, a so-called Stokes expansion in the amplitude of the waves reveals that any periodic wave is accompanied by a series of harmonic components with integer multiples of the frequency of the linear parent wave and their magnitude proportional to increasing integer powers of the steepness [Stokes, 1847]. For multi-chromatic parent waves representing waves groups, the harmonic components interact to give both 'frequency-sum' and 'frequency-difference' terms, as first described by Longuet-Higgins and Stewart [1962] for unidirectional waves and including terms up to second-order in steepness. Although expressions for the 'frequency-difference' terms in a multi-directional sea can be distilled from Hasselmann [1962] (cf. Okihiro et al. [1992]), Sharma and Dean [1981], Dalzell [1999] and Forristall [2000] are commonly credited for extending the work of Longuet-Higgins and Stewart [1962] to directional seas, allowing for interactions between parent wave components of different frequencies and travelling in different directions. In the limit of a quasi-monochromatic group with a single carrier wave travelling in one direction, differential equations describing these second-order bound interactions can also be calculated using a multiple-scales approach. In the seminal papers by Dysthe [1979] (infinite water depth) and Davey and Stewartson [1974] (finite water depth), the non-linear evolution equations for the wave group are accompanied by a second set of differential equations describing the mean flow and the wave-averaged free surface.

Physically, in the unidirectional case the bound frequency-difference terms cause a depression in the wave-averaged surface elevation on the scale of the wave group, often referred to as a set-down [Longuet-Higgins and Stewart, 1962]. It can be

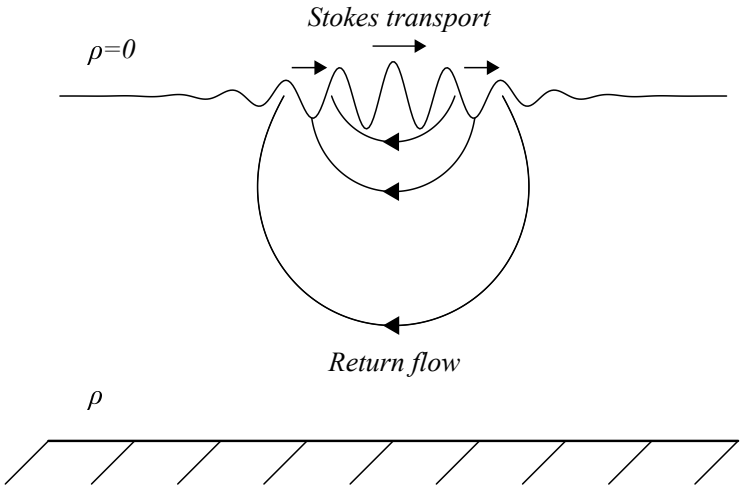

Figure 3.1. Illustration of Stokes transport and resulting return flow under a wave group (adapted from van den Bremer [2014]).

thought of as the free surface manifestation of the return flow underneath the group that forms to balance the Stokes transport, which is divergent on the scale of the group and acts to 'pump' fluid from its trailing edge to its leading edge as illustrated in figure 3.1 [McIntyre, 1981, van den Bremer and Taylor, 2015, 2016]. The set-down is simply largest at the centre of the group, where the (negative) return flow is also largest in magnitude. In the limit of a unidirectional deep-water parent wave and a group that is long relative to the water depth h, the set-down becomes: [Longuet-Higgins and Stewart, 1964]:

$$\eta_{-}^{(2)} = -\frac{|A(\tilde{x})|^2}{4h}, \tag{3.1}$$

where A denotes the amplitude envelope of the group, and $\tilde{x} = x - c_{g,0}t$ is the horizontal coordinate in the group reference frame.

When examining the very large freak wave that occurred at the Draupner platform

in the North Sea on the 1st of January 1995, Walker et al. [2004] observed a large set-up in the wave-averaged surface elevation. Subsequent analysis of the Draupner wave by Adcock and Taylor [2009] and Adcock et al. [2011], identified crossing waves as the probable cause of the set-up associated with the Draupner wave. This finding is supported by a high resolution hindcast model of the Draupner storm performed by Cavaleri et al. [2016], which highlighted the presence of two large crossing wave systems. Adcock and Draper [2015] show for waves of random phase a set-up may also occur under normal spreading conditions, however, for large waves this is less likely owing to phase coherence associated with wave group structure. In addition to the Draupner wave, Fedele et al. [2016] examine set-up in the wave-averaged surface elevation of two other very large waves concluding that crossing directional spectra was the likely cause. In a broader sense both Fedele et al. [2016], Adcock et al. [2011] conclude that crossing of waves and resulting set-up may provide a contribution to the formation of Freak waves (see Kharif and Pelinovsky [2003], Dysthe and Müller [2008], Adcock and Taylor [2014], and Onorato et al. [2013] for reviews of the mechanisms behind freak waves).

It is necessary to make a functional distinction between waves with a large degree of spreading and crossing waves. In both scenarios a set-up forms under the same mechanism, the interaction of waves at large angles. However, to have two well separated crossing wave groups is a significantly more likely eventuality than a highly directionally spread group in extra-tropical storms.

A set-up was also observed by Toffoli et al. [2007] for smaller waves measured on Lake George, Australia. Toffoli et al. [2007] showed this effect to be consistent with second-order theory, and found that crossing waves of similar frequency result in positive interaction by numerically computing the frequency-difference interaction kernel of Sharma and Dean [1981]. These effects were also observed in time-domain simulations performed by Toffoli et al. [2006]. A similar observation

was made by [Okihiro et al., 1992] based on the (equivalent) frequency-difference interaction kernel reconstructed from Hasselmann [1962], noting that this kernel reduces with increasing angle and changes sign for two wave components at an angle of 30° in deep water ($k_0 d \gg 1$). Indeed, the energy spectrum associated with second-order bound waves reduces considerably with increasing directional spreading [Herbers et al., 1994].

Experimentally, Johannessen and Swan [2001] examined the evolution and focusing of moderately directionally-spread focused wave groups and found that the directionality of the wave groups serves to reduce the overall nonlinearity of the waves, affecting the onset of breaking and nonlinear modification of the free waves. Onorato et al. [2009] and Toffoli et al. [2010] performed experiments and numerical analysis of irregular crossing waves, observing a direct relationship between crossing angle and kurtosis, an indicator of the probability of freak wave occurrence. All reported experimental studies, have been limited to small degrees of directional spreading and have not observed the formation of a set-up, with the exception Toffoli et al. [2011], who conducted experiments with crossing wave systems at crossing angles up to 40°, but did not specifically examine the occurrence of a set-up.

Herein, the structure and magnitude of the wave-averaged free surface for directionally spread and crossing surface gravity waves groups is examined. When and how a set-down can turn into a set-up is investigated. Experiments are conducted in the circular wave tank at the FloWave Ocean Energy Research Facility, which has 168 individually controlled paddles enabling the generation of wave groups with any desired directional distribution. Three categories of experiments are carried out: tests in which the degree of directional spreading for an individual wave group is varied (category A), tests in which the three-dimensional surface associated with the set-down/set-up of such a group is

measured (category B), and tests in which two waves group cross each other at different angles (category C).

Figure 3.2 illustrates the linear surface profile at the time of linear focus for the groups examined experimentally in categories A and B for three individual groups with increasing degrees of directional spreading. Figure 3.3 shows the linear surface profile for two groups with narrow degrees of directional spreading crossing at an angle, as examined in category C. Looking ahead, panels g-i show how the set-down associated with the individual groups before g and after crossing i can turn into a set-up h at the point of crossing. Although the set-down takes the form of a 'hole' on the scale of the envelope, the set-up has a more complex structure. Motivated by the characteristics of the wave tank, the focus is on water depths that are deep relative to the wave length of the individual waves ($k_0 h \approx 4 \gg 1$, with $k_0 = 2\pi/\lambda_0$ and λ_0 corresponding to the carrier wave length), but a group scale that is intermediate to shallow relative to the water depth: $h/(2\sigma_x) \approx 0.6$, where σ_x is the standard deviation of the approximately Gaussian envelope of the linear surface elevation.

This chapter is structured as follows. First, in §3.2 a multiple-scales solution for crossing groups is compared to existing second-order theory. In §3.3, experimental method is outlined and the three sets of experiments performed are introduced. Then in Chapters 4 and 5 experimental results are presented and compared with theory.

3.2 Second-order theory

In this section, a multiple-scales approach is introduced for the formation of a set-up when two groups cross each other at an angle (§3.2.2) and compared to

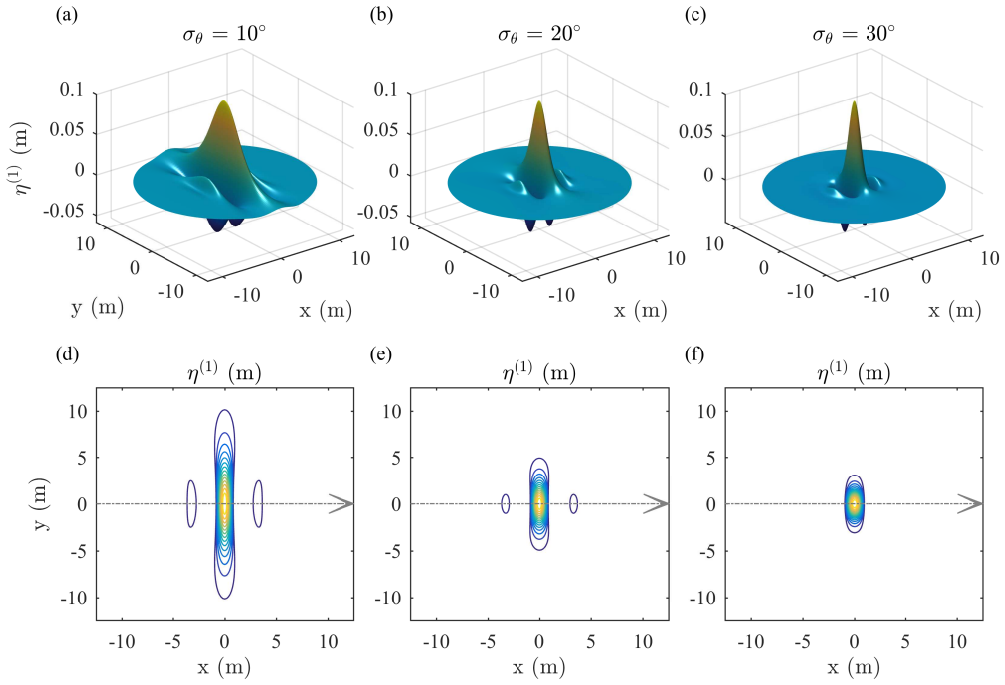

Figure 3.2. Illustration of linear surface profile $\eta^{(1)}(x, y)$ for spreading and surface tests (categories A and B) at time of focus ($t = 0$) and for three different degrees of spreading $\sigma_\theta = 10, 20, 30°$. Panels a-c display the surfaces, and panels d-f corresponding contours, showing positive contours only for clarity (linear amplitude at focus $a_0 = 0.1$ m).

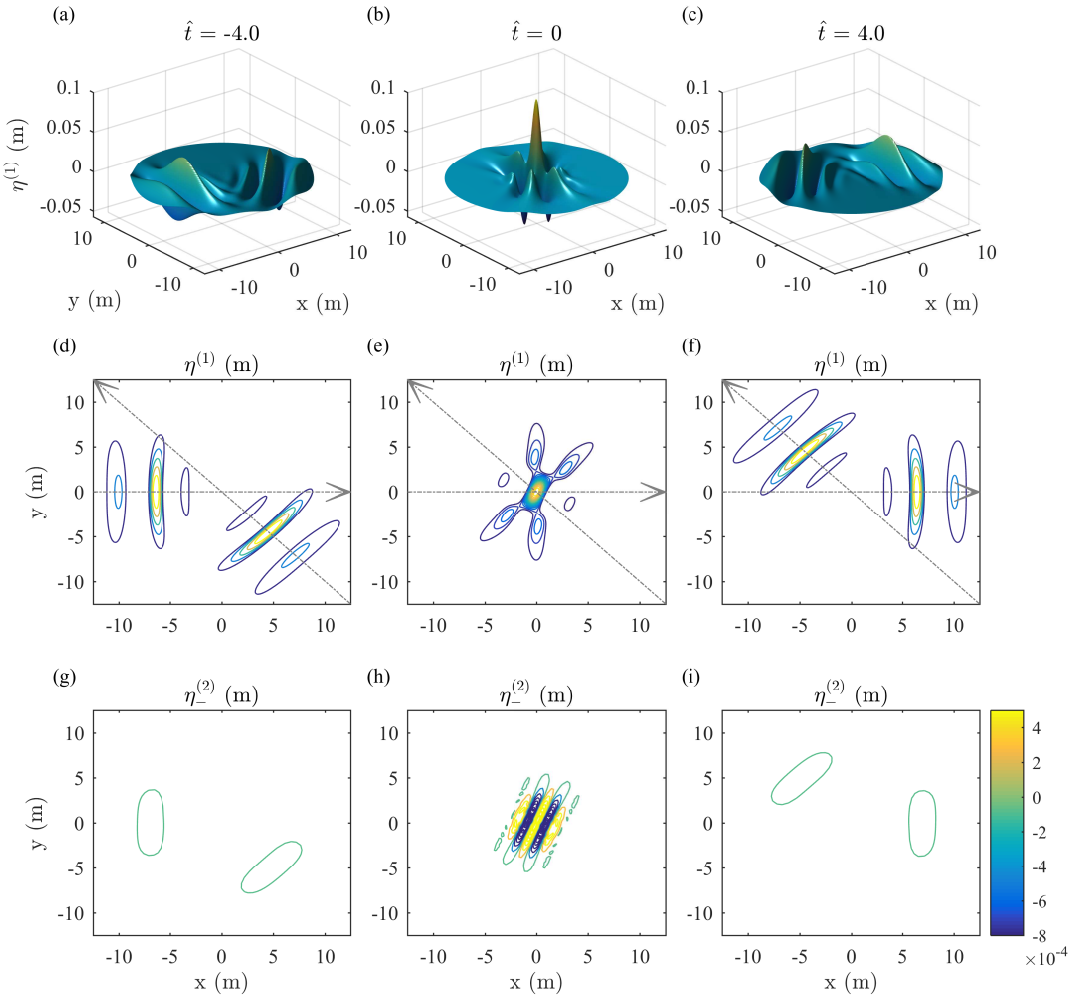

Figure 3.3. Illustration of linear surface profile $\eta^{(1)}(x, y)$ for crossing tests (category C), showing two wave groups with moderate degrees of directional spreading ($\sigma_\theta = 10°$) at a crossing angle of $\Delta\theta = 135°$ for three different times $\hat{t} \equiv c_{g,0}t/\sigma_x$: before focus at $\hat{t} = -4.0$ (left column), at linear focus $\hat{t} = 0$ (middle column), and after focus at $\hat{t} = 4.0$ (third column). Panels a-c display the linear surfaces, and panels d-f corresponding contours, showing positive contours only for clarity (combined linear amplitude at focus $a_0 = 0.1$ m). Panels g-i show the wave-averaged free surface.

the second order model detailed in full in Chapter 2 and briefly revisited here in 3.2.1.

3.2.1 Multi-component second-order theory (review)

By considering the linear signal as the sum of N_k discrete components travelling in N_θ different directions, as previously discussed using complex notation in Chapter 2:

$$\eta^{(1)} = \sum_{n=1}^{N_k} \sum_{i=1}^{N_\theta} D(\theta_i) a_n \cos\left(\varphi_{n,i}\right) \delta k \delta\theta \quad \text{with} \quad \varphi_{n,j} = \mathbf{k}_{n,i} \cdot \mathbf{x} - \omega_n \, t, \tag{3.2}$$

where the wavenumber vector $\mathbf{k}_{n,i} = k_n\big(\cos(\theta_i), \sin(\theta_i)\big)$ has magnitude k_n and angle θ_i measured anti-clockwise from the positive x-axis. Each component satisfies the linear dispersion relationship $\omega_n^2 = g k_n \tanh(k_n h)$, where $\tanh(kh) \approx 1$ for almost all components of the linear spectrum. $D(\theta)$ represents the directional spreading distribution. The coefficients δk and $\delta\theta$ correspond to the magnitude of the discrete steps, so that $\delta k \to dk$ as $N_k \to \infty$ and similarly for $\delta\theta$. The corresponding second-order difference waves that represent the wave-averaged free surface may be calculated as [Dalzell, 1999]:

$$\eta_-^{(2)} = \sum_{n=1}^{N_k} \sum_{m=1}^{N_k} \sum_{i=1}^{N_\theta} \sum_{j=1}^{N_\theta} D(\theta_i) D(\theta_j) a_n a_m B^-(\mathbf{k}_{n,i}, \mathbf{k}_{m,j}, \omega_n, \omega_m, h) \cos\left(\varphi_{n,i} - \varphi_{m,j}\right) (\delta k)^2 (\delta\theta)^2, \tag{3.3}$$

where the interaction kernel B^- is given in Chapter 2.

3.2.2 Separation-of-scales approximation

Under two approximations, that the spectrum is narrow-banded in both frequency and direction, the wave groups can be modelled using the leading-order terms in a multiple-scales expansion[1]. Here $\eta_-^{(2)}$ is approximated as the combination of a set-down η_{SD} and a set-up η_{SU}

$$\eta_-^{(2)} = \underbrace{\eta_{\mathrm{SD,A1A1}} + \eta_{\mathrm{SD,A2A2}} + \eta_{\mathrm{SD,A1A2}}}_{=\eta_{\mathrm{SD}}} + \eta_{\mathrm{SU}}. \tag{3.4}$$

where a set down is associated with the self-interaction of each group:

$$\eta_{\mathrm{SD,A1A1}}(\tilde{x}_1, \tilde{y}_1) = \frac{|a_1|^2}{4h} \frac{1}{\pi\sigma_x^2} \int_{-\infty}^{\infty}\int_{-\infty}^{\infty} \frac{e^{-(\tilde{x}_1^*)^2/\sigma_x^2 - (\tilde{y}_1^*)^2/\sigma_y^2} \tilde{x}_1^*(\tilde{x}_1 - \tilde{x}_1^*)}{(\tilde{x}_1 - \tilde{x}_1^*)^2 + (\tilde{y}_1 - \tilde{y}_1^*)^2} d\tilde{x}_1^* d\tilde{y}_1^*, \tag{3.5}$$

and the cross-interaction of the two groups:

$$\eta_{\mathrm{SD,A1A2}}(\tilde{x}, \tilde{y}) = \frac{1}{4h}\frac{1}{\pi} \int_{-\infty}^{\infty}\int_{-\infty}^{\infty} \frac{1}{g} \frac{\partial F_{\mathrm{A1A2}}(x^*, y^*, t)}{\partial t} \log\Big((x - x^*)^2 + (y - y^*)^2\Big) dx^* dy^*, \tag{3.6}$$

and a set-up also as a result of the cross-interaction of the two groups:

$$\begin{aligned}\eta_{\mathrm{SU}} &= \frac{-1}{g}\overline{\Big(\frac{\partial^2\phi^{(1)}}{\partial z \partial t}\Big|_{z=0}\eta^{(1)} + \frac{1}{2}|\nabla\phi|^2\Big|_{z=0}\Big)} \\ &= \frac{1}{2}(1 - \cos(\Delta\theta))k_0|A_1||A_2| \cos\Big(k_0(\underbrace{x\big(1 - \cos(\Delta\theta)\big) - y\sin(\Delta\theta)}_{=\tilde{x}_1 - \tilde{x}_2}) + \varphi_1 - \varphi_2\Big).\end{aligned} \tag{3.7}$$

[1]The author is grateful to van den Bremer (personal communication) for the derivation of the results, which is based on an extension of van den Bremer and Taylor [2015]. The derivation is reproduced in Appendix A

For $\Delta\theta = 0$ this reduces to the set-down for a single group presented in Chapter 2. Here, the subscripts 1 and 2 refer to properties of the two crossing wave groups, and F_{A1A2} is the mean flow forcing for the interaction of the two groups.

For the experimental parameters considered herein ($\alpha = k_0 a_0 = 0.20$, $\epsilon_x = 1/(k_0\sigma_x) = 0.30$, $k_0 h = 3.9$ and $h/\sigma_x = 1.2$), discussed in more detail in §3.3, figure 3.4 compares the component-by-component solution (3.3) (top panels) to the multiple-scales solution for the set-down (3.5) (bottom panels) for a single wave group, demonstrating good agreement for low degrees of spreading. The mean direction of wave group propagation is left to right in the positive x-direction. For high degrees of spreading, a set-up starts to appear in the form of a ridge along the x-axis that connects the humps in front and behind the group and that is not predicted by the multiple-scales solution (3.5).

Figure 3.5 compares the component-by-component solution (3.3) (top panels) for two crossing groups at four different crossing angles to the multiple-scales expansion (3.4) (bottom row). Also shown are the individual contributions from the set-down (3.5-3.6) in panels e-h and the set-up (3.7) in panels i-l. It is evident from this comparison that the multiple-scales solution can predict the magnitude, but not the exact spatial structure of the set-down for $\Delta\theta = 45°$, as the directional spectra of the group are not clearly separated for low crossing angles. For all larger crossing angles, the two methods agree well as the set-up is dominant.

3.3 Experimental method

This section introduces the experimental setup (§3.3.1), details the input parameters of each category of experiment (§3.3.2), and introduces the method used to isolate the wave-averaged surface elevation from the measured signal (§3.3.3).

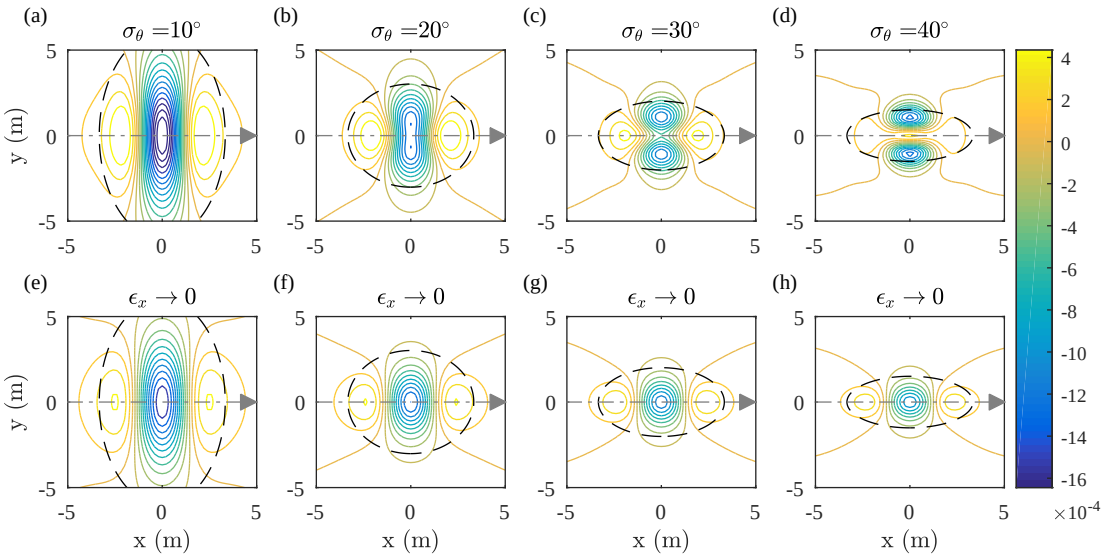

Figure 3.4. Contours of the wave-averaged surface elevation $\eta_-^{(2)}$ for a single group at time of linear focus for different degrees of spreading σ_θ. The panels in the top row (a-d) are computed from multi-component second-order theory (3.3), and the panels in the bottom row (e-h) correspond to the quasi-monochromatic limit (3.5), as denoted by $\epsilon_x \to 0$. The aspect ratio in the quasi-monochromatic limit is computed from $R = \sigma_x/(k_0\sigma_\theta)$, which is asymptotically valid in the limit of a small degree of spreading (R = 0.6, 1.1, 1.7, 2.3 for the four values of σ_θ, respectively). The black dashed lines correspond to two standard deviations (σ_x) from the centre of the group.

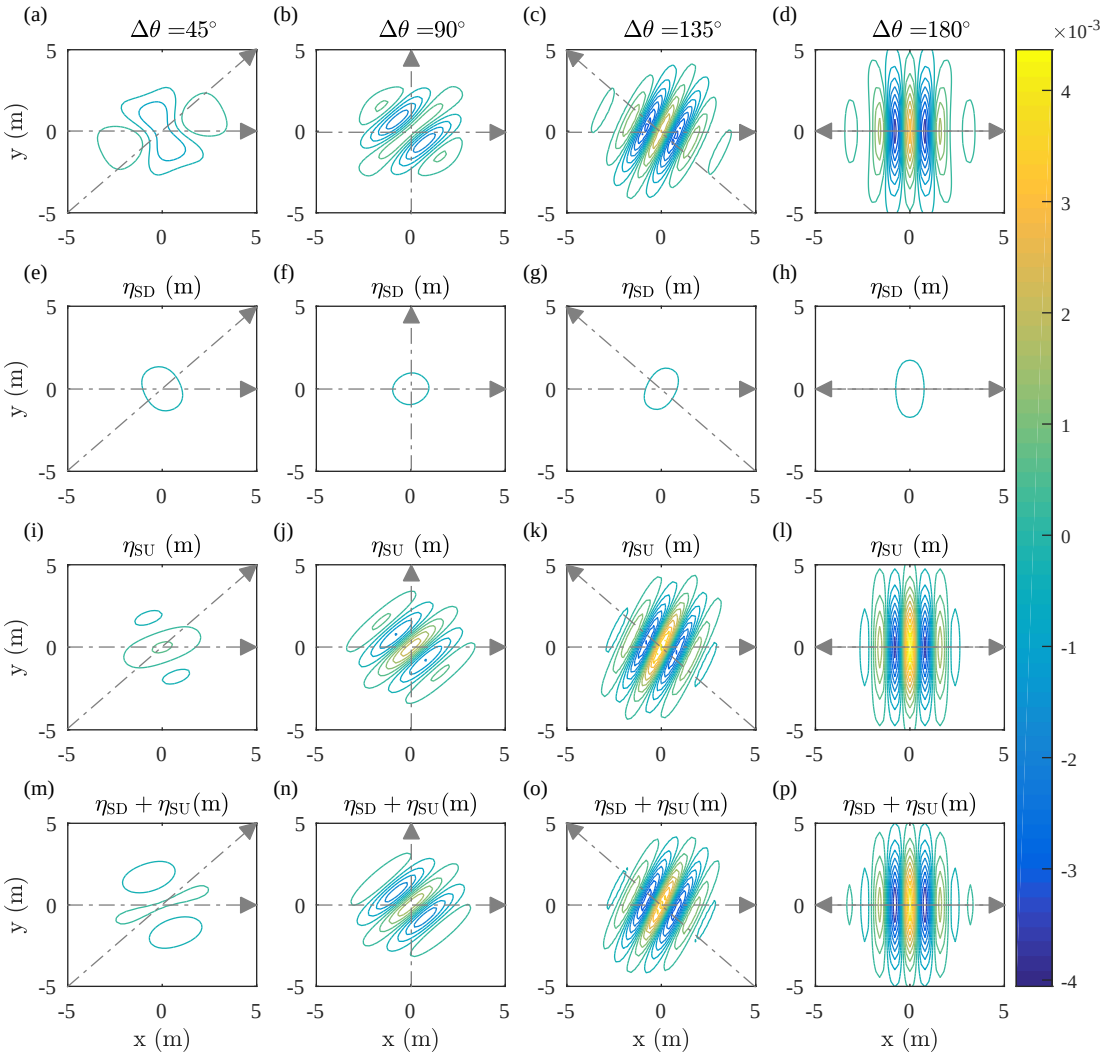

Figure 3.5. Contours of the wave-averaged surface elevation $\eta_-^{(2)}$ for crossing wave groups at time of linear focus for different crossing angles $\Delta\theta$. The panels in the first row (a-d) are computed from multi-component second-order theory (3.3), panels in the second row (e-h) to the set-down in the quasi-monochromatic limit (3.5-3.6), panels in the third row (i-l) to the set-up in the quasi-monochromatic limit (3.7), and panels in the fourth row (m-p) to the sum of the last two. The degree of spreading of the individual groups is $\sigma_\theta = 10°$.

Sections 3.3.4 and 3.3.5 respectively describe the estimation of spectral and directional parameters from the measured signal. Finally, §3.3.6 discusses sources of measurement error and repeatability.

3.3.1 FloWave and gauge layout

The experiments reported on herein were conducted at the FloWave Ocean Energy Research Facility at the University of Edinburgh (c.f. Ingram et al. [2014]). The circular multi-directional wave basin has a 25 m diameter, is 2 m deep, and is encircled by 168 actively-absorbing force-feedback wavemakers, allowing for the creation of waves in all directions. All experiments are of sufficiently short duration for reflections not to play a role. The generation of waves by the wavemakers is based on linear theory. Figure 3.6 shows the layout of the array consisting of 14 capacitance wave gauges within the tank, with gauge locations chosen to combine good spatial resolution, whilst being spaced far enough apart to capture the entire spatial structure of wave-averaged free surface. The wave gauges were calibrated at the start of each day of testing. A settling time of 10 minutes between each test was employed to allow for the absorption of reflected waves.

All of the tests carried out in the foregoing chapters were carried out by the Author. The wavemaker control signal was defined using front files which compose each frequency component to be created in the tank. For each component or wave front, frequency, amplitude, phase, and direction were defined to give the desired linear freesurface elevation at the centre of the tank. The wavemaker software then converted this information into the necessary paddle motion.

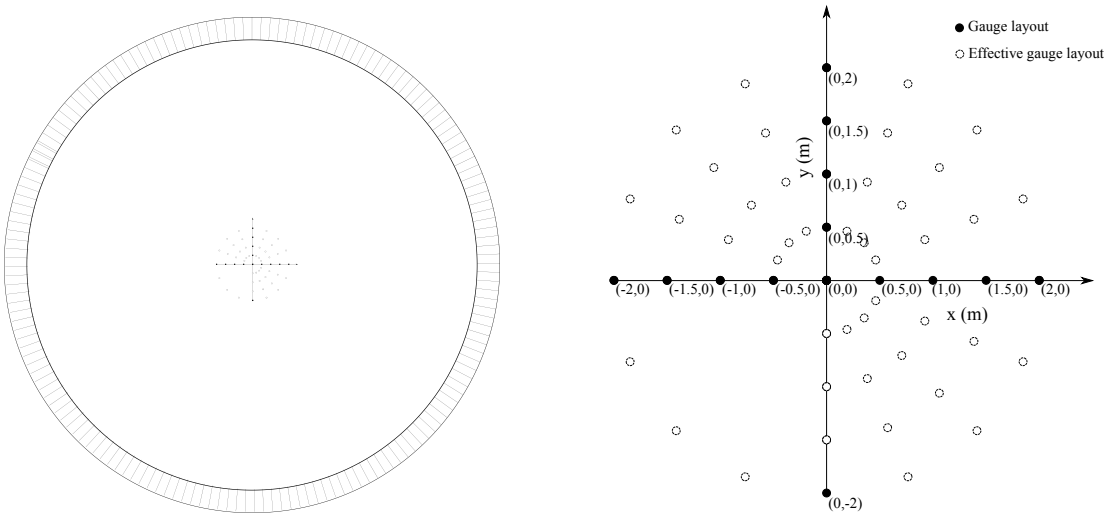

Figure 3.6. Gauge array layout, showing wave gauge locations with respect to the centre of the tank ($x = 0$, $y = 0$). The closed circles denote the location of the 14 gauges with the positive x-axis corresponding to the mean direction of travel of the group (or one of the groups). The open circles denote the effective gauge layout achieved by changing the mean wave direction in steps of 22.5° to map out the set-down/set-up surface (category B).

3.3.2 Matrix of experiments and input parameters

Tests are conducted in three categories: spreading tests (category A), surface tests (category B), and crossing tests (category C), as summarised in table 3.1. In these three categories of test, the degree of directional spreading for a single group is varied (A), the spatial structure of the wave-averaged free surface is mapped (B), and two crossing groups for different crossing angles are considered (C). For all experiments, the input is based on a Gaussian amplitude distribution in wavenumber magnitude $k = |\mathbf{k}|$:

$$\hat{\eta}(k) = \frac{a_0}{\sqrt{2\pi}\Delta k} \exp\Big(-\frac{1}{2}\Big(\frac{k - k_0}{\Delta k}\Big)^2\Big) \qquad \text{for} \qquad 0 \leq k \leq \infty, \tag{3.8}$$

which is converted into the frequency domain using the linear dispersion relationship before being provided as an input to the wavemakers. The peak wavenumber

is set to $k_0 = 2.0$ m^{-1} (based on a peak frequency of 0.7 Hz) and standard deviation is set to $\Delta k = 0.6$ m^{-1}. Although (3.8) only formally corresponds to a group with a Gaussian envelope in real space if k has support on the entire real line (where $k > 0$), $\hat{\eta}(k)$ is negligibly small for $k = 0$ in practice and $\sigma_x = 1/\Delta k = 1.7$ m corresponds to the spatial scale of the group (the standard deviation of the approximately Gaussian group). $\epsilon_x = 0.30$, so the multiple scales approximation will likely hold, but be associated with an error that scales as ϵ_x^2 ($\sim 10\%$). This large value of ϵ_x is chosen, so that the spatial extent of the group is a number of times smaller than that of the tank. This ensures that long second-order error waves associated with the linear paddle motion have time to propagate ahead of the group. There linear waves are always deep ($k_0 d = 3.9$) and the total linear amplitude a_0 is set to 0.1 or 0.15 m corresponding to a steepness of $\alpha = k_0 a_0 = 0.20$ and 0.3. A Gaussian amplitude distribution in angle θ is considered:

$$D(\theta) = \frac{D_0}{\sqrt{2\pi}\sigma_\theta} \exp\Big(-\frac{1}{2}\Big(\frac{\theta - \theta_0}{\sigma_\theta}\Big)^2\Big), \qquad \text{for} \qquad -180^\circ \leq \theta \leq 180^\circ, \tag{3.9}$$

where θ_0 is the mean direction and σ_θ is a measure of the degree of directional spreading. The spreading distribution is truncated at -180° and $+180^\circ$ and the normalization coefficient D_0 chosen so that the integral of $D(\theta)$ is unity over this range. For small degrees of spreading, σ_θ corresponds to the root-mean-squared spreading value. For crossing wave groups two spectra with differing values of θ_0 are superimposed. It its emphasised that there is a difference between σ_θ and the usual energy spectrum directional spreading parameter which is equal to $\sigma_\theta/\sqrt{2}$.

A - Spreading tests

First, tests are carried out to assess the relationship between the degree of directional spreading σ_θ, and the amplitude and sign of the wave-averaged surface elevation for focused wave groups. The degree of directional spreading σ_θ is

Category	Test numbers	a_0 (m)	σ_θ (.deg)	θ_0 (.deg)	$\Delta\theta$ (.deg)
A. Spreading	A.1-13	0.1	0-90 (at 10), 135, 180, 360	0	0
	A.14-19	0.15	0-50 (at 10)	0	0
B. Surface	B.1-3	0.1	20, 30, 40	0-90 (at 22.5)	0
	B.4	0.15	40	0-90 (at 22.5)	0
C. Crossing	C.1-3	0.1	10, 20, 30	0	45-180 (at 45)
	C.4	0.15	20	0	45-180 (at 45)

Table 3.1 Matrix of experiments.

varied in the range 0-360°. For groups with an amplitude of $a_0 = 0.1$ m and in the range σ_θ =0-50° for an increased amplitude of $a_0 = 0.15$ m. In practice $\sigma_\theta = 360°$ corresponds to the case where the directional spectrum has almost fully saturated ($\sigma_\theta \to \infty$ corresponds to axisymmetric spreading: the variation of $D(\theta)$ as a function of θ is less than 7% for $\sigma_\theta = 360°$). The difference in the amplitude of wave-averaged surface elevation between $\sigma_\theta = 360°$ and $\sigma_\theta \to \infty$ is negligible ($< 0.1\%$).

B - Surface tests

Here, tests from category A are repeated in order to perform spatial measurements of surface elevation. By varying the mean direction of propagation from 0 to 90° and repeating tests at intervals of 22.5°, the spatial structure of the wave-averaged surface elevation is captured using the axial gauge array (see figure 3.6) for single directionally spread wave groups. The wave-averaged free surface is mapped for $\sigma_\theta = 20, 30, 40°$ (and at an increased amplitude of $a_0 = 0.15$ m for $\sigma_\theta = 40°$). In doing so, the spatial structure of the wave-averaged free surface dominated by the set-down, the set-up, and the transition between these as a function of σ_θ is captured.

C - Crossing tests

Finally, tests are carried out to assess the relationship between the crossing angle $\Delta\theta$ of two directionally spread focused wave groups, and the set up or down of the wave-averaged surface elevation. The crossing angle $\Delta\theta$ of the wave groups is varied between 0 and 180° at 45° intervals. This is repeated for groups with directional spreading of $\sigma_\theta = 10, 20, 30°$ and $a_0 = 0.1$ m (and for an increased amplitude of $a_0 = 0.15$ m at $\sigma_\theta = 20°$).

3.3.3 Harmonic separation

In order to observe the set-up/down of wave groups and other nonlinear harmonics, these components must be be extracted from the fully nonlinear signal measured by the gauges. As illustrated in Chapter 7 this can be achieved for second-order difference components by a process of filtering and minimising skewness [Walker et al., 2004]. However, this approach may not be extended as effectively to other nonlinear harmonics components. This approach also requires harmonic components to be well separated in the frequency domain. An alternative approach that is possible for physical and numerical testing, is to repeat experiments with a phase shift, the phase shifted measurements can then be used to separate out harmonics. The number of phase shifts carried out determines the combination of harmonics that can be extracted.

Two-phase harmonic extraction

Waves of non-zero amplitude are nonlinear, their nonlinearity is proportional to steepness $\alpha = ka$. This nonlinearity may be expressed in harmonic terms as a

Stokes-type perturbation in orders of α:

$$\begin{aligned}\eta = &\alpha\eta^{(1)} \\ &+ \alpha^2\eta^{(2,0)} + \alpha^2\eta^{(2,2)} \\ &+ \alpha^3\eta^{(3,1)} + \alpha^3\eta^{(3,3)} \\ &+ \alpha^4\eta^{(4,0)} + \alpha^4\eta^{(4,2)} + \alpha^4\eta^{(4,4)} \\ &+ O(\alpha^5),\end{aligned} \tag{3.10}$$

The first superscript denotes the relevant powers of steepness and the second the frequency harmonic. At second order in steepness, bound waves $\eta^{(2,0)}$ and $\eta^{(2,2)}$ occur at the difference and sum of the interacting free wave components $\eta^{(1)}$, and herein are denoted as $\eta_-^{(2)}$ and $\eta_+^{(2)}$ respectively. By repeating experiments and changing the phases of the harmonic components by 180° between experiments, terms in (3.10) of odd and even powers may be extracted:

$$\eta_{odd} = \eta^{(1)} + \eta^{(3,1)} + \eta^{(3,3)} = \frac{\eta_0 - \eta_{180}}{2}, \tag{3.11}$$

$$\eta_{even} = \eta^{(2,0)} + \eta^{(2,2)} + \eta^{(4,0)} + \eta^{(4,2)} + \eta^{(4,4)} = \frac{\eta_0 + \eta_{180}}{2}. \tag{3.12}$$

where crest focused and trough focused repeat experiments are η_0 and η_{180} [Baldock et al., 1996].

To extract individual harmonic components from the odd and even harmonics filtering in the frequency domain must be carried out. When separated into odd and even harmonics the individual harmonic components are better defined in the frequency domain as illustrated by figure 3.7 significantly aiding their extraction.

Four-phase harmonic extraction

Figure 3.8 illustrates the results of two phase harmonic extraction. While this method successfully separates out odd and even harmonics, the individual sum $\eta_+^{(2)}$ and difference $\eta_-^{(2)}$ harmonic terms contained within may overlap for higher-bandwidth signals. Carrying out two additional phase shifts at 90 and 270^o allows for the isolation of the following harmonics [Fitzgerald et al., 2014],

$$\eta^{(1,1)} + \eta^{(3,1)} = \frac{\eta_0 - \tilde{\eta}_{90} - \eta_{180} + \tilde{\eta}_{270}}{4}, \tag{3.13}$$

$$\eta^{(2,2)} + \eta^{(4,2)} = \frac{\eta_0 - \eta_{90} + \eta_{180} - \eta_{270}}{4}, \tag{3.14}$$

$$\eta^{(3,3)} = \frac{\eta_0 + \tilde{\eta}_{90} - \eta_{180} - \tilde{\eta}_{270}}{4}, \tag{3.15}$$

$$\eta^{(2,0)} + \eta^{(4,0)} + \eta^{(4,4)} = \frac{\eta_0 + \eta_{90} + \eta_{180} + \eta_{270}}{4}. \tag{3.16}$$

For small values of α, 3rd and 4th order terms will be much smaller than 1st and 2nd, in such cases the linear and second-order waves may be observed without the need for filtering. If α is large and filtering is necessary, individual harmonics are better defined in the frequency domain than using two phase extraction, as shown in 3.7.

Twelve-phase harmonic extraction

It is desirable to separate individual harmonic terms without filtering, as it introduces a degree of uncertainty. Hann et al. [2014] use twelve phase shifts from $0 - 330^o$ in steps of 30^o, to extract combinations of the 0th order

$$\eta^{(2,0)} + \eta^{(4,0)} = \frac{\eta_0 + \eta_{30} + \eta_{60} + \eta_{90} + \eta_{120} + \eta_{150} + \eta_{180} + \eta_{210} + \eta_{240} + \eta_{270} + \eta_{300} + \eta_{330}}{12}, \tag{3.17}$$

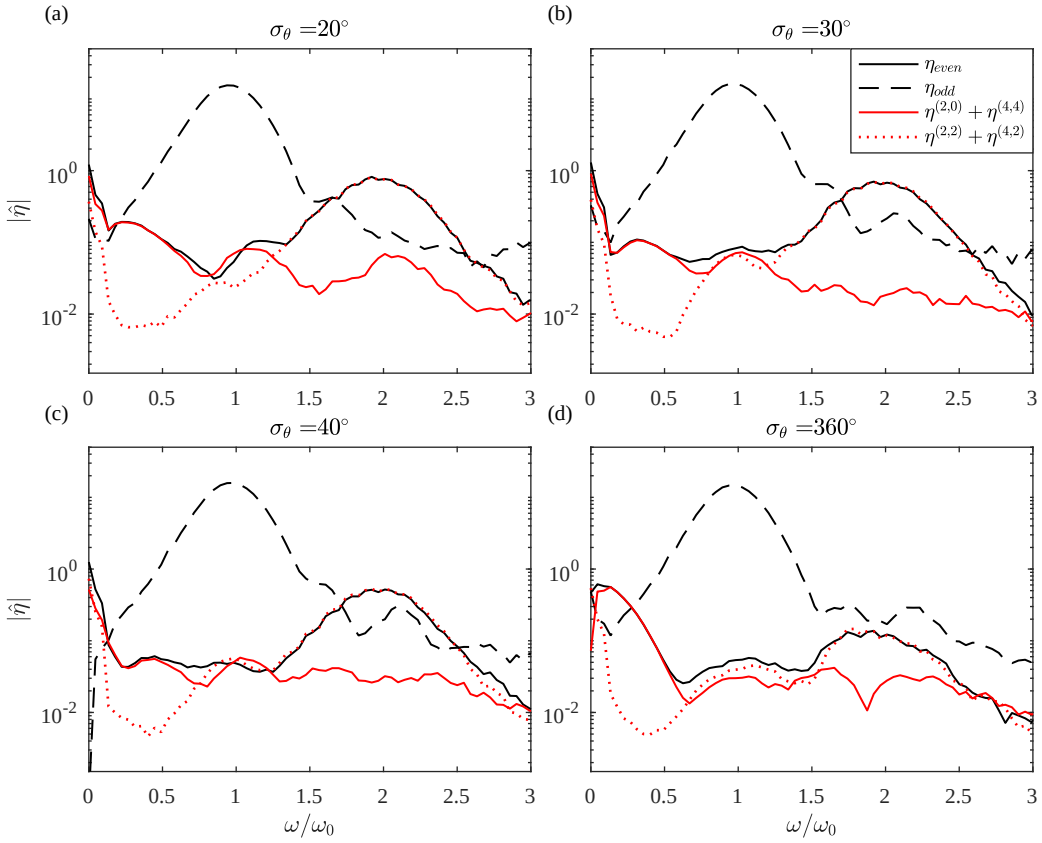

Figure 3.7. Log-scale amplitude spectra of extracted harmonic components produced using two and four phase extraction methods; two phase results (black lines), and four phase results (red lines). The different panels correspond to increasing degrees of input directional spreading $\sigma_\theta = 20, 30, 40, 360°$.

1st order

$$\eta^{(1,1)} + \eta^{(3,1)} = \frac{\eta_{30} + \eta_{330} - \eta_{150} - \eta_{210}}{2\sqrt{3}}, \tag{3.18}$$

2nd order

$$\eta^{(2,2)} + \eta^{(4,2)} = \frac{\eta_{120} + \eta_{240} - \eta_{60} - \eta_{300}}{4} + \frac{\eta_{30} + \eta_{330} - \eta_{150} - \eta_{210}}{4\sqrt{3}}, \tag{3.19}$$

3rd order

$$\eta^{(3,3)} = \frac{\eta_{30} + \eta_{330} + \eta_{150} + \eta_{210} - \eta_{60} - \eta_{300} - \eta_{120} - \eta_{240}}{4}, \tag{3.20}$$

and 4th order terms

$$\eta^{(4,4)} = \frac{\eta_0 + \eta_{90} + \eta_{180} + \eta_{270}}{4} - \left(\eta^{(2,0)} + \eta^{(4,0)}\right). \tag{3.21}$$

This method further separates the terms without filtering. However, not all harmonics are isolated.

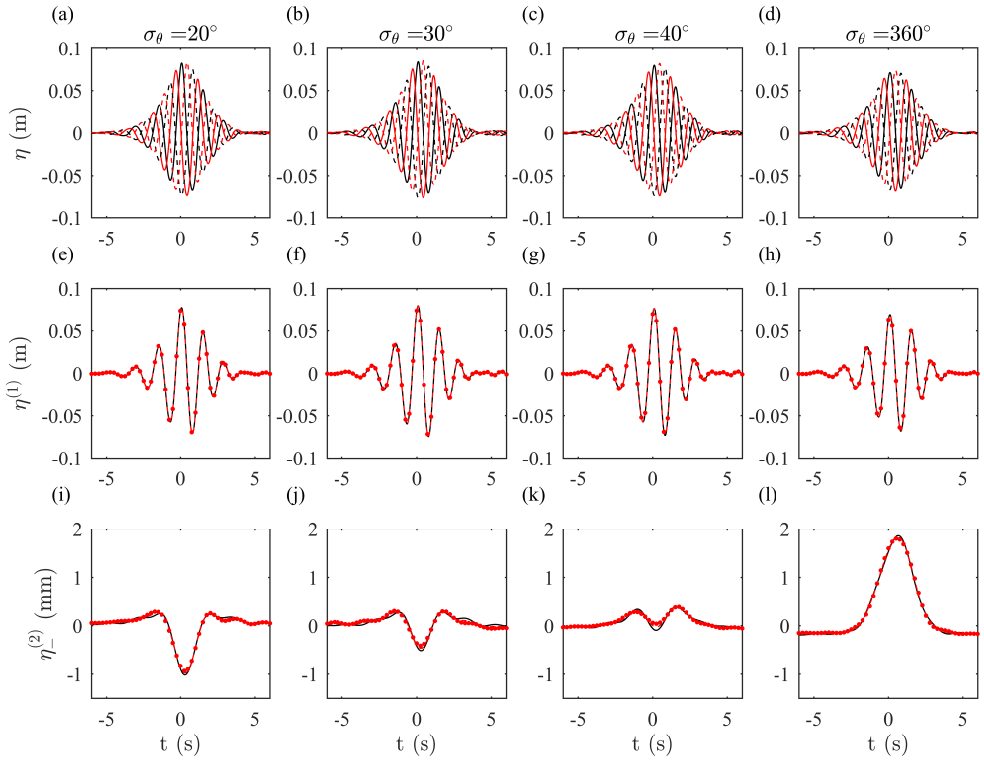

Figure 3.8. Results of four-phase harmonic extraction for degrees of spreading $\sigma_\theta = 20, 30, 40, 360°$: measured time series η_{0-270} at central probe ($x = 0$, $y = 0$) (panels a-d); $\varphi = 0°$ (black line), $\varphi = 90°$ (red line), $\varphi = 180°$ (black dashed line), and $\varphi = 270°$ (red dashed line). Extracted linear waves $\eta^{(1)}$ (panels e - h), and difference waves $\eta^(2)_-$ (panels i - j); two-phase method (black line); four-phase method (red dots).

Experimental results

When carrying out physical tests, running multiple repeats for each experiment is time consuming and costly, and with each method of harmonic extraction there is a diminishing return. The degree of nonlinearity and hence the size of the higher order harmonic terms dictates the necessity of employing additional phase shifts. Other aspects such as the broad-bandedness of waves will also effect the ease of harmonic extraction.

σ_θ (.deg)	a_0 (m)	k_0 (m^{-1})	Δ_k	φ (.deg)
20	0.1	1.97	0.6	0,90,180,270
30	0.1	1.97	0.6	0,90,180,270
40	0.1	1.97	0.6	0,90,180,270
360	0.1	1.97	0.6	0,90,180,270

Table 3.2 Harmonic separation experimental test matrix

In order to assess the optimal approach of harmonic extraction, initial experiments were undertaken for a range of directionally spread wave groups with phase shifts of $0, 90, 180$, and 270^o. As waves become more directionally spread their resulting wave-averaged surface elevation changes. For focused wave groups the second-order difference waves $\eta_-^{(2)}$ initially form a set-down under the group, and as spreading increases this becomes a set-up. This change occurs at values of spreading around $30 - 40^o$, and at these values of spreading the difference waves may be very small and difficult to isolate. Therefore, tests were carried out at values of $20, 30, 40$, and 360^o. Where, 360^o was selected as an extreme case because under such large spreading wave-averaged surface elevation is drastically different. Table 3.2 details the experiments carried out.

Figure 3.8 compares the results of two and four phase harmonic separation of $\eta_-^{(2)}$ and $\eta^{(1)}$, plotted in black and red respectively. It is clear that both methods agree very well for the conditions tested. In light of this and constraints on testing time, herein each experiment will be repeated at 180°. It should be noted that the inversion of phase is unaffected by cubic nonlinear interactions, so perfect phase focusing is not required for these methods of harmonic extraction.

3.3.4 Estimation of spectral parameters

As the input spectrum is in wavenumber magnitude $\hat{\eta}(k)$, and the measurements are in time, the resulting Fourier transform $\hat{\eta}(\omega)$ must be converted in order to estimate spectral parameters as follows:

$$\hat{\eta}(k) = \hat{\eta}(\omega(k))\frac{d\omega(k)}{dk}, \tag{3.22}$$

where $\omega(k) = \sqrt{kg \tanh kh}$. The carrier wavenumber $k_0^\star$ is estimated as wavenumber of the spectral peak of the linear spectrum. The linear amplitude $a_0^\star$ is estimated by taking the 0-th moment of the of the measured linear wavenumber spectrum:

$$a_0^\star = \int_0^\infty \hat{\eta}(k)dk. \tag{3.23}$$

The spectral bandwidth Δk is then estimated using the variance of the observed spectrum:

$$Var(k) = \frac{1}{a_0^\star}\int_0^\infty \hat{\eta}(k)(k-k_0^\star)^2 dk, \qquad \text{and} \quad \Delta k^\star = \sqrt{Var(k)}. \tag{3.24}$$

The symbol $\star$ is used throughout to indicate parameters estimated from measurements, as distinct from values provided as inputs to the wavemakers.

3.3.5 Estimation of measured directional spectrum

In the all of the foregoing experiments, the degree of directional spreading is of primary concern, and so it is therefore necessary to estimate the actual degree of directional spreading $\sigma_\theta^\star$ experienced for each experiment. The non-ergodic nature of the experiments considered herein makes estimates generated using maximum likelihood and entropy methods inappropriate (cf. Krogstad [1988], Benoit et al.

[1997]). Instead, a least squares approach is adopted where $\sigma_\theta^\star$ is identified as the value that minimizes the difference between the measured $\eta_M^{(1)}$ and predicted $\eta_T^{(1)}$ linear time series. The predicted time series $\eta_T^{(1)}$ at each probe is calculated using the Fourier transform $\hat{\eta}_M^{(1)}$ of the time series observed at the central probe, which is propagated in space using linear wave theory,

$$\eta_T^{(1)}(\mathbf{x_p}, t) = \mathrm{Re}\left[\sum_{n=1}^{N_k}\sum_{i=1}^{N_\theta} D(\theta_i)\hat{\eta}_{M,n}^{(1)} \exp(-\imath(\omega_n t - \mathbf{k}_{i,n}\cdot\mathbf{x}_p))\delta k\delta\theta\right] \tag{3.25}$$

where $\mathbf{x_p}$ is the location of probe p, and $D(\theta)$ is the assumed spreading distribution as a function of the parameter σ_θ to be identified. The least squares estimate of spreading is then found as

$$\sigma_\theta^\star \in \arg\min \sum_{p=1}^{N_p} \int_{-\frac{6\sigma_x}{C_{g,0}}}^{\frac{6\sigma_x}{C_{g,0}}} \left(\eta_M^{(1)}(\mathbf{x}_p, t) - \eta_T^{(1)}(\mathbf{x}_p, t)\right)^2 dt. \tag{3.26}$$

The integral limits are set to $\pm 6\sigma_x/c_{g,0}$ to capture the passage of the entire wave group, focussed at $t = 0$, and minimize the influence of any reflections. This approach assumes that components of equal frequency are in phase at the central probe; this is valid providing there is not significant modification to the linear dispersion of free waves from the paddles to the observation points through cubic wave-wave interactions, as the waves travel from the paddles to the observation points.

Figure 3.9 illustrates the results of (3.26), for test A.15, which had inputs $\sigma_\theta = 10°$ and $a_0 = 0.15$ m. This figure shows the measured and predicted linear time series for $\sigma_\theta^\star$ at all 14 probes. Test A.15 exhibits the largest difference between measured and predicted time series of the spreading tests; despite this, it is clear that the the above method is successful in reproducing the time series at each probe and hence is providing a reasonable estimate of the degree of directional spreading.

Here, the greatest disagreement is observed for the first nine time series (panels a to i), these panels run along the x-axis as shown in figure 3.6, this may be a result of cubic wave-wave interaction as the measured waves become slightly steeper than linear predictions as they propagate forwards. This is also observed for the unidirectional increased amplitude test test A.14, which supports this hypothesis.

As already mentioned, in this set of experiments the degree of spreading is a crucial parameter; to assess the uncertainty associated with the above method of spreading estimation a boot-strapping method is used. This approach re-samples a limited number of the total measurements performing the estimation multiple times. This then produces a larger sample of spreading estimates from which an estimate of uncertainty may be made. Here 14 wave gauges are used, sampling all possible combinations of 7 out the 14 probes (excluding the central probe) produces 1716 (= 13!/(7!6!)) estimates of $\sigma_\theta^\star$. Plotting these estimates as histograms and fitting a Gaussian distribution gives an estimate of the uncertainty associated with estimating directional spreading. Figures 3.10 to 3.12 present the results of re-sampling $\sigma_\theta^\star$. For all tests the mean of re-sampled $\sigma_\theta^\star$ is the same as $\sigma_\theta^\star$ calculated using all probes. The standard deviation of estimates is $\Delta\sigma_\theta^\star \approx 1^\circ$. For tests with larger values of $\sigma_\theta^\star$ the spread of results goes up (figure 3.10), because at large values of $\sigma_\theta^\star$ the directional spectrum is almost saturated so that changes in $\sigma_\theta^\star$ have a small effect on the shape of the spreading distribution. Estimated degree of directional spreading $\sigma_\theta^\star$ is used to calculate the theoretical wave-averaged surface elevation, hence any error in $\sigma_\theta^\star$ is propagated to $\eta_{T-}^{(2)}$; the affect this has wave-averaged surface elevation is discussed in §3.3.6.

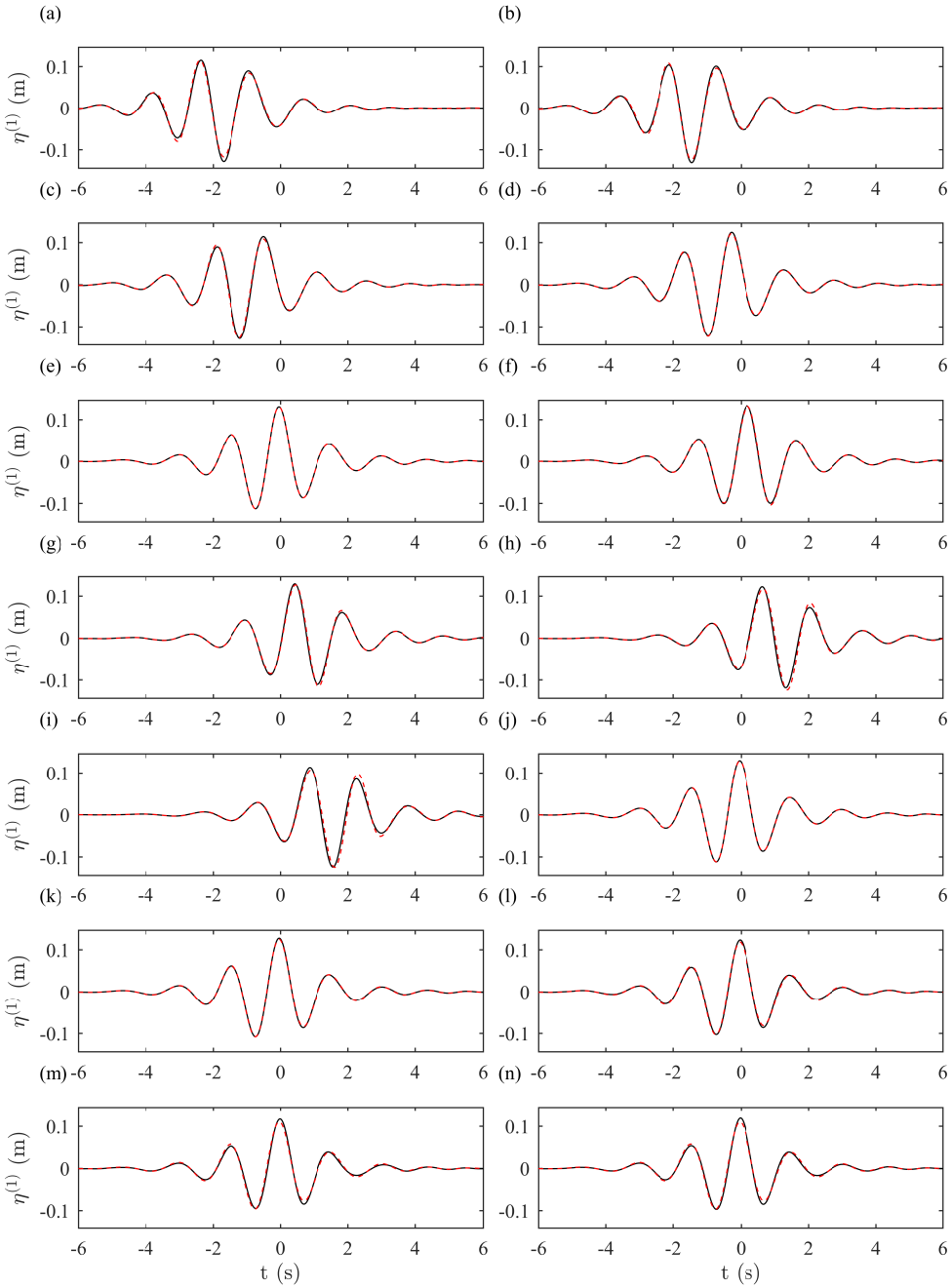

Figure 3.9. Measured $\eta_M^{(1)}$ (black lines) and predicted $\eta_T^{(1)}$ (red dashed lines) linear time series produced in the estimation of the degree of directional spreading $\sigma_\theta^\star = 7.8°$, where input spreading is $\sigma_\theta = 10°$ and $a_0 = 0.15$ m. Panels a to n correspond to probes 1 to 14.

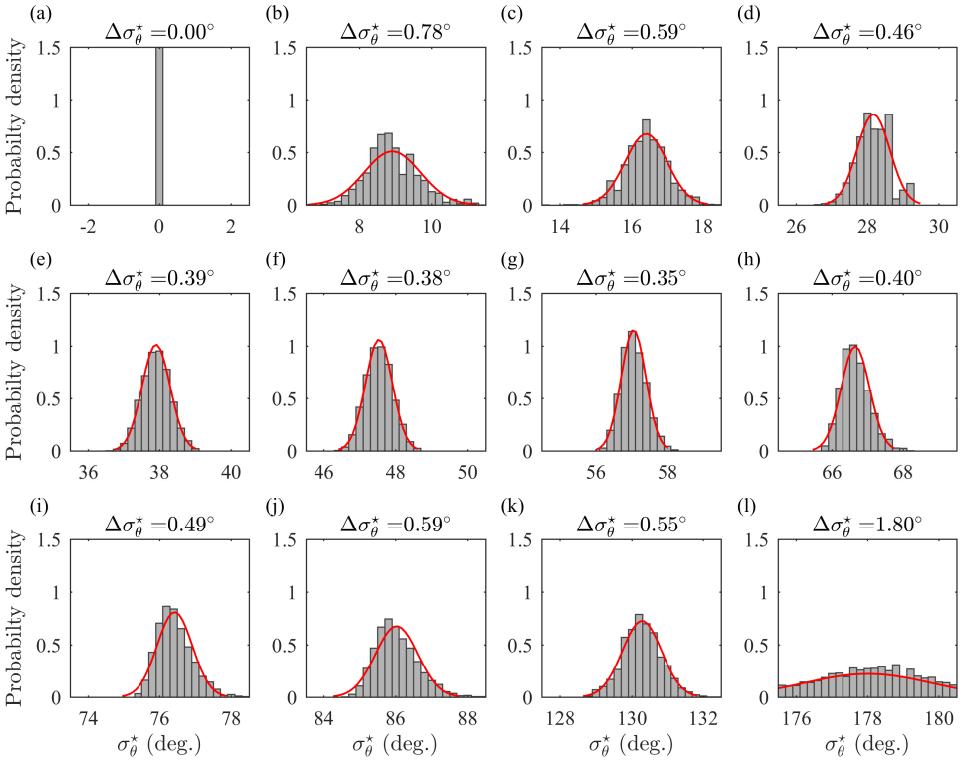

Figure 3.10. Quantification of uncertainty in spreading estimation for spreading tests, panels show histograms of resampled spreading estimates for input degree of spreading $\sigma_\theta = 0 - 180°$ (tests A1.-A.12), and fitted Gaussian distribution (red line).

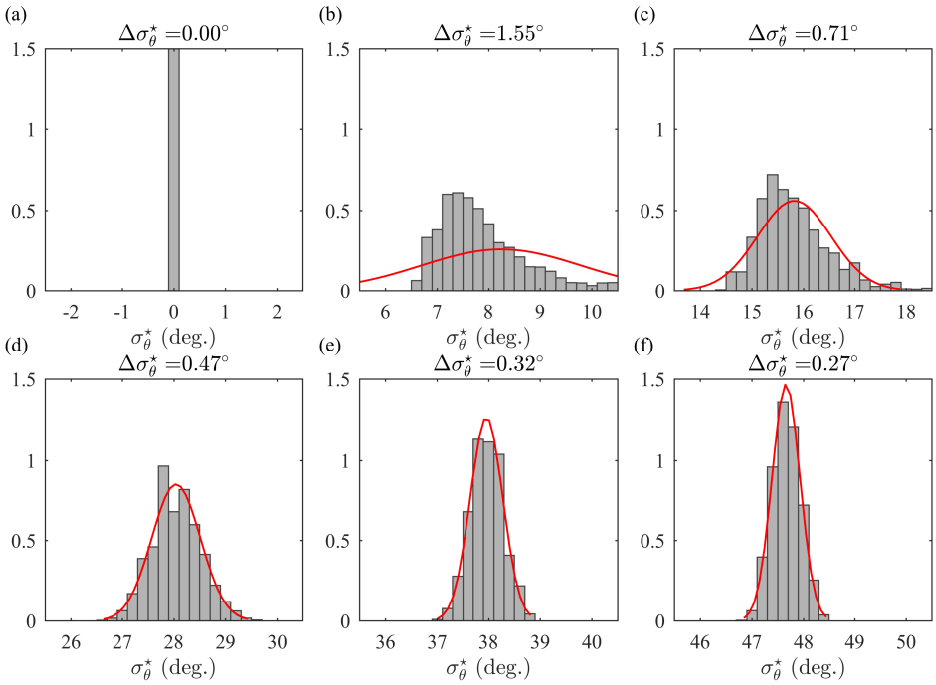

Figure 3.11. Quantification of uncertainty in spreading estimation for spreading tests The different panels correspond to increasing degrees of input spreading $\sigma_\theta = 0 - 50°$, and the captions denote the estimated degree of spreading $\sigma_\theta^\star$.

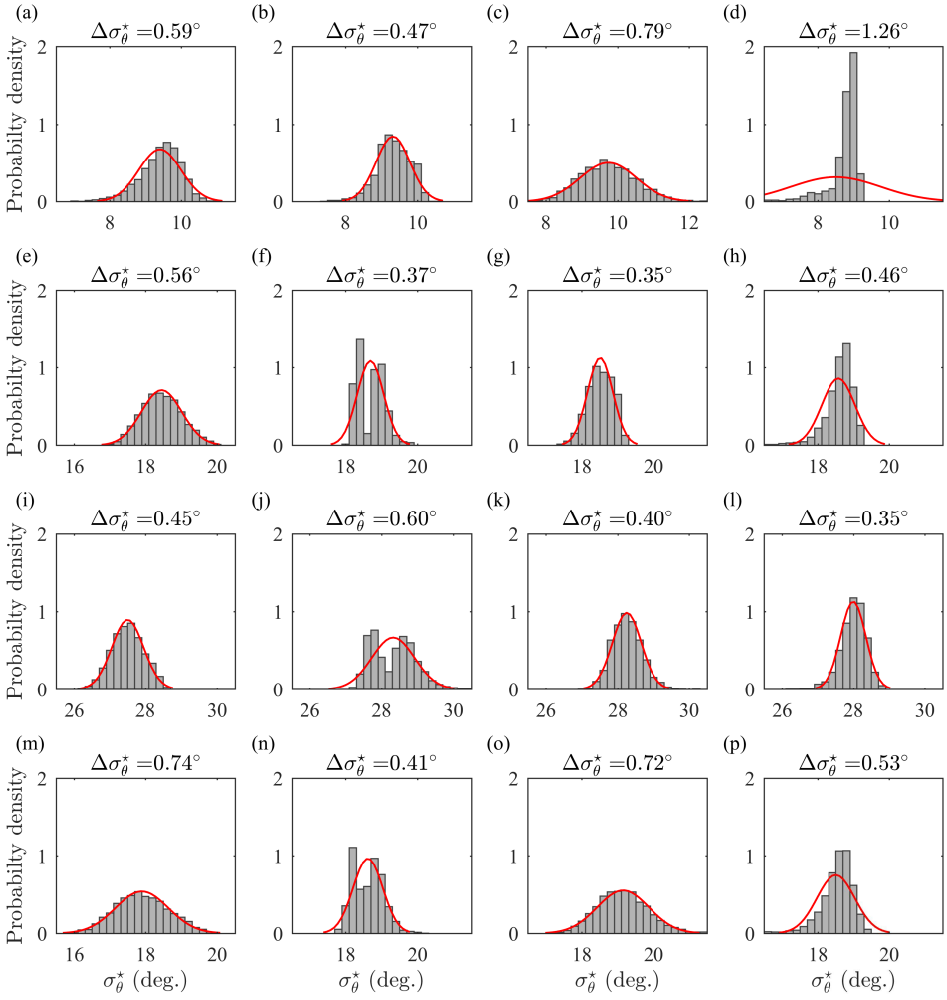

Figure 3.12. Quantification of uncertainty in spreading estimation for spreading tests, panels show histograms of resampled spreading estimates. The different panels correspond to increasing values of crossing angle $\Delta\theta = 0 - 180°$ for degrees of input spreading $\sigma_\theta = 10, 20, 30°$, and the captions denote the estimated degree of spreading $\sigma_\theta^\star$.

	Description	Test parameters	Test numbers	Error ± $\eta_-^{(2)}$ (mm)	Error ± $\eta_-^{(2)}/(\lvert a_0^\star\rvert^2 k_0^\star)$
I.	Residual tank motion $\Delta\eta_I$	-	-	0.50	-
	Low-pass filtered $\Delta\eta_I$	-	-	0.025	0.0013
II.	Two standard deviations of the	$\sigma_\theta = 20°$	A.3, A.3†, B.1.1	0.080	0.0068
	measured wave-averaged surface	$\sigma_\theta = 30°$	A.4, A.4†, B.2.1	0.14	0.01
	amplitude $a_{M-}^{(2)}$ from repeated	$\sigma_\theta = 40°$	A.5, A.5†, B.3.1	0.16	0.012
	tests $\Delta\eta_{II}$	$\sigma_\theta = 360°$	A.13, A.13†	0.11	0.01
		$\sigma_\theta = 40°$, $a_0 = 0.15$m	A.18, B.4.1	0.023	0.00075
III.	Two standard deviations of the	$\sigma_\theta = 20°$	B.1.1-B.1.5	0.38	0.032
	measured wave-averaged surface	$\sigma_\theta = 30°$	B.2.1-B.2.5	0.24	0.017
	amplitude $a_{M-}^{(2)}$ from surface	$\sigma_\theta = 40°$	B.3.1-B.3.5	0.10	0.0076
	tests $\Delta\eta_{III}$	$\sigma_\theta = 40°$, $a_0 = 0.15$m	B.4.1-B.4.5	0.43	0.014
IV.	Mean error in $a_{T-}^{(2)}$ associated	$a_0 = 0.1$m	A.1-A.13	0.055	0.0044
	with estimating $\sigma_\theta^\star$ $\Delta\eta_{III}$	$a_0 = 0.15$m	A.14-A.19	0.28	0.0086
		$a_0 = 0.1$m	C.1-C.12	0.047	0.0035
		$a_0 = 0.15$m	C.13-C.16	0.11	0.0035
V.	Gauge calibration error of central probe (mean $a_0^\star$ and $k_0^\star$ used)	-	-	0.4	0.033

Table 3.3. Quantification of errors in the wave-averaged free surface $\eta_-^{(2)}$ († denotes tests which were repeated with additional 90° and 270° phase shifts.)

3.3.6 Sources of error

Chapters 4 and 5 present individual results for test categories A-C. However, in carrying out the matrix of experiments presented table 3.1 a number of tests were repeated, allowing for the repeatability of forgoing experiments to be assessed. In addition to the variation between repeat experiments, table 3.3 summarizes the leading sources of error (I-V).

Unabsorbed reflections (Error measure I)

In order to capture the effect of waves that are not fully absorbed by the wavemakers and remain present in the tank throughout the tests, the variation in the surface elevation is measured after the 10 min of settling time between

experiments. Specifically, $\Delta\eta_I$ is defined as the difference between the maximum and the minimum surface elevation in the 32 s window before tests. In order to assess the effect of this residual tank motion on the error in the wave-averaged free surface, the same low-pass filter is applied to the residual motion.

Repeatability (Error measures II and III)

To quantify the repeatability of tests (error measure II), $\Delta\eta_{II}$ reports two times the standard deviation of the maximum measured wave-averaged surface amplitude $a^{(2)}_{M-}$ across a number of tests that have been repeated two or three times. Similarly, whilst performing the surface tests (category B), only the mean direction of the wave group was varied. The measurements at the central probe that are thus repeated five times can be used to quantify azimuthal imperfection of the wavemakers and gauge location (error measure III). Two times the standard deviation of the measured wave-averaged surface amplitude $a^{(2)}_{M-}$ for these repeat tests is reported as the error in $\Delta\eta_{III}$.

Estimation of directional spreading (Error measure IV)

Error in the predicted value of wave-averaged surface amplitude $a^{(2)}_{T-}$ that arises from the estimation of the degree of directional spreading $\sigma^\star_\theta$ from the linearized signal is also considered. The estimates of $\sigma^\star_\theta$ in tables 4.1-5.1 are obtained from (3.26) using all fourteen probes. Estimating $\sigma^\star_\theta$ using fewer than fourteen probes, allows for multiple estimates of $\sigma^\star_\theta$ using different combinations of probes. Here, we use combinations of seven of the fourteen probes (excluding the central probe). This allows for 1716 (= 13!/(7!6!)) estimates of $\sigma^\star_\theta$, from which we can compute a standard deviation $\Delta\sigma^\star_\theta$ (see §3.3.5). To avoid the time-consuming computation of

the wave-averaged free surface amplitude $a_{T-}^{(2)}$ for all estimates of $\sigma_\theta^\star$, we compute upper and lower bounds of $a_{T-}^{(2)}$ using $\sigma_\theta^\star - 2\Delta\sigma_\theta^\star$ and $\sigma_\theta^\star + 2\Delta\sigma_\theta^\star$ and report the average difference with the mean as the error measure $\Delta\eta_{IV}$. It should be noted that the means of the re-sampled spreading estimates agree with the value obtained using all fourteen probes, demonstrating that the estimator (3.26) is unbiased. The error in $a_{T-}^{(2)}$, that results from estimation of $\Delta\sigma_\theta^\star$ for test categories A and C is listed in Tables 3.4 and 3.5.

Wave gauge calibration (Error measure V)

Finally, the error associated with wave gauge calibration is calculated. The gauges were calibrated by positioning them at known heights in still water and fitting a linear relationship to the resulting measured voltage. Two times the standard deviation of the predicted values of height z is taken as the calibration error $\Delta\eta_V$.

The estimated error in the wave-averaged free surface associated with residual tank motion (error measure I) was small ($\pm$0.025 mm). The repeatability of experiments was found be extremely high (error measure II), with exact repeats of the same experiment giving an error in the maximum amplitude of the wave-averaged free surface between repeats of 0.023-0.14 mm. The measure of error is defined to be two times the standard deviation in all cases. A more substantial error in the wave-averaged free surface of 0.1-0.38 mm ($a_0 = 0.1$ m) and 0.43 mm ($a_0 = 0.15$ m) (two standard deviations) is identified when the same experiments are repeated, but the main direction of travel of the group is varied, reflecting slight azimuthal asymmetry in the wavemaker configuration or the gauge layout. From repeated re-sampling from 14 probes an error in the wave-averaged free surface amplitude, resulting from an error in $\sigma_\theta^\star$, of 0.047-0.28 mm ($a_0 = 0.1$ m) and 0.3-0.7 mm ($a_0 = 0.15$ m) is obtained. Underlying all these sources of error, is most likely the error associated with wave gauge calibration of 0.4 mm (error

	Input		Estimated						
	σ_θ (deg.)	a_0 (m)	$\sigma^\star_\theta$ (deg.)				$\frac{a^{(2)}_{T-}}{k_0 a_0^2}$		
Test:			all probes	span-wise	mean	Δ	$\sigma^\star_\theta - 2\Delta\sigma^\star_\theta$	$\sigma^\star_\theta + 2\Delta\sigma^\star_\theta$	Error
A.1	0	0.1	0	0	0	0	-	-	-
A.2	10		8.8	8.8	8.9	0.78	-0.1048	-0.0934	-0.0114
A.3	20		16.4	16.5	16.4	0.59	-0.0710	-0.0622	-0.0088
A.4	30		28.2	28.5	28.2	0.46	-0.0195	-0.0126	-0.0070
A.5	40		37.9	38.6	37.9	0.39	0.0182	0.0239	-0.0057
A.6	50		47.5	48.7	47.5	0.38	0.0551	0.0599	-0.0048
A.7	60		57.0	58.9	57.1	0.35	0.0838	0.0877	-0.0039
A.8	70		66.6	70.1	66.7	0.40	0.1077	0.1111	-0.0034
A.9	80		76.4	84.4	76.4	0.49	0.1263	0.1293	-0.0030
A.10	90		85.9	124.5	86.0	0.59	0.1388	0.1413	-0.0025
A.11	135		130.3	122.7	130.3	0.55	0.1693	0.1697	-0.0005
A.12	180		178.1	122.8	178.0	1.8	0.1717	0.1720	-0.0004
A.13	360		360	126.0	360	-	0.1733	0.1734	-0.0001
A.14	0	0.15	0	0	0	0	-	-	0
A.15	10		7.8	6.6	8.2	1.55	-0.1189	-0.0954	-0.0234
A.16	20		15.7	15.0	15.8	0.71	-0.0830	-0.0716	-0.0113
A.17	30		28.0	27.6	28.0	0.47	-0.2037	-0.0159	-0.0077
A.18	40		38.0	38.2	38.0	0.32	0.0190	0.0240	-0.0050
A.19	50		47.6	48.5	47.7	0.27	0.0580	0.0616	-0.0035

Table 3.4. Propagation of error in spreading estimation for spreading tests (category A)

	Input			Estimated						
	$\Delta\theta$ (deg.)	σ_θ (deg.)	a_0 (m)	$\sigma_\theta^\star$ (deg.)				$\frac{a_{T^-}^{(2)}}{k_0 a_0^2}$		
Test:				all probes	span-wise	mean	Δ	$\sigma_\theta^\star - 2\Delta\sigma_\theta^\star$	$\sigma_\theta^\star + 2\Delta\sigma_\theta^\star$	Error
C.1	45	10	0.1	9.5	9.5	9.4	0.47	-0.0292	-0.0260	-0.0051
C.2	90			9.3	10.2	9.3	0.59	0.0550	0.0533	-0.0072
C.3	135			9.7	11.2	9.7	0.79	0.1262	0.1210	-0.0121
C.4	180			8.8	9.1	8.5	1.26	0.1510	0.1521	-0.0087
C.5	45	20	0.1	18.4	17.9	18.5	0.56	-0.0111	-0.0060	-0.0051
C.6	90			18.6	19.3	18.7	0.37	0.0677	0.0642	-0.0079
C.7	135			18.5	18.9	18.5	0.35	0.1328	0.1245	-0.0109
C.8	180			18.7	19.0	18.6	0.46	0.1580	0.1483	-0.0172
C.9	45	30	0.1	27.5	27.5	27.5	0.45	0.0126	0.0168	-0.0055
C.10	90			28.3	29.4	28.3	0.60	0.0773	0.0734	-0.0109
C.11	135			28.2	29.3	28.3	0.40	0.1387	0.1289	-0.0121
C.12	180			28.0	28.5	28.0	0.35	0.1669	0.1496	-0.0185
C.13	45	20	0.15	17.7	17.5	17.9	0.74	-0.0129	-0.0104	-0.0113
C.14	90			18.6	19.2	18.6	0.41	0.0678	0.0658	-0.0071
C.15	135			19.1	21.3	19.2	0.72	0.1347	0.1283	-0.0116
C.16	180			18.6	18.9	18.5	0.53	0.1684	0.1564	-0.0148

Table 3.5. Propagation of error in spreading estimation for crossing tests (category C)

measure V). As these measures of error are not independent, the calibration error is taken to be the dominant source of error and this was used the error bars presented in the next section. These error bars constitute a large relative error ($\approx 100\%$) when the amplitude of wave-averaged surface elevation approaches zero $\sigma_\theta = 30 - 40°$, this is unavoidable when measuring a transition from set-up (-ve) to set-down (+ve). At such values relative error is misleading, and it is more important that measurements lie within error bounds of theoretical predictions.

Chapter 4

Directionally spread focused wave groups

For a single directionally spread focused wave group, increasing the degree of directional spreading reduces the in line velocity of the wave crest, spreading the energy of the group in multiple directions. This reduces the effects of Stokes transport, hence the return flow and resulting 'set-down'. As the degree of spreading is increased further $30 - 40°$, this 'set-down' of the wave-averaged surface elevation can become positive, forming a 'set-up'. This set-up behaves differently to the set-down and forms under differing physical mechanisms. By conducting tests where the spreading of waves is varied between unidirectional and axisymmetric, this transition is captured experimentally for the first time. Tests are then carried out to capture the spatial structure of both phenomena and the transition between the two as spreading increases. New insight is gained, of the formation of the set-up showing it to behave as a partial standing wave that does not translate with the wave group like the classically understood slow behaviour of the set-down.

4.1 A - Spreading tests

4.1.1 Measured free surface elevation time series

Figures 4.1 and 4.2 present the free surface elevation time series measured at the central probe for tests A.1-A.12 and increased amplitude tests A14-A19. In general the experiments exhibit good focusing with maxima occurring at $t = 0$ and display horizontal symmetry. However, for the long-crested increased amplitude waves the focusing at $x = 0$ $y = 0$ is clearly reduced and the groups exhibit horizontal asymmetry (figure 4.2a and b). Here, the dispersion of free waves is being affected by cubic nonlinearity, as observed by Taklo et al. [2017]. As discussed in §3.3.3, this will not affect extraction of the measured wave-averaged surface elevation, but it should be noted when drawing comparison to theory based on perfect linear focusing.

4.1.2 Estimated spectral parameters

Table 4.1 details the estimated spectral parameters for the spreading tests. The estimated spreading $\sigma_\theta^\star$ is consistent with input values of spreading, a slight offset is observed with the estimates consistently smaller than the inputs. The increased amplitude tests A.14-19 show a larger reduction in spreading for tests at $\sigma_\theta^\star = 10°$ and $\sigma_\theta^\star = 20°$. This is consistent with the numerical simulations of Gibbs and Taylor [2005], who observe a reduction in spreading proportional to steepness α^2 for a degree of spreading $\sigma_\theta = 15°$. There is a slight reduction in carrier wavenumber for tests at $0 - 20°$. This is consistent with Lake et al. [1977] and Tian et al. [2011] who observe a down shift of peak wavenumber that becomes more pronounced with steepness. Here, this occurs for the long-crested waves, as the effect of spreading serves to decrease the overall degree of nonlinearity as

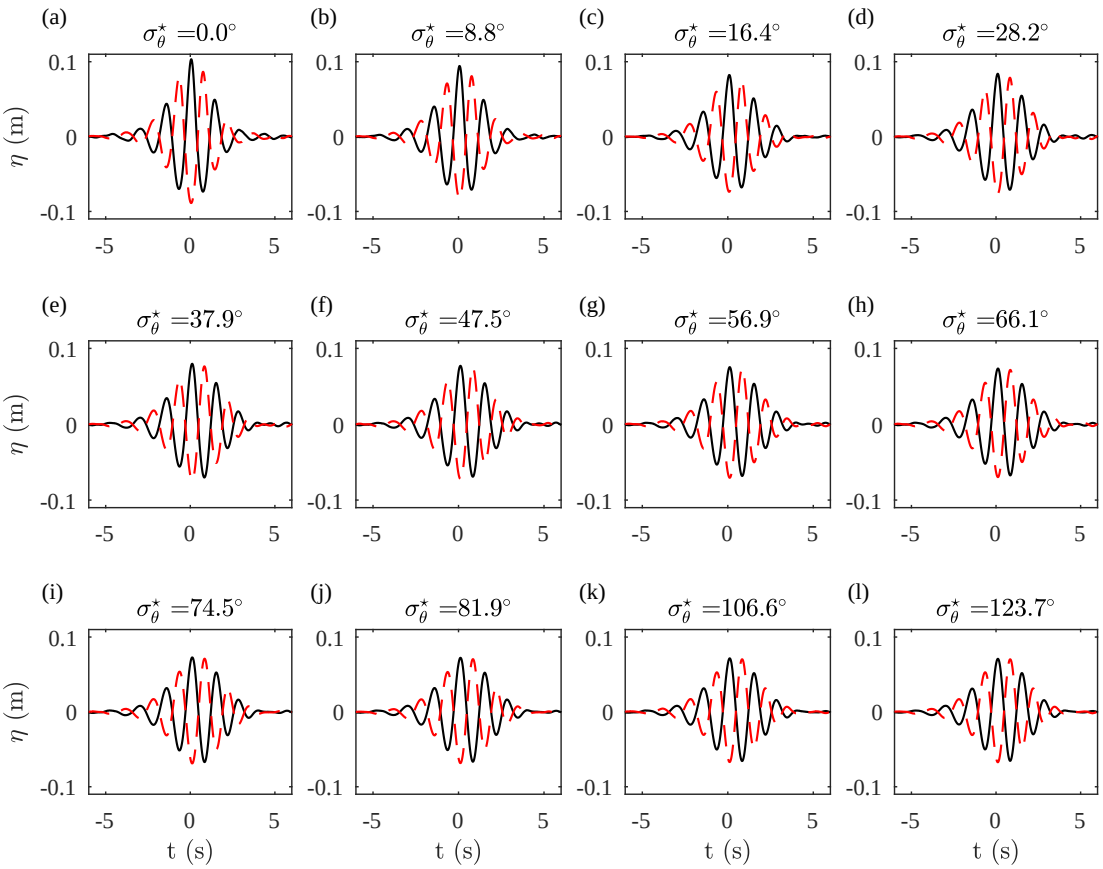

Figure 4.1. Measured time series η at the central probe ($x = 0$, $y = 0$) for the spreading tests (category A), showing crest-focused group η_0 (black lines) and trough-focused group η_{180} (red dashed lines) for input amplitude $a_0 = 0.1$ m. The different panels correspond to increasing degrees of input spreading $\sigma_\theta = 0 - 180°$, and the captions denote the estimated degree of spreading $\sigma_\theta^\star$.

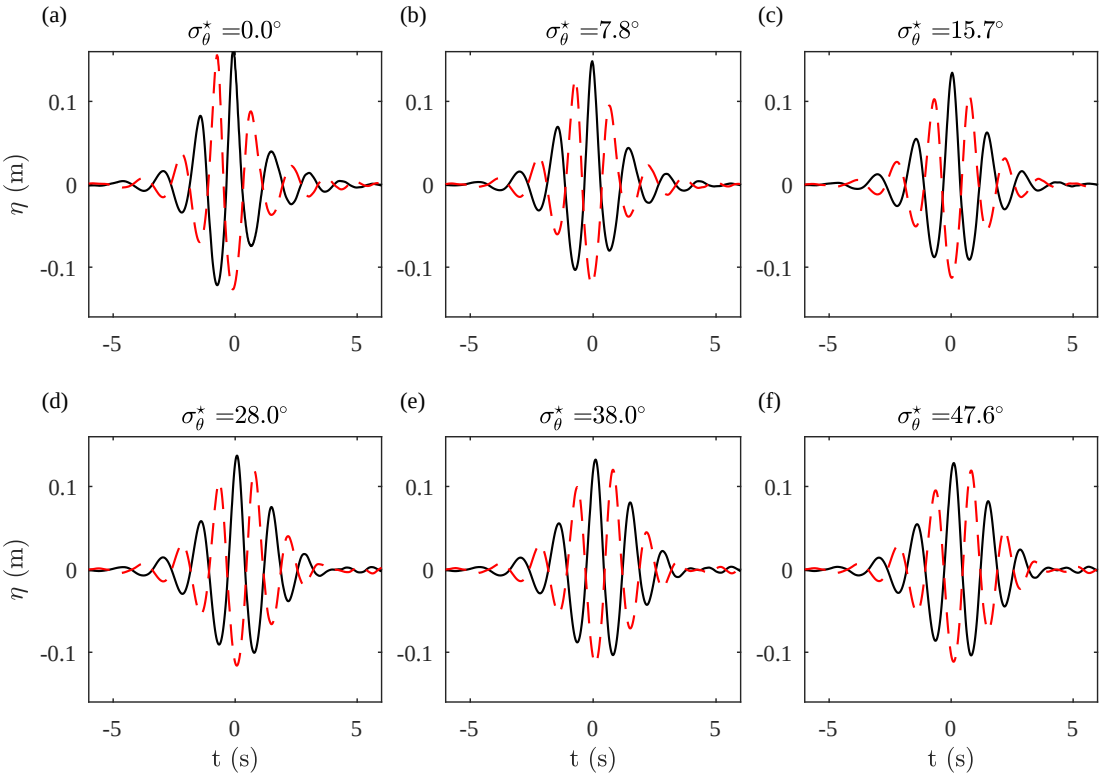

Figure 4.2. Measured time series η at the central probe ($x = 0$, $y = 0$) for the spreading tests (category A), showing crest-focused group η_0 (black lines) and trough-focused group η_{180} (red dashed lines) for input amplitude $a_0 = 0.15$ m. The different panels correspond to increasing degrees of input spreading $\sigma_\theta = 0 - 50°$, and the captions denote the estimated degree of spreading $\sigma_\theta^\star$.

	Input				Estimated			
Test:	σ_θ (deg.)	a_0 (m)	k_0 (m^{-1})	Δk (m^{-1})	$\sigma_\theta^\star$ (deg.)	$a_0^\star$ (m)	$k_0^\star$ (m^{-1})	$\Delta k^\star$ (m^{-1})
A.1	0	0.1	1.97	0.6	0	0.094	1.90	0.56
A.2	10				8.8	0.090	1.74	0.61
A.3†	20				16.4	0.082	1.74	0.64
A.4†	30				28.2	0.085	1.90	0.61
A.5†	40				37.9	0.083	1.90	0.62
A.6	50				47.5	0.081	1.90	0.63
A.7	60				57.0	0.080	1.90	0.64
A.8	70				66.6	0.079	1.90	0.64
A.9	80				76.4	0.078	1.90	0.64
A.10	90				85.9	0.077	1.90	0.65
A.11	135				130.3	0.075	1.90	0.58
A.12	180				178.1	0.076	1.90	0.63
A.13†	360				412	0.076	1.90	0.63
A.14	0	0.15	1.97	0.6	0	0.157	1.74	0.71
A.15	10				7.8	0.138	1.74	0.66
A.16	20				15.7	0.123	1.74	0.65
A.17	30				28.0	0.127	1.90	0.60
A.18	40				38.0	0.127	1.90	0.61
A.19	50				47.6	0.126	1.90	0.60

Table 4.1. Input and estimated spectral parameters for the spreading tests (category A), † denotes tests which were repeated with additional 90° and 270° phase shifts.

discussed by Johannessen and Swan [2001]. There are no significant trends in the estimated bandwidth $\Delta k^\star$. The amplitude $a_0^\star$ of the measured waves reduces as the degree of spreading is increased. As with the other estimated parameters the increased nonlinearity at low degrees of spreading affects the measured amplitude causing it to increase; this is most clear in test A.14 where $a_0^\star$ is greater than the input amplitude. However, nonlinearity does not affect the highly spread tests in the same way, and is presumably not the reason for the decrease in amplitude which is thought to be a result of systematic under-production of amplitude in the tank.

4.1.3 Wave-averaged surface elevation

Figure 4.3 plots measured the wave-averaged surface elevation $\eta^{(2)}_{M-}$ at the central probe for tests A.1-12, shown alongside theoretically predicted wave-averaged surface elevation $\eta^{(2)}_{T-}$. The subscripts M and T denote measured and theoretically predicted surface elevations respectively. $\eta^{(2)}_{M-}$ is extracted from the measurements using the process outlined in §3.3.3, and $\eta^{(2)}_{T-}$ is calculated using (3.3), the values of $\sigma_\theta^\star$ in table 4.1, and the linear time series $\eta^{(1)}_M$ measured at the central probe. Both the measured and predicted results initially show a set-down in the wave-average surface elevation (panels a-d). As the degree of spreading is increased, the amplitude of the set-down decreases and reaches zero at around $\sigma_\theta^\star \approx 40^\circ$ (panel e), after which a set-up begins to form (panels f-l). The measured and predicted wave-averaged surface elevation show very good agreement, the level of agreement is greatest at the extremes in spreading. As $\sigma_\theta \to 0$ it is straightforward to estimate accurately spreading. As $\sigma_\theta \to 360$ the directional spectrum begins to saturate with waves travelling in all directions, accordingly changes in the amplitude of $\eta^{(2)}$ in this region are small. Therefore, as measured $\eta^{(2)}_{M-}$ is well predicted by $\eta^{(2)}_{T-}$ at these limits where uncertainty in $\sigma_\theta^\star$ is low, the slight decrease in agreement

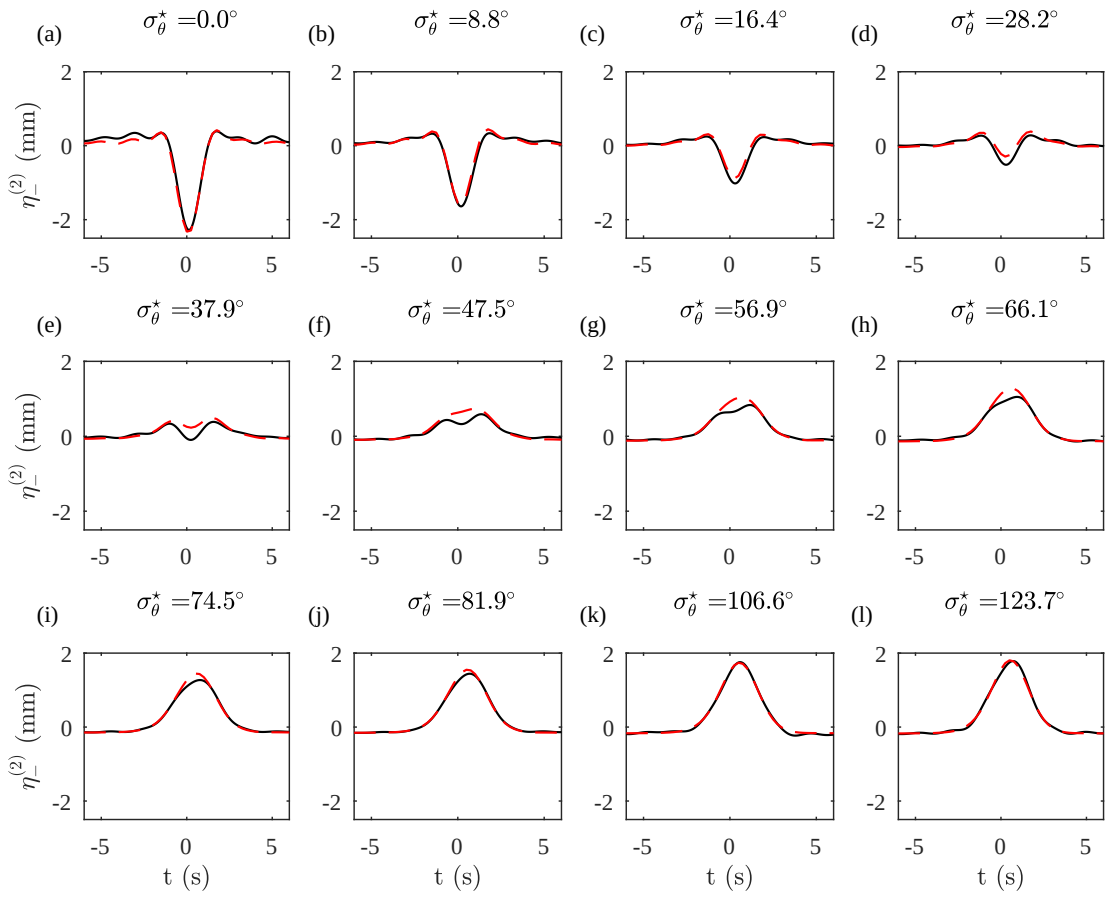

Figure 4.3. Wave-averaged surface elevation $\eta_-^{(2)}$ at the central probe ($x = 0$, $y = 0$) for the spreading tests (category A), showing measured waves $\eta_{M-}^{(2)}$ (black lines) and theoretical predictions $\eta_{T-}^{(2)}$ (red dashed lines) for input amplitude $a_0 = 0.1$ m. The different panels correspond to increasing degrees of input spreading $\sigma_\theta = 0-180°$, and the captions denote the estimated degree of spreading $\sigma_\theta^\star$ used for the theoretical predictions of $\eta_{T-}^{(2)}$.

for intermediate values of $\sigma_\theta^\star$ may be indicative of error in the estimation of $\sigma_\theta^\star$. It is also the case that amplitude of the wave-averaged surface elevation for these values is very small, therefore more susceptible to sources of error (see §3.3.6).

Figure 4.4 shows the wave-averaged surface elevation time series of tests A.14-19 that were repeated for increased amplitude $a_0 = 0.15$ m. These tests range from input spreading $\sigma_\theta = 0 - 50°$, and also show the sign change in wave-averaged surface elevation. For these tests the agreement between $\eta_{M-}^{(2)}$ and

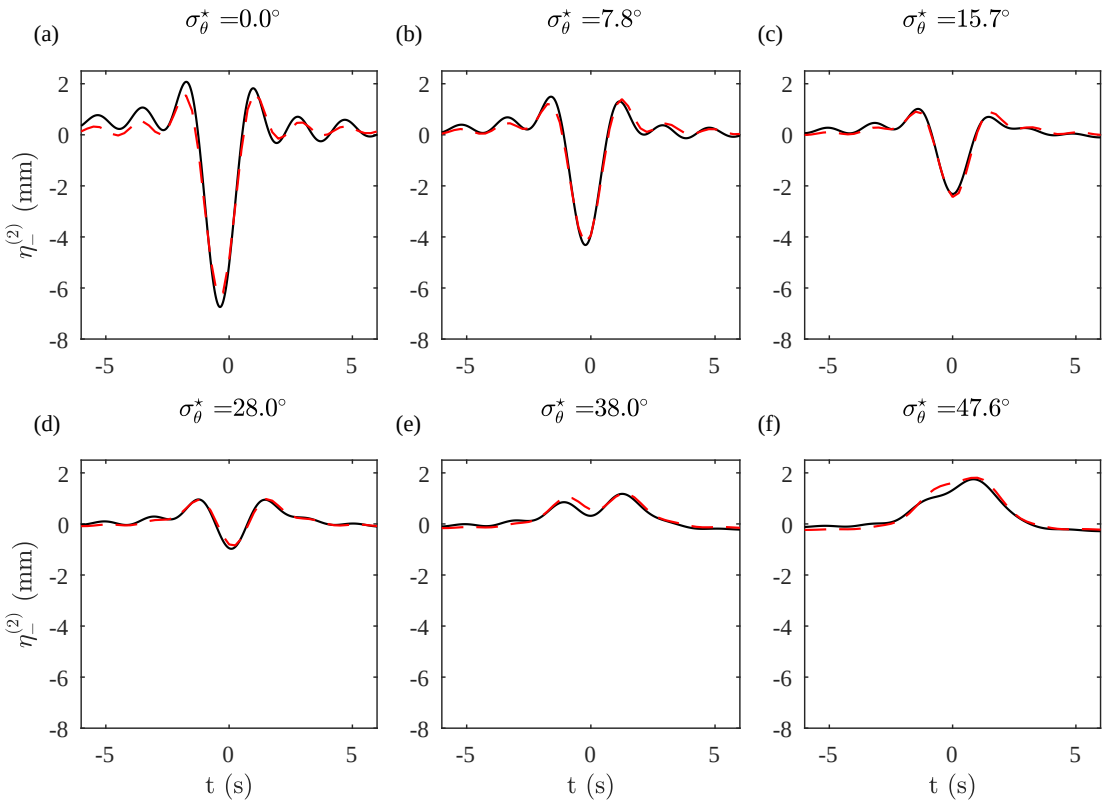

Figure 4.4. Wave-averaged surface elevation $\eta_-^{(2)}$ at the central probe ($x = 0$, $y = 0$) for the spreading tests (category A), showing measured waves $\eta_{M-}^{(2)}$ (black lines) and theoretical predictions $\eta_{T-}^{(2)}$ (red dashed lines) for linear input amplitude $a_0 = 0.15$ m. The different panels correspond to increasing degrees of input spreading $\sigma_\theta = 0-50°$, and the captions denote the estimated degree of spreading $\sigma_\theta^\star$.

$\eta_{T-}^{(2)}$, is also excellent, and does not reduce significantly with spreading. This reinforces the notion that the slight decrease in agreement observed in figure 4.3, for intermediate spreading values, may be a result of measurement uncertainty.

Figure 4.5 summarises the results of the spreading tests. In panel b the amplitude of the measured $a_{M-}^{(2)}$ wave-averaged surface elevation is plotted as a function of the estimated degree of directional spreading $\sigma_\theta^\star$. Here, the amplitude $a_{M-}^{(2)}$ is non-dimensionalised by $(k_0 a_0^2)$, both tests at $a_0 = 0.1$ and $a_0 = 0.15$ m compare well and are effectively scaled by $(k_0 a_0^2)$. The red lines show the amplitude of the wave-averaged surface elevation for a Gaussian wave group $k_0 = 1.90$ m^{-1} and

$\Delta k = 0.65$ m^{-1}, the dotted line shows the narrow-banded ($\epsilon_x \to 0$) separation-of-scales approximation. The two approaches to calculating the value of $a_-^{(2)}$ agree under unidirectional conditions. As σ_θ increases the two values diverge significantly, and the narrow-banded approximation always remains negative. It should be noted that values of $k_0^\star$ and $\Delta k^\star$ vary between tests. In light of this, the experimental values $a_{M-}^{(2)}$ compare very well with the theoretical predictions for a perfectly focused Gaussian wave group. Panel a compares the amplitude of measured wave-averaged surface elevation $a_{M-}^{(2)}$ to $a_{T-}^{(2)}$ calculated using equation 3.3. This comparison accounts for actual measured spectra, and as noted for figures 4.3 and 4.4, the increased amplitude experiments compare slightly better to theory. However, both sets of test compare very well overall. Both sets of results compare best at the extremes of spreading; it is at these points that the confidence in the degree of spreading is highest for the near unidirectional cases, and has little influence for the highly spread tests. These values of $a_-^{(2)}$ are also the largest in magnitude. Therefore, the most likely causes of the small reduction in agreement are the estimation of spreading or the influence of background noise (see §3.3.6).

4.1.4 Sum waves

As well as the wave-averaged surface elevation, the second-order super harmonics $\eta_+^{(2)}$ may be examined. Time series of measured and predicted $\eta_+^{(2)}$ are presented in Appendix B; upon visual comparison these predictions and measurements compare remarkably well too. Figure 4.6 panel b, presents the amplitude $\eta_+^{(2)}$ of sum waves to those expected for a Gaussian wave packet, as a function of spreading. Here, $\eta_+^{(2)}$ is calculated using the wave envelope, given that the sum waves are composed of high frequency waves the location of the maxima is more sensitive to phase. At low values of spreading the sum waves are larger

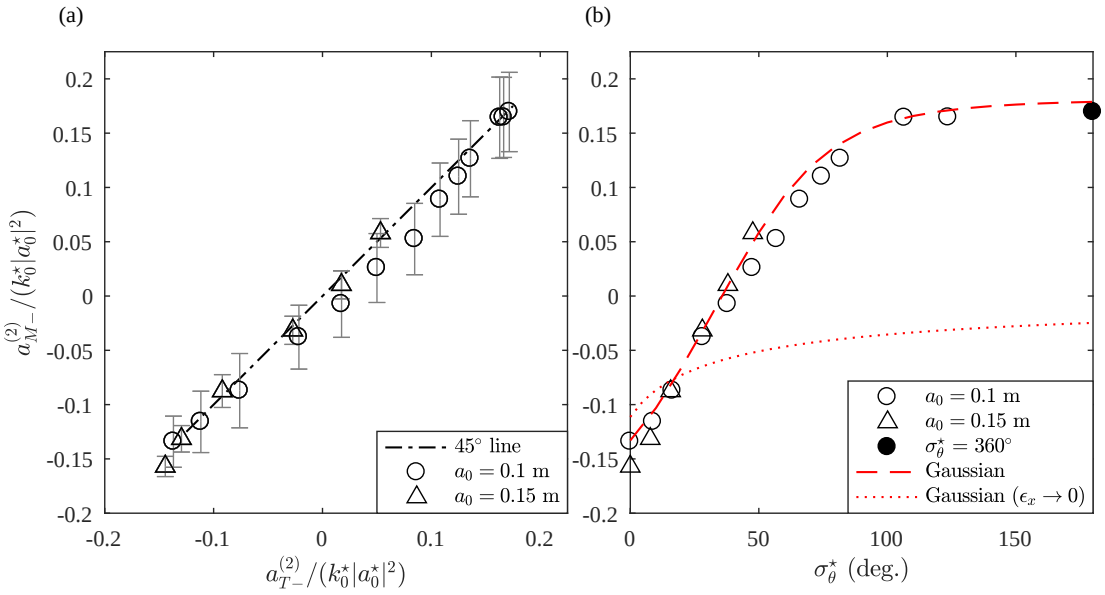

Figure 4.5. Amplitude of wave-averaged surface elevation at the central probe ($x = 0$, $y = 0$) for the spreading tests (category A). Panel a shows the measured mean free surface amplitude $a^{(2)}_{M-}$ as a function of the theoretical prediction $a^{(2)}_{T-}$, and panel b shows the measured mean free surface amplitude $a^{(2)}_{M-}$ as a function of the estimated degree of spreading $\sigma^\star_\theta$.

than expected for a Gaussian wave packet; this is thought to be the results of unabsorbed noise or non Guassian spectral tail.

4.2 B - Surface tests

4.2.1 Estimated spectral parameters

The estimated spectral parameters for the surface tests are presented in table 4.2, the spectral parameters for tests B.1-4 are consistent with tests A.3-4,18. As θ_0 is varied through 90°, $\sigma^\star_\theta$ varies at most by 1.2°, the values of $\sigma^\star_\theta$ for the increased amplitude surface test are more precise varying only by 0.4°. Variation in Δk for the surface tests is similar to that observed for the spreading tests (category A),

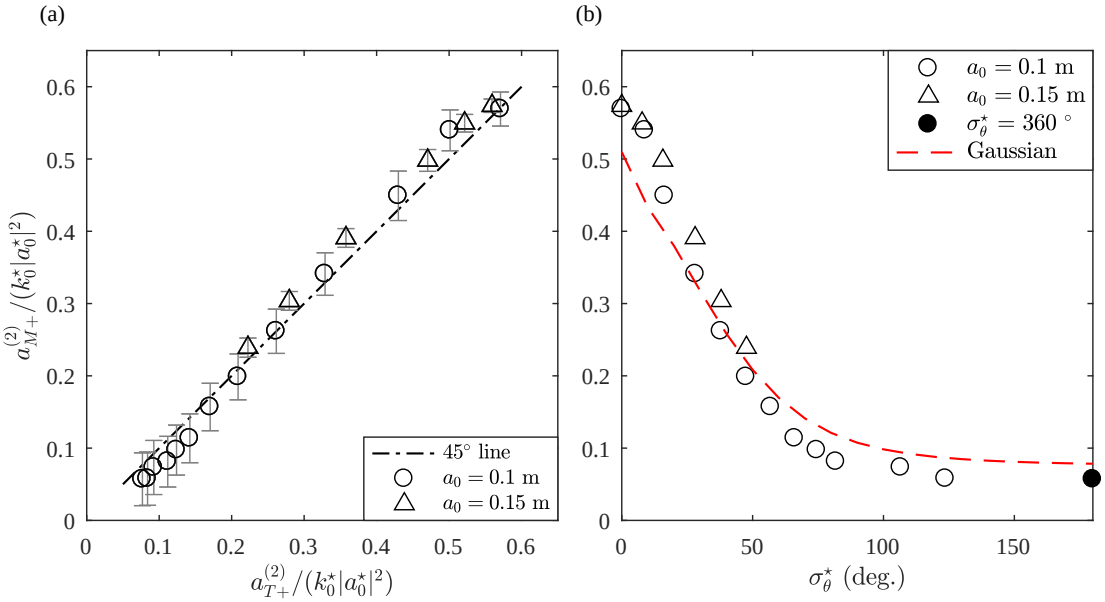

Figure 4.6. Amplitude of second-order sum waves at the central probe ($x = 0$, $y = 0$) for the spreading tests (category A). Panel a shows the measured mean free surface amplitude $a_{M+}^{(2)}$ as a function of the theoretical prediction $a_{T+}^{(2)}$, and panel b shows the measured mean free surface amplitude $a_{M+}^{(2)}$ as a function of the estimated degree of spreading $\sigma_\theta^\star$.

reinforcing the notion that this is not a phenomenon associated with the foregoing experiments.

4.2.2 Linear surface

The process behind the estimation of $\sigma_\theta^\star$ is visualised by figure 4.7, where the measured linear free surface $\eta_M^{(1)}$ (panels a-c) and the predicted linear surface $\eta_T^{(1)}$ (panels e-h) are shown as contour plots at time of focus. For all for tests B.1-4, the predicted linear free surface contours compare very well to measurement. At the front of the wave groups a small amount of discrepancy is observed for all four tests, where the measured waves are very slightly steeper. A contraction at the front of the wave group supplementary to the effects of linear dispersion is discussed by Gibbs and Taylor [2005].

	Input					Estimated			
Test:	θ_0 (deg.)	σ_θ (deg.)	a_0 (m)	k_0 (m^{-1})	Δk (m^{-1})	$\sigma_\theta^\star$ (deg.)	$a_0^\star$ (m)	$k_0^\star$ (m^{-1})	$\Delta k^\star$ (m^{-1})
B.1.1	0	20	0.1	1.97	0.6	16.4	0.083	1.74	0.63
B.1.2	22.5					15.8	0.082	1.74	0.63
B.1.3	45					16.2	0.082	1.74	0.61
B.1.4	67.5					16.8	0.082	1.74	0.58
B.1.5	90					17.0	0.083	1.74	0.62
B.2.1	0	30	0.1	1.97	0.6	27.7	0.085	1.90	0.62
B.2.2	22.5					27.8	0.084	1.90	0.59
B.2.3	45					28.5	0.084	1.90	0.57
B.2.4	67.5					28.6	0.086	1.90	0.58
B.2.5	90					28.6	0.085	1.90	0.57
B.3.1	0	40	0.1	1.97	0.6	37.6	0.083	1.90	0.61
B.3.2	22.5					37.4	0.082	1.90	0.59
B.3.3	45					38.6	0.083	1.90	0.59
B.3.4	67.5					38.5	0.084	1.90	0.58
B.3.5	90					38.3	0.084	1.90	0.59
B.4.1	0	40	0.15	1.97	0.6	37.9	0.127	1.90	0.61
B.4.2	22.5					38.0	0.128	1.90	0.60
B.4.3	45					38.2	0.129	1.90	0.59
B.4.4	67.5					38.0	0.128	1.90	0.58
B.4.5	90					38.3	0.128	1.90	0.58

Table 4.2. Input and estimated spectral parameters for the surface tests (category B).

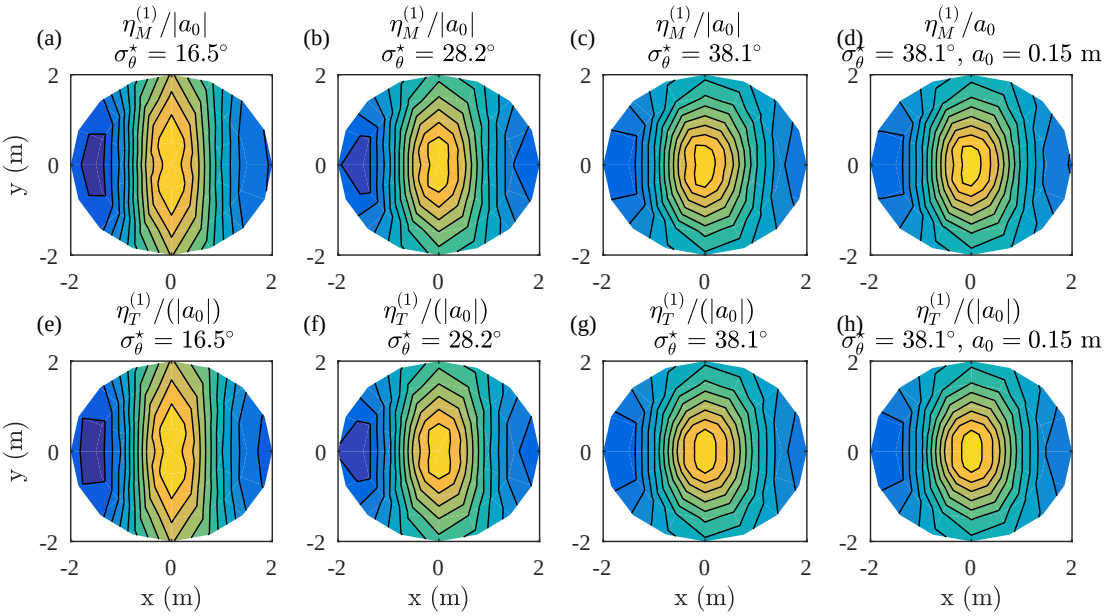

Figure 4.7. Contour plots showing the measured linear free surface elevation $\eta_M^{(1)}$ (panels a-d) and the predicted linear surface elevation $\eta_T^{(1)}$ (panels e-h) at time of focus for the surface tests (catagory B). The different panels correspond to increasing degrees of input spreading $\sigma_\theta = 20, 30, 40°$, and the captions denote the estimated degree of spreading $\sigma_\theta^\star$ used for theoretical predictions of $\eta_T^{(1)}$.

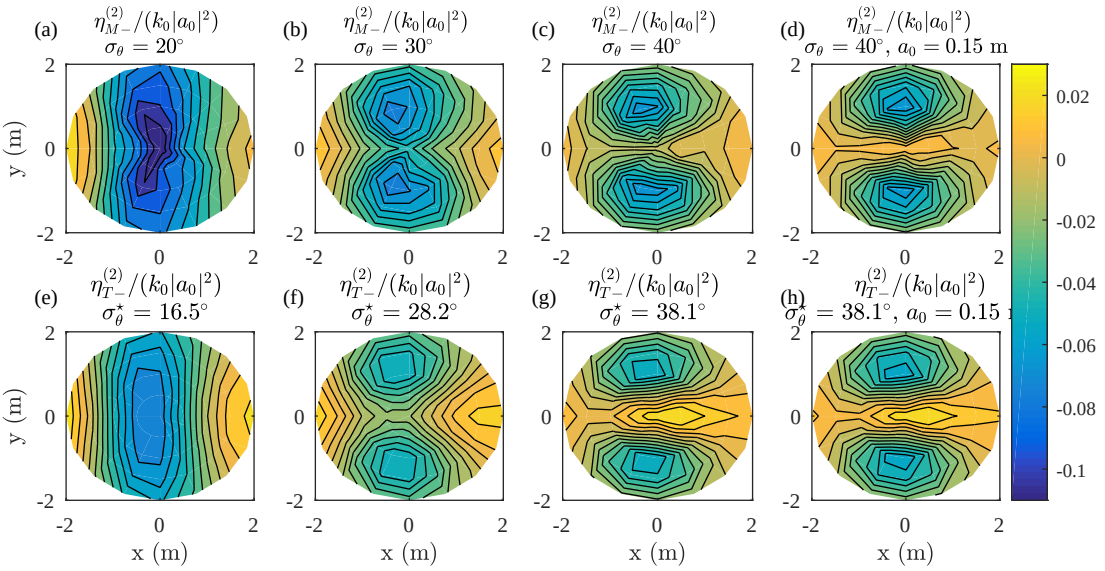

Figure 4.8. Contour plots showing the measured wave-averaged surface elevation $\eta_{M-}^{(2)}$ (panels a-c) and the predicted wave-averaged surface elevation $\eta_{T-}^{(2)}$ (panels e-f) at time of focus. The different panels correspond to increasing degrees of input spreading $\sigma_\theta = 20, 30, 40°$, and the captions denote the estimated degree of spreading $\sigma_\theta^\star$ used for theoretical predictions of $\eta_{T-}^{(2)}$.

4.2.3 Wave-averaged surface elevation

The two dimensional structure wave-averaged surface elevation is examined in figure 4.8. The top row of panels (a) to (d) show the measured wave-averaged surface elevation $\eta^{(2)}_{M-}$ as input spreading is increased from $20 - 40°$. For these panels the measured surface $\eta^{(2)}_{M-}$ in the south west quadrant ($x < 0$, $y < 0$) is mirrored from the north-west quadrant ($x < 0$, $y > 0$) to complete the surface. The bottom row of panels (e) to (h) show the wave-averaged surface elevation $\eta^{(2)}_{M-}$, calculated for $\sigma^{\star}_{\theta}$. Here, the set-down can initially be observed as a deep hole that is gradually reduced by the formation of the set up, eventually splitting into two holes either side of the wave crest. For each test the holes are slightly deeper than predicted and the set-up is less pronounced. This suggests that the, degree of directional spreading at focus may be lower than $\sigma^{\star}_{\theta}$. This is a nonlinear effect observed by Gibbs and Taylor [2005], however, this is not expected at values of $\sigma^{\star}_{\theta}$ as large as 40°. It is worth noting that the array of probes used to generate these contour plots is sparse around the point of focus ($x = 0$,$y = 0$)(see figure 3.6). Therefore, any error in this area is exaggerated when linear interpolation is used to produce the contour surfaces. In light of this qualitative comparison between the experiment and theory is still very good, and the formation of the set up ridge is clearly captured.

Test B.3 was repeated at an increased amplitude of $a_0 = 0.15$ m (test B.4). First, the linear free surface is compared (figures 4.7c and d), $\eta^{(1)}_{M}$ is nondimensionalised by $(k_0 a_0)$. At cursory inspection the scaled linear free surfaces are indistinguishable. Second, the wave-averaged surface elevation is compared (figures 4.8c and d). Here, the wave-averaged surface elevation for both test has a similar form with two holes either side of the set-up. Both sets of holes have the same magnitude whereas the set up observed for the increased amplitude test (panel d) is

much more pronounced. The majority of this discrepancy stems from the one measurement at the central probe.

Figure 4.9 shows the evolution of the wave-averaged surface elevation in time moving left to right and increasing $\sigma_\theta^\star$ top to bottom, this figure clearly illustrates the formation of the set-up ridge as spreading is increased. The temporal evolution of the surface moving left to right shows how the set-down associated with the group propagates towards the point of focus, where it is counteracted by the set-up that forms a ridge along the direction of propagation. Here, it is clear that the set-up acts like a partial standing wave forming at the focal point if the wave group, and does not propagate in space like the set-down.

4.3 Conclusions

Herein, detailed experiments of the wave-averaged surface elevation for compact directionally spread waves on deep water ($k_0 d \gg 1$) are presented. Experimental observations are compared to second-order theory using existing Fourier-base spectral summation. Excellent agreement is observed with predictions made using the approach of Dalzell [1999].

The existence of a set-up for highly directionally spread groups is experimentally confirmed for the first time. The 2D structure of this phenomenon is explored, showing the set-up to be a fundamentally different standing wave effect fixed in space, to a set-down which is a slow process that travels with the wave group.

These tests provide excellent insight to the existence of a set-up for highly spread focused wave groups, and importantly its temporal and spatial behaviour. However, such wave groups do not present a realistic scenario for the formation of a set-up in observations of real sea waves in extra-tropical storms.

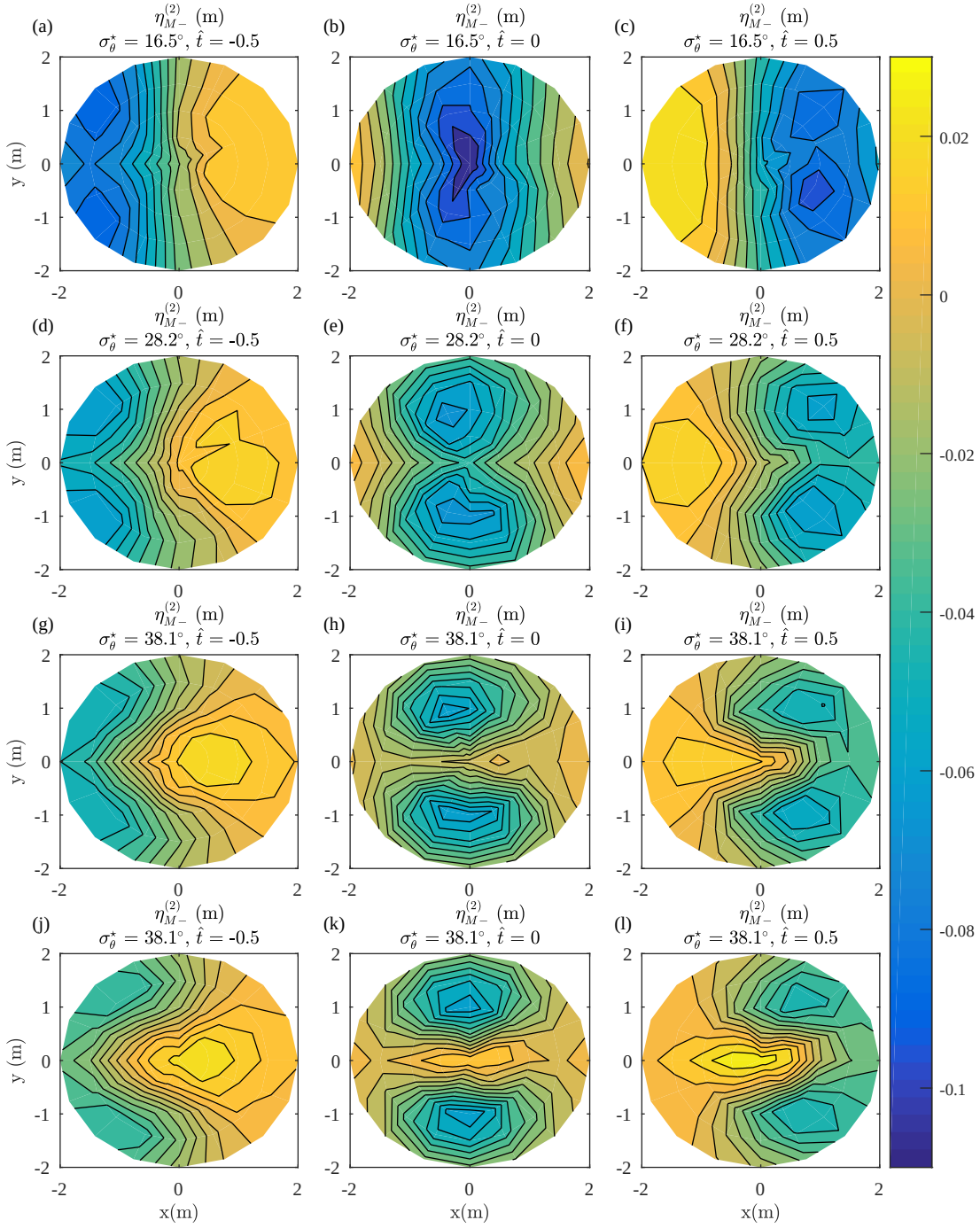

Figure 4.9. Contour plots showing evolution the measured wave-averaged surface elevation $\eta^{(2)}_{M-}$ in time (left to right); before focus ($\hat{t} = -0.5$) (panels a,d,g,j), at focus ($\hat{t} = 0$) (panels b,c,h,k) and after focus ($\hat{t} = 0.5$) (panels c,f,i,l); for increasing degrees of input spreading $\sigma_\theta = 20, 30, 40°$. The captions denote the estimated degree of spreading $\sigma^\star_\theta$.

Chapter 5

Directionally spread crossing wave groups

Encountering wave groups with near axisymmetric spreading is very unlikely in the ocean, and hence most often waves measured in extra tropical storms display a set-down in wave-averaged surface elevation. However, in a number of prominent examples [Fedele et al., 2016] of very large or Freak waves, a set-up in wave-averaged surface elevation is observed. In such cases the crossing of wave groups that results from separated wind and swell systems may be the cause. Tests are carried out to assess the formation of a set-up for directionally spread crossing wave groups. For crossing angles of 50-70°, and beyond, a pronounced set-up is observed. The wave-averaged surface elevation of crossing groups is shown to differ drastically from a single group, showing fast spatial variation on a similar scale to the linear waves. Despite occurring at the confluence of two wave groups, the spatial structure of the wave-averaged surface elevation is also less localised in space than the narrow set-up ridge observed for a single group.

5.1 C - Crossing Tests

5.1.1 Measured time series

The time series measured at the central probe for tests A.1-A.12 and increased amplitude tests A.14-A.19 are presented in figure 5.1. In general the experiments exhibit good focusing with maxima occurring at $t = 0$ and display horizontal symmetry. Here, both tests with $a_0 = 0.1$ m and $a_0 = 0.15$ m exhibit similar focusing unlike the spreading tests at increased amplitude and low degrees of spreading in Chapter 4. It should be noted that the two crossing groups have individual amplitudes of $a_0/2$ and so they are initially less steep.

5.1.2 Estimated spectral parameters

Estimated spectral parameters for the crossing tests are presented in table 5.1. Comparison with the results of tests from categories A and B, is less straightforward here. The estimated degree of directional spreading is consistently higher than estimates for the foregoing tests with the same input. This may be owing to the fact that the initial steepness of the groups is half that of the previous test. Therefore, if the reduction in spreading is a result of nonlinearity these tests are less affected.

5.1.3 Wave-averaged surface elevation

Figure 5.2 plots the wave-averaged surface elevation $\eta^{(2)}_{M-}$ measured at the central probe for tests C.1-16, shown with $\eta^{(2)}_{T-}$ the theoretically predicted wave-averaged surface elevation. The panels correspond to increasing the crossing angle $\Delta\theta$

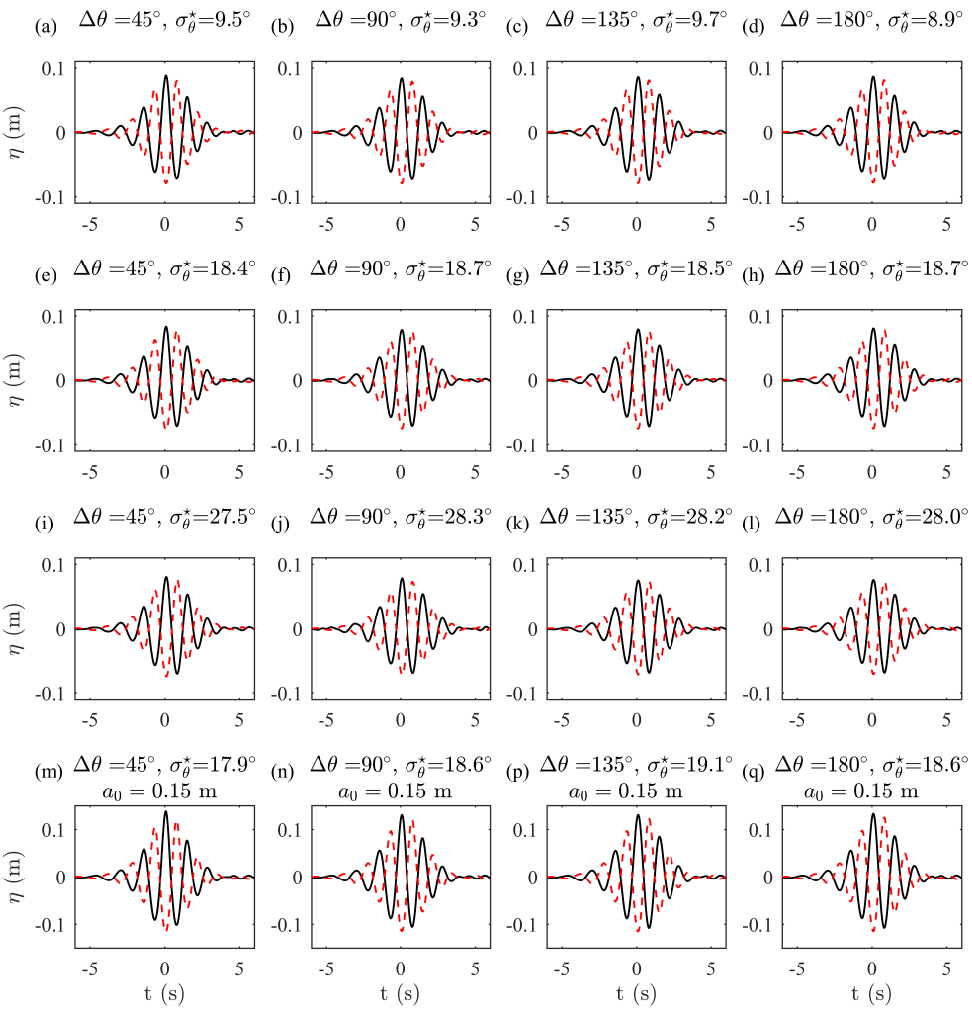

Figure 5.1. Measured time series η at the central probe ($x = 0$, $y = 0$) for the crossing tests (category C), showing crest-focused group η_0 (black lines) and trough-focused group η_{180} (red dashed lines) for input amplitude $a_0 = 0.1$ m. The different panels correspond to increasing values of crossing angle $\Delta\theta = 0-180°$ for degrees of input spreading $\sigma_\theta = 10, 20, 30°$, and the captions denote the estimated degree of spreading $\sigma^\star_\theta$.

	Input					Estimated			
Test:	$\Delta\theta$ (deg.)	σ_θ (deg.)	a_0 (m)	k_0 (m^{-1})	Δk (m^{-1})	$\sigma_\theta^\star$ (deg.)	$a_0^\star$ (m)	$k_0^\star$ (m^{-1})	$\Delta k^\star$ (m^{-1})
C.1	45	10	0.1	1.97	0.6	9.5	0.086	1.90	0.57
C.2	90					9.3	0.086	1.90	0.54
C.3	135					9.7	0.088	1.90	0.58
C.4	180					8.8	0.087	1.90	0.55
C.5	45	20	0.1	1.97	0.6	18.4	0.084	1.90	0.60
C.6	90					18.6	0.082	1.90	0.59
C.7	135					18.5	0.083	1.90	0.58
C.8	180					18.7	0.084	1.90	0.59
C.9	45	30	0.1	1.97	0.6	27.5	0.083	1.90	0.60
C.10	90					28.3	0.083	1.90	0.97
C.11	135					28.2	0.080	1.90	0.61
C.12	180					28.0	0.080	1.90	0.60
C.13	45	20	0.15	1.97	0.6	17.7	0.129	1.96	0.61
C.14	90					18.6	0.127	1.95	0.61
C.15	135					19.1	0.131	1.95	0.61
C.16	180					18.6	0.130	1.88	0.57

Table 5.1. Input and estimated spectral parameters for the crossings tests (category C).

moving left to right, and the degree of spreading top to bottom. The bottom row (panels m-p) shows the increased amplitude crossing tests C.13-16. For all degrees of spreading tested, initially at $\Delta\theta = 45°$ a small set -down is observed. When the crossing angle is increased to 90° all degrees of spreading display a significant set-up, which grows to a maximum value at $\Delta\theta = 180°$. The measured and predicted wave-averaged surface elevation results again show remarkable agreement, the level of agreement is slightly reduced at small crossing angles.

Figure 5.3 summarises the results of the crossing tests. In panel (a) the amplitude of the measured $a_{M-}^{(2)}$ wave-averaged surface elevation is plotted as a function of the crossing angle $\Delta\theta$. Again the red lines show the amplitude of the wave-averaged surface elevation for a Gaussian wave group $k_0 = 1.90$ m^{-1} and $\Delta k = 0.65$ m^{-1}, for degrees of spreading $\sigma_\theta = 10, 20, 30°$. The experiments show slight deviation from the Gaussian predictions at $\Delta\theta = 90°$, otherwise they match well. Panel b compares the amplitude of the measured $a_{M-}^{(2)}$ wave-averaged surface elevation

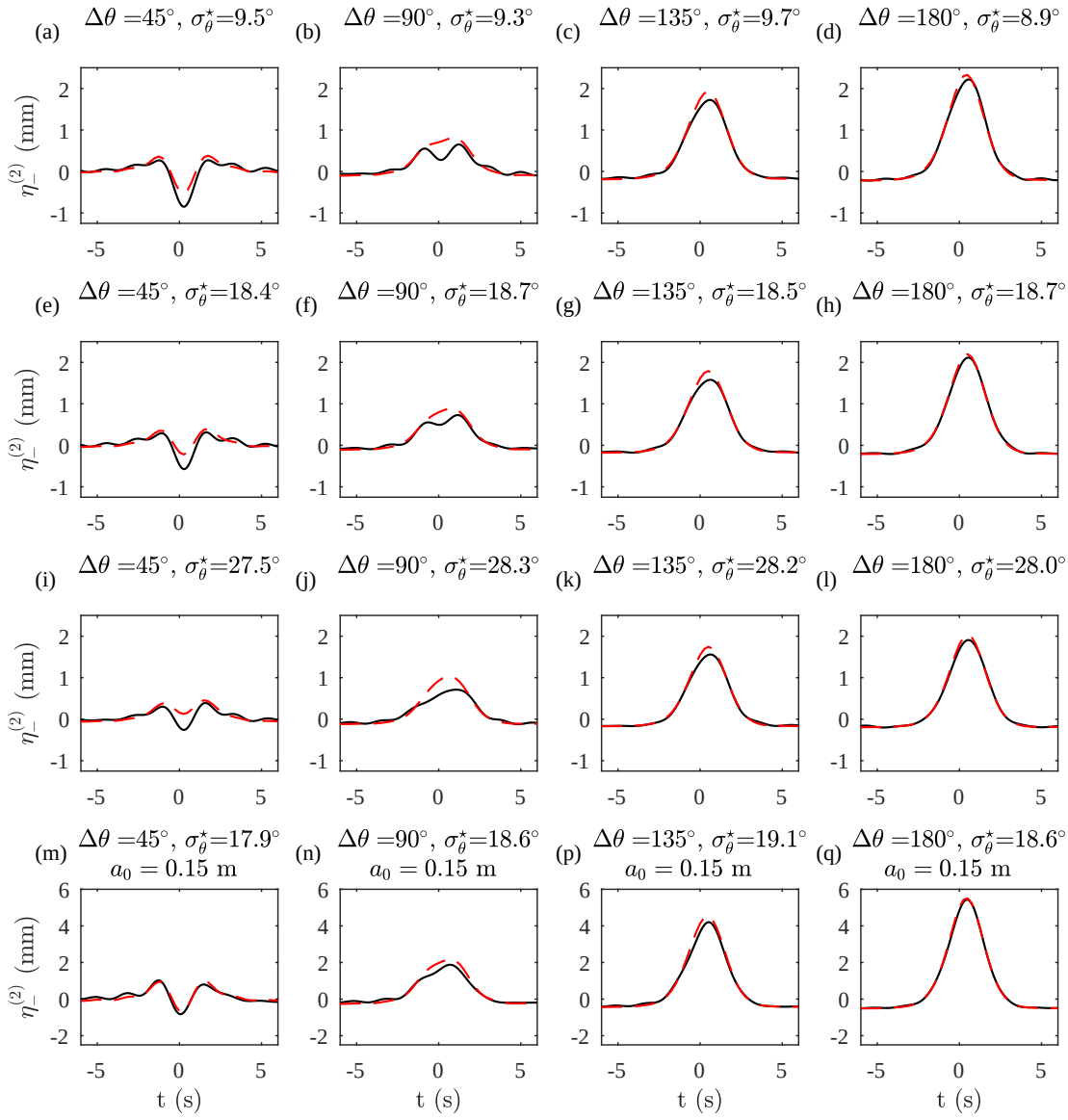

Figure 5.2. Wave-averaged surface elevation $\eta_-^{(2)}$ at the central probe ($x = 0$, $y = 0$) for the crossing tests (category C), showing measured waves $\eta_{M-}^{(2)}$ (black lines) and theoretical predictions $\eta_{T-}^{(2)}$ (red dashed lines) for input amplitude $a_0 = 0.1$ m. The different panels correspond to increasing values of crossing angle $\Delta\theta = 0 - 180°$ for degrees of input spreading $\sigma_\theta = 10, 20, 30°$, and the captions denote the estimated degree of spreading $\sigma_\theta^\star$.

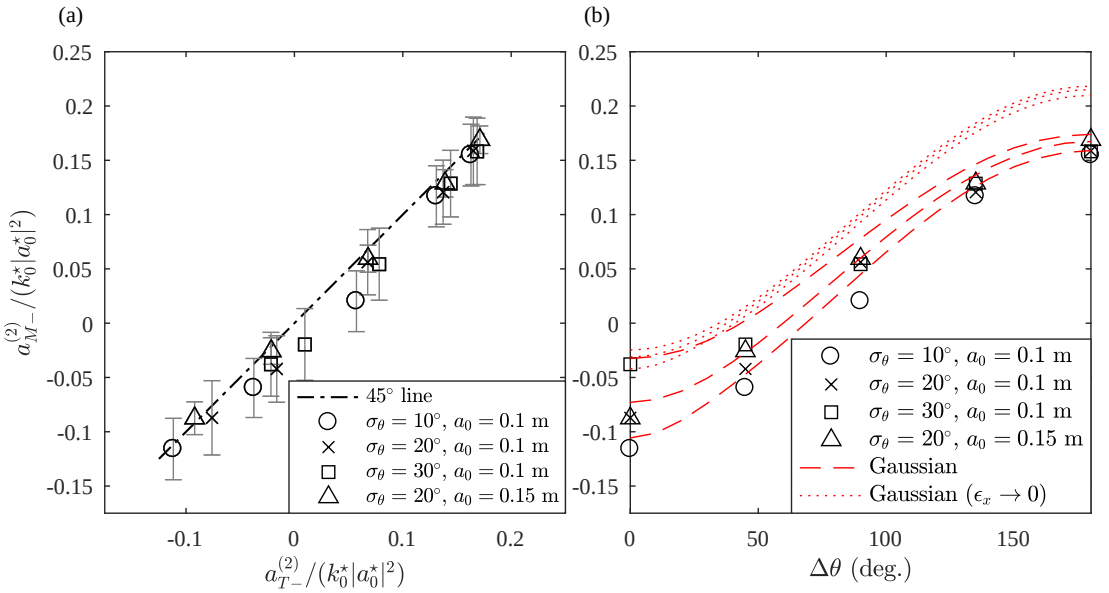

Figure 5.3. Amplitude of wave-averaged surface elevation at the central probe ($x = 0$, $y = 0$) for the crossing tests (category C). Panel a shows the measured mean free surface $a^{(2)}_{M-}$ as a function of the theoretical prediction $a^{(2)}_{T-}$, and panel b shows the measured mean free surface $a^{(2)}_{M-}$ as a function of the crossing angle.

to the calculated theoretically predicted amplitude $a^{(2)}_{T-}$, this illustrates quite how well the theory matches the experiments. For tests with lower crossing angles where there is a set down the results are slightly less accurate, this is most apparent where amplitude approaches zero.

Spatial wave-averaged surface elevation

In the absence of full surface measurements, figure 5.4 compares measured and theoretical wave-averaged surface elevation along the x-axis where nine gauges were located. Measured values of $\eta^{(2)}_-$ shown as black dots correspond to the time of linear focus of each test. Continuous lines were calculated for perfectly focused Gaussian wave groups. The predicted waves calculated using the interaction kernels method, as shown by red dashed lines, are consistently slightly larger than the measured values. Similarly, the predicted waves calculated using the

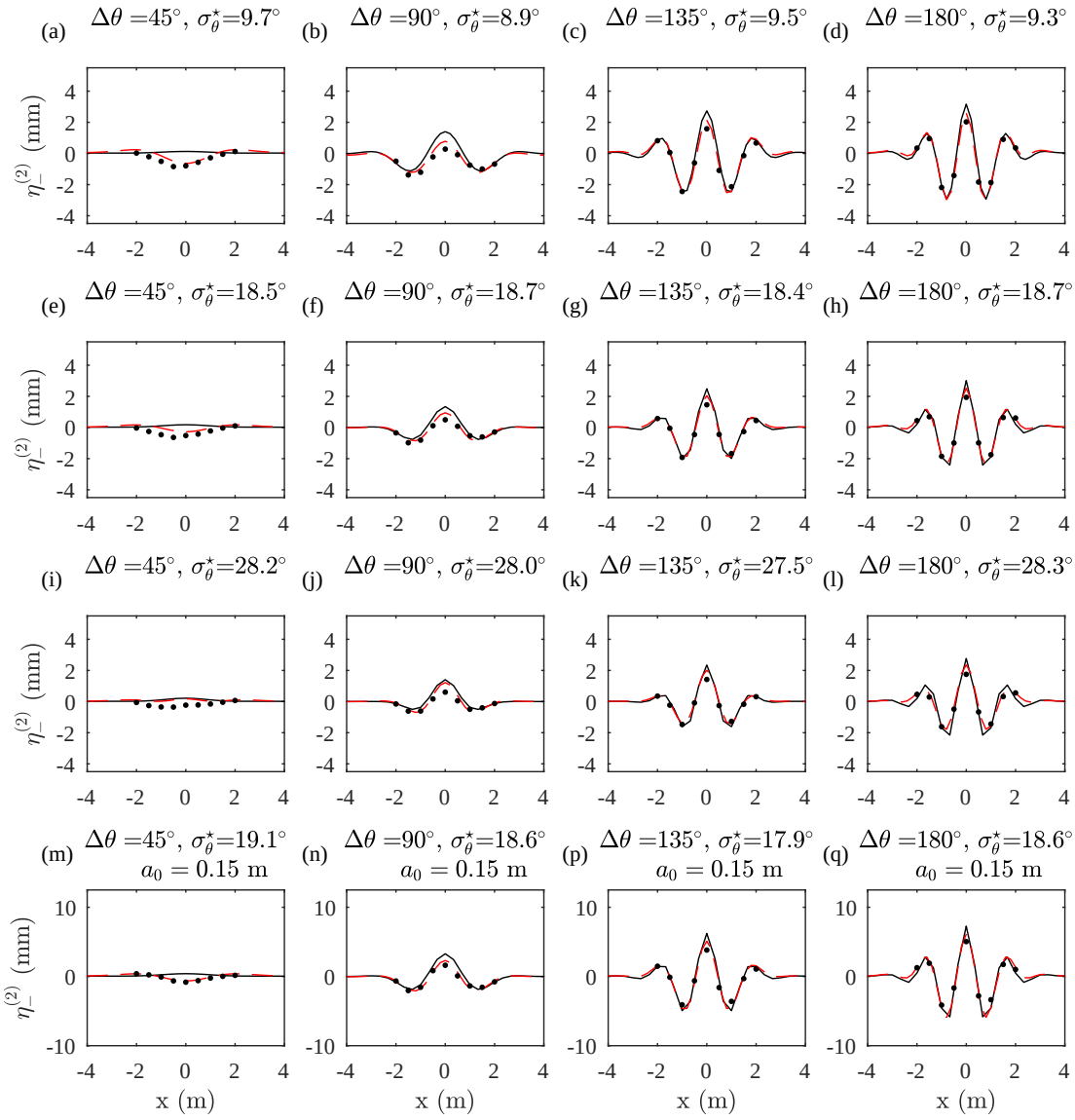

Figure 5.4. Wave-averaged surface elevation $\eta_-^{(2)}$ in the direction of propagation ($x = 0$) at time of linear focus for the crossing tests (category C), showing measured waves $\eta_{M-}^{(2)}$ (black dots) and theoretical predictions $\eta_{T-}^{(2)}$ made using interaction kernels (red dashed lines) and asymptotic approximation (black solid lines) for input amplitude $a_0 = 0.1$ m. The different panels correspond to increasing values of crossing angle $\Delta\theta = 0 - 180°$ for degrees of input spreading $\sigma_\theta = 10, 20, 30°$, and the captions denote the estimated degree of spreading $\sigma_\theta^\star$.

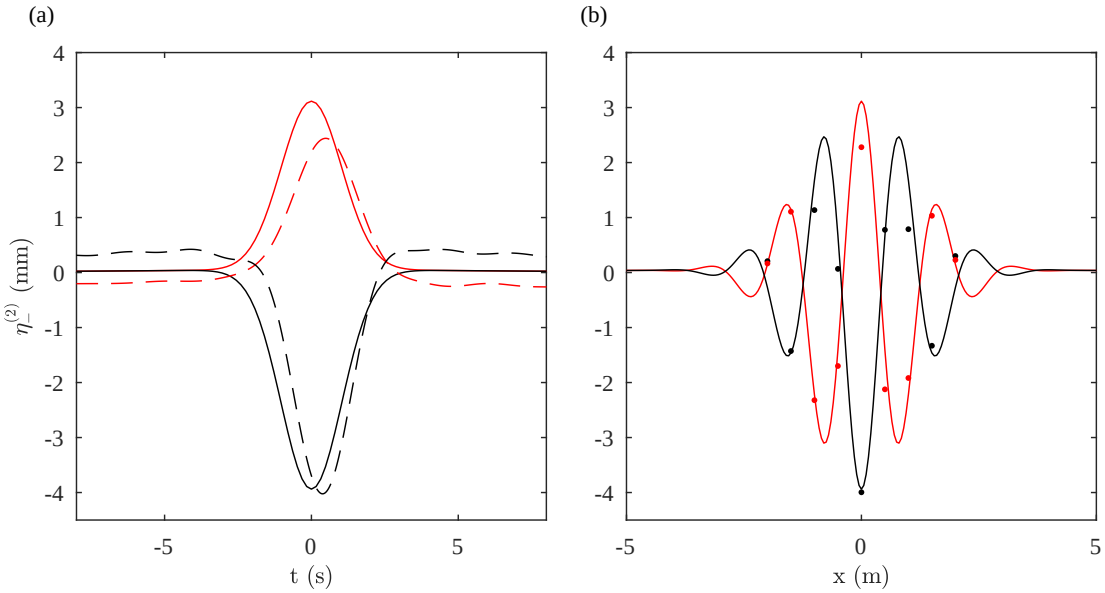

Figure 5.5. Wave-averaged surface elevation $\eta_-^{(2)}$ for two unidirectional wave groups at a crossing angle of $\Delta\theta = 180°$; with both wave groups in phase (red), and a 180° phase shift between groups (black). Theoretical predictions $\eta_{T-}^{(2)}$ made using asymptotic approximation (solid lines) measured values (dots and dashed lines. Panel (a) shows temporal behaviour, and panel (b) shows spatial behaviour.

asymptotic approximation are consistently slightly larger in amplitude than those produced by interaction kernels. In both cases this is most likely to be owing to the effects of imperfect focusing. Importantly all three wave-averaged surface elevations exhibit a fast local structure, that differs drastically from the slow hole or hump formed by an individual wave group.

Phase of interacting wave groups

Examining the role of phase more carefully, figure 5.5 compares the wave-averaged free surface for two opposing unidirectional wave groups ($\Delta\theta = 180°$) that are in-phase ($\varphi_1 = \varphi_2$) and out-of-phase ($\varphi_1 - \varphi_2 = 180°$). When the phase of one group is shifted by 180°, the wave-averaged surface elevation is reversed, becoming negative as predicted by (3.3) and (3.4). It is also evident from this figure the 'hole' is deeper than the 'hump', as the set-down is not a function of

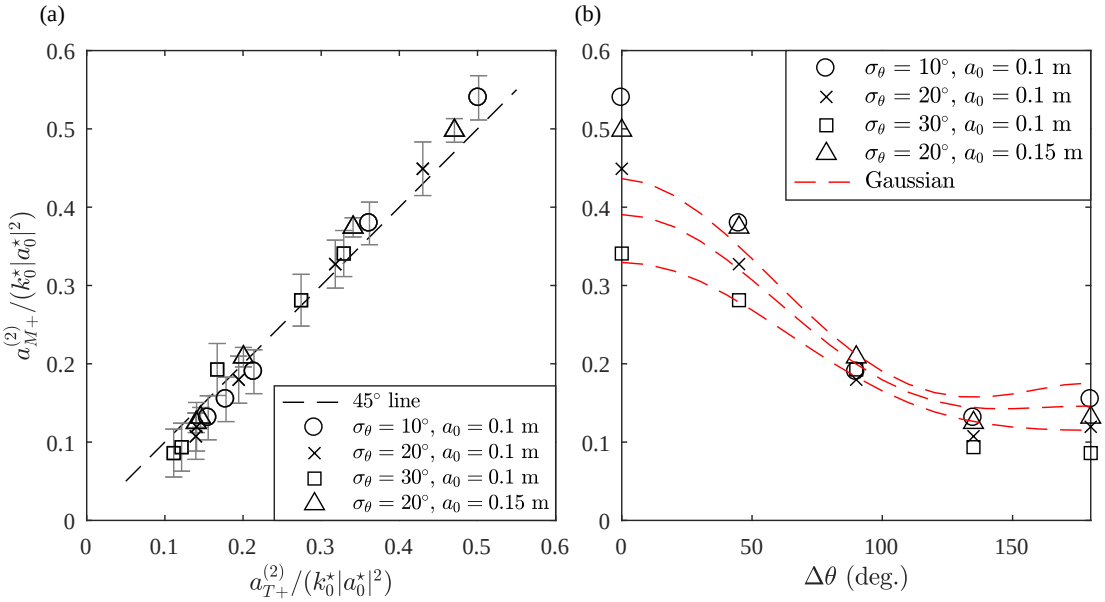

Figure 5.6. Amplitude of second-order sum waves at the central probe ($x = 0$, $y = 0$) for the crossing tests (category C). Panel (a) shows the measured mean free surface $a^{(2)}_{M-}$ as a function of the theoretical prediction $a^{(2)}_{T-}$, and panel b shows the measured mean free surface $a^{(2)}_{M-}$ as a function of the crossing angle.

phase and always remains negative, whilst the 'set-up' changes sign. Nevertheless, it is worth emphasizing that in the in-phase case ($\varphi_1 = \varphi_2$) the linear signal constructively interferes and the 'hump' contributes to an already large and positive crest, whereas in the out-of-phase case ($\varphi_1 - \varphi_2 = 180°$) the linear signal de-constructively interferes and the 'hole' combined with second-order sum components is the only observable feature. Finally, due to its (partial) standing-wave nature the set-up varies slowly in time (panel a), whilst varying rapidly in space. In time and space, the set-up is subject to the same slow modulation associated with the product of the crossing groups, which travels at twice the group velocity from the perspective of a stationary observer.

5.1.4 Sum waves

In addition to the wave-averaged surface elevation the amplitude of the sum waves $\eta_+^{(2)}$ are presented in figure 5.6. The time series of $\eta_+^{(2)}$ are provided in Appendix B. Panel (a) plots the measured amplitude of the sum waves $a_+^{(2)}$ as a function of crossing angle. As with the spreading tests $a_{M+}^{(2)}$ is slightly larger than expected for Gaussian wave packet low crossing angles, otherwise a they are well matched. Panel (b) compares theoretical predicted amplitude of sum waves $a_{T+}^{(2)}$ to $a_{M+}^{(2)}$, again here agreement between theory and experiments reduces proportional with amplitude.

5.2 Conclusions

Herein, results are presented from detailed experiments of the wave-averaged surface elevation for compact directionally spread crossing waves on deep water ($k_0 d \gg 1$). Experimental observations are compared to second-order theory; first, using existing Fourier base spectral summation, secondly a modified multiple scales approach for crossing wave groups is used. Experiments show excellent agreement with predictions made using the approach of Dalzell [1999], and with modified multiple-scales approach where a set-up dominates $\Delta\theta > 50-70^\circ$ (figure 5.3b).

The spatial structure of the set-up that occurs as a result of crossing wave groups, is found to have a completely different form to that observed for individual wave groups. Here, the wave-averaged surface elevation takes a form of the same scale as the linear wave along the mean direction of the two wave groups.

The practical implications of the change between a set-down to a set-up can be illustrated by considering a large typical wave group of linear crest height $a_0 = 10$

m, a peak period of 12 s on a water depth of 140 m, representative of realistic severe conditions, and chosen to correspond approximately to the non-dimensional water depth and steepness in the scaled experiments ($k_0 d = 3.9$, $k_0 a_0 = 0.28$, and $\epsilon_x = 0.3$). For single wave groups with degrees of spreading of $\sigma_\theta = 10$, 20, 30 and 40°, the predicted modifications of the maximum crest height due to set-down or set-up of the wave-averaged free surface are -0.22, -0.12, 0.00 and $+0.13$ m, respectively. The contributions from the frequency-sum components, would be $+1.4$, $+1.2$, $+1.0$ and $+0.83$ m, giving a total crest modification at second order of $+1.1$, $+1.1$, $+1.0$ and $+0.96$ m. Unlike the wave-averaged free surface, which is slowly-varying in time and slowly-varying (set-down) or rapidly-varying (set-up) in space, the frequency-sum components are rapidly varying in both space and time (at twice the frequency and wavenumber).

For two identical wave groups with a small degree of individual spreading $\sigma_\theta = 20°$ that cross at angles of 45, 90, 135 and 180° and have a combined linear amplitude of 10 m at the point of crossing, predicted modifications of the maximum crest height due to set-down or set-up of the wave-averaged free surface are $+0.00$, $+0.27$, $+0.50$ and $+0.60$ m, respectively. The contributions from the frequency-sum components, would be $+1.0$, $+0.63$, $+0.45$ and $+0.45$ m, giving a total crest modification at second order of $+1.0$, $+0.90$, $+0.96$ and $+1.1$ m. Here, as the crossing angle increases, the contribution from the frequency-sum components decreases by approximately the same amount as the contribution from the set-up increases. In reality, it is likely that crossing waves that result from wind and swell systems will be of different frequencies, which will affect the magnitude of the set-up at large angles. Nevertheless, this study reinforces the notion that the crossing of waves presents a likely scenario for the observation of a large set-up observed under extreme or freak waves in the oceans. The effects of finite water depth of the linear waves ($k_0 d = O(1)$) will act to increase the magnitude of the set-up, which will be considered in future work.

Part II

Directional estimation of ocean measurements

Chapter 6

Field data and quality control

Field measurements of free surface elevation present an invaluable resource for the understanding of ocean processes, and the validation of associated theories and models. However, field data are inherently noisy and often plagued by instrumentation error. Quality control is a vital step in the analysis of *in situ* free surface elevation measurements. The North Alwyn dataset used herein comprises a large number of measurements made during storms, where inclement weather conditions (among other issues) adversely affect data quality. Furthermore, the extreme conditions observed during storms may themselves appear as anomalies. The energetic nature of these measurements and the possible confusion between real and erroneous observations, makes the quality control process a non trivial task, heightened by the large volume of data (over 20 000 measurements). The following chapter provides a brief overview of the North Alwyn platform; its location, data acquisition system, and instrumentation. A short review is presented of quality control methods, and the results summarised.

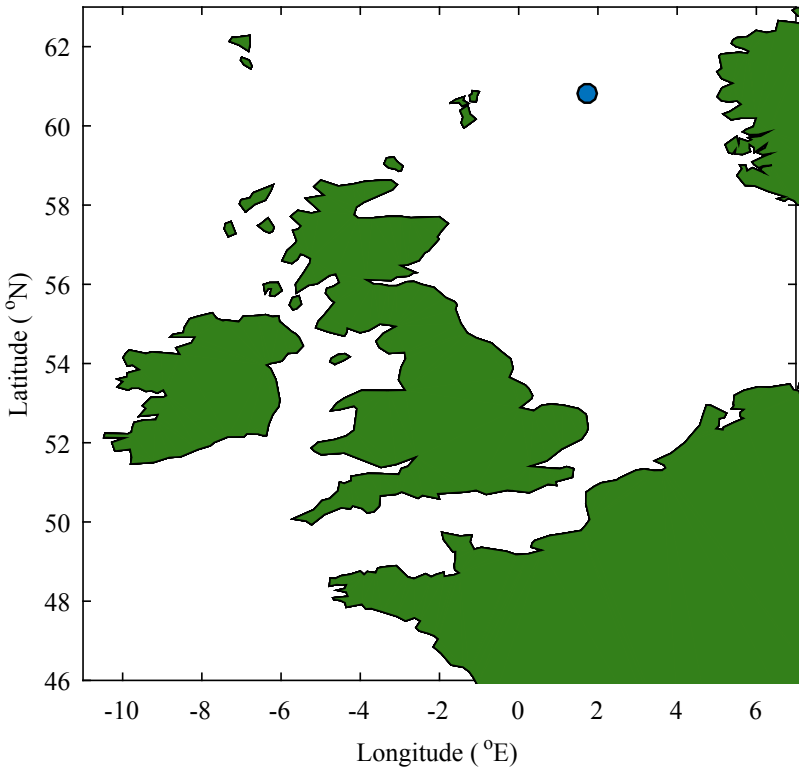

Figure 6.1 Map showing location of North Alwyn platform (blue dot)

6.1 North Alwyn dataset

6.1.1 North Alwyn platform

The ocean wave data considered herein were all obtained from single point gauges located on the North Alwyn Platform, a fixed jacket offshore structure located in the northern North Sea at ($60^o48.5'$N,$1^o44.17'$E) about 150 km east of the Shetland Isles (Figure 6.1). Mean water depth at the platform was 130 m. The platform comprised two structures, North Alwyn A (NAA) and North Alwyn B (NAB), connected by a bridge (Figure 6.2). The platform substructure was sparse, with each support column of diameter $D = 1.5$ m. The wavelength of

incoming waves was typically of the order of $L = 100$ m. Hence, $D/L << 0.2$ and the North Alwyn Platform can be considered as being composed of small diameter cylinders, meaning that wave-structure interactions such as reflections and diffraction were negligible [Sawaragi, 1995] and did not significantly affect the recorded observations of the surrounding wave field.

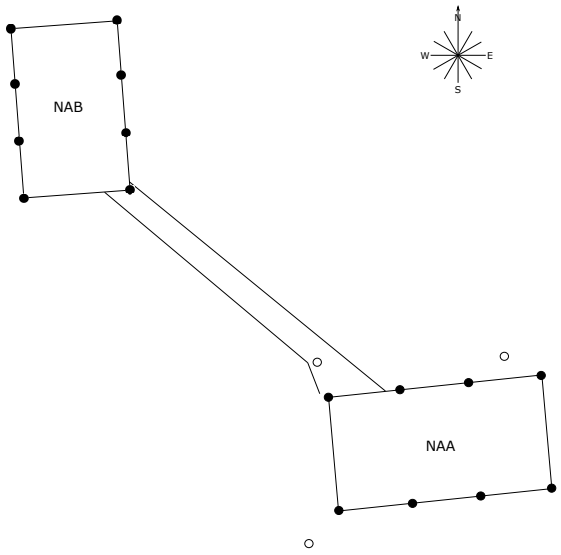

Figure 6.2 Schematic showing layout of North Alwyn platforms NAA and NAB

6.1.2 Instrumentation

The measurement devices were all located on North Alwyn A, and comprised three Thorn EMI infra-red laser probes that simultaneously measured sea surface elevations (Figure 6.3). The probes were set out in plan as nodes of a triangle with side lengths of about 50, 51, and 72.5 m. The probe resolution was $\pm$ 5 cm (i.e. accurate to within 1%). A Labtech Notebook on the platform was used to control data acquisition, undertake preliminary data processing, and provide local data storage. The PC acquired data at 5 Hz, via an XE software package. Raw data were split into 20-min blocks for statistical treatment. Further details are given by Wolfram et al. [1994].

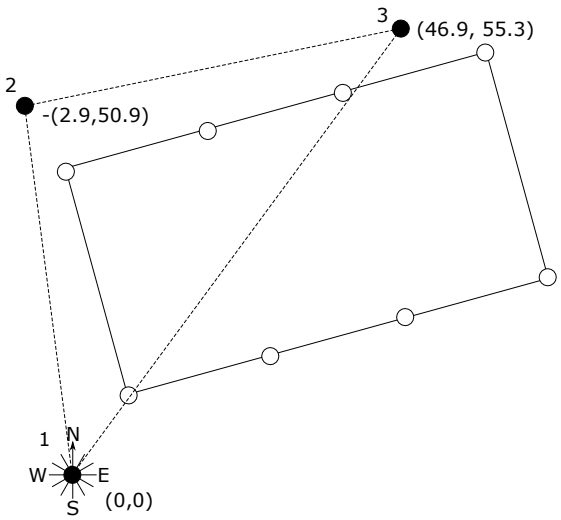

Figure 6.3. Schematic showing arrangement of North Alwyn measurement array in plan

In addition to wave height, a Munro IM 146 anemometer, located 102 m above the mean water level, recorded the wind speed and direction at NAA. The information from both sets of sensors was continuously logged and split into 20 minute sections. The wind measurements were converted into mean values of wind speed and direction.

6.1.3 Measurement procedure and availability

Free surface elevation data were recorded over a ten year period from 1994-2004. The data measurements were continuously monitored, and values stored when either the significant wave height H_s exceeded 3.5 m or the wind speed was greater than 16 ms^{-1}. A total of 448 individual 'storms' made up the North Alwyn dataset, comprising 16,422 separate 20-minute duration files, each containing three concurrent sets of measurements.

The availability of data between 1994 and 1997 is limited to selected storms, whereas from 2000-2004 all recorded storms were made available. Therefore, the

Year	*Storms*	*Files*	Coverage
1994	1	177	0.673%
1995	5	658	2.5%
1996	1	71	0.27%
1997	5	1241	4.72%
2000	176	5972	22.7%
2001	100	2272	8.65%
2002	108	4019	15.3%
2003	52	2012	7.66%
Total:	448	16422	-

Table 6.1 North Alwyn dataset

coverage for these years is disproportionately low. The thresholds were designed to have approximately a 25% exceedance probability 2000, which is nearly met in 2000.

6.2 Quality control procedure

There are a wide range of approaches adopted in the quality control of real-time data; those that directly pertain to measurements of free surface elevation have been collected by the Coastal Data Information Program (CDIP). The CDIP have collected information on tests and error flags from the following institutes: the Integrated Ocean Observing System (IOOS), Qauality Assurance of Real Time Ocean Data (QARTOD) manual, the Field Research Facility (FRF) of the Coastal and Hydraulics Laboratory, and the International Ocean Commission (IOC). These flags have been designed primarily for waverider buoys and pressure transducers, flags pertaining specifically to such devices have been omitted. Flags relevant to Eulerian observations are summarised in Table 6.2, similar entries have been combined. The time series obtained by Lagrangian means are similar in form to those produced by laser wave gauges, and so the majority of flags still apply.

Test/Flag	QARTOD	CDIP	FRF	IOC
Gap Test/Raw Data Timing	×	×	×	×
Spike/ Gross Error Limit	×	×	×	×
Range test	×	×	×	
Mean shift	×	×		×
Acceleration/Jump	×	×	×	
Slope				×
Energy/Variance	×	×	×	
Mean/Water depth		×	×	
Series comparison		×	×	
Flat/Equal values		×		×
Data stability				×
Equal Peaks		×		
Mean crossings		×		
Period distribution		×		

Table 6.2 Summary of quality control tests and error flags

Christou and Ewans [2014] performed analysis of a similar quantity of wave data, the focus of this analysis was on freak waves. Full detail of the quality control used in the their study is given by Christou and Ewans [2011]. Due to similarities in requirements, the quality control procedure in this study will draw significantly from this. Freak waves are anomalous events in themselves; accordingly Christou and Ewans [2011] detail a quality control process with certain flags specific to data including freak waves. Drawing from both the information in Table 6.2 and Christou and Ewans [2011], the following flags have been used for quality control of the data used in this study:

1. Five consecutive points of equal value
2. Zero down-crossing period $> 25s$
3. Limit rate of change S_y, first and second derivative
4. Energy in spectrum at frequencies below $0.04Hz > 5\%$ of total

5. Energy in spectrum at frequencies above $0.6Hz > 5\%$ of total

6. Are H_s and T_p physical values

It is important to note that a zero tolerance approach has been adopted, meaning that if any one of the five flags occur, the time series is discarded. This approach was necessary, because the analysis in Chapter 7 is very sensitive to measurement quality. In a situation where a smaller number of measurements are available and discarding a large amount is an issue, time series can be appended and cropped to remove erroneous measurements.

Figure 6.4, presents three illustrative examples of typical erroneous measurements contained within North Alwyn dataset, which were detected by the QC process. Panel a shows a time series where the maximum steepness flag 3 was triggered. Here the majority of waves are acceptable, apart from two impossibly steep waves that occur after around 350 s. In panel b flags 1,2, and 5 are triggered simultaneously, for these flags this was typical where the gauge is clearly experiencing serious issues locating the free surface. Finally, panel c contains a free surface elevation time series where the effects of high frequency noise can be seen, resulting in the triggering of flag 5.

As with Christou and Ewans [2014] the limiting rate of change flag 3, was found to be overly sensitive, failing waves that upon visual inspection appeared to be legitimate. The flag was modified to when both the slope and acceleration exceed S_y. This amended flag is still very sensitive. The limiting rate of change is defined as:

$$s_y = \frac{2\pi\sigma}{T_z}\sqrt{2lnN_z} \tag{6.1}$$

where σ is the standard deviation of the time series, T_z is the mean zero down-crossing wave period, and N_z is the number of down-crossing waves in the sample. This is derived from the assumption of a Gaussian sea-state

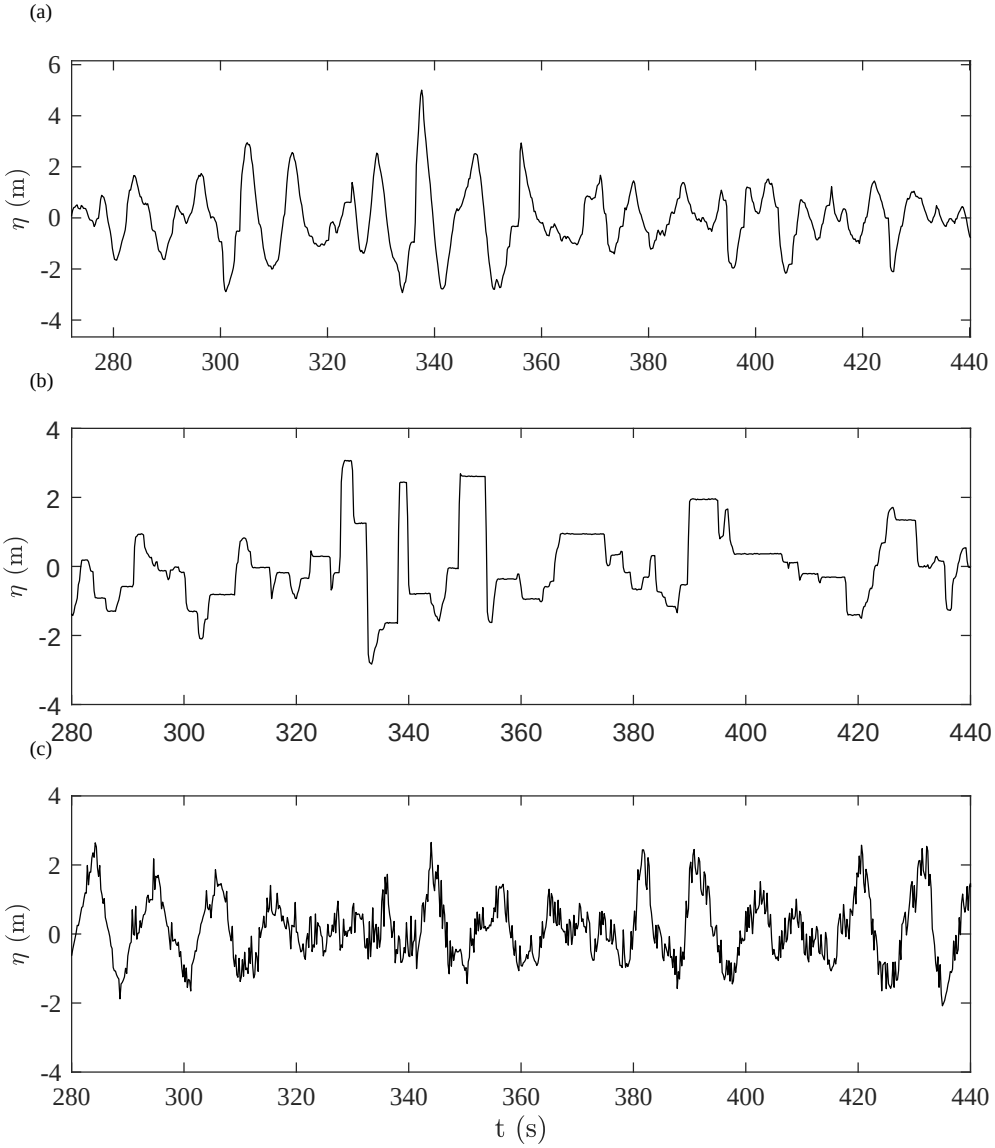

Figure 6.4. Examples of errors flagged by the quality control process; flag 3 (panel a); flags 1,2,5 (panel b); and flag 5 (panel c).

(Marios Christou personal communication,06 May,2015), where the most probable maximum amplitude a_{MP} is:

$$a_{MP} = \bar{a}\sqrt{\ln(N_z)} \tag{6.2}$$

For a sine wave the Root-Mean-Squared (RMS) amplitude $\bar{a}$ is $\bar{a} = \sigma\sqrt{2}$, therefore:

$$a_{MP} = \sigma\sqrt{2\ln(N_z)} \tag{6.3}$$

Similarly for a regular sine wave, the free surface elevation may be expressed as:

$$\begin{aligned} \eta(t) &= a\sin(kx - \omega t) \\ \therefore \frac{\partial\eta}{\partial t} &= -a\omega\cos(kx - \omega t) \end{aligned} \tag{6.4}$$

Hence the maximum temporal slope is defined as:

$$\begin{aligned} \left.\frac{\partial\eta}{\partial t}\right|_{max} &= |-a\omega\cos(kx - \omega t)| \\ \therefore \left.\frac{\partial\eta}{\partial t}\right|_{max} &= a\omega \end{aligned} \tag{6.5}$$

If T_z is the mean zero-crossing period corresponding to N_z and $w = 2\pi/T$ substituting maximum amplitude Eqn (6.3) gives Eqn (6.1).

Visual verification

Certain errors will escape the quality control process and can only be identified visually. This process can be somewhat subjective, and so, as with the zero tolerance approach above, a conservative viewpoint has been taken with all marginal cases being discarded. For data where a suspiciously large crest or trough was observed, when concurrent probe measurements were available authenticity was assessed through comparison; an example of this is discussed in chapter 7.

Year	Storms	Files	QC passed	3 Probes QC passed
1994	1	177	172	124
1995	5	658	595	0
1996	1	71	148	22
1997	5	1241	1659	0
2000	176	5972	7698	185
2001	100	2272	2581	12
2002	108	4019	4792	44
2003	52	2012	3157	4
Total:	448	16422	20802/49266	391/16422

Table 6.3. North Alwyn Dataset: availability of measurements between 1994-2004, and results of quality control process

6.2.1 Results

Having assessed the quality of the measurements at each probe for every data file in every storm, the data files were divided into three categories. Files where data at all three probes were found to be bad quality were discarded from further analysis. Of the remaining data, files where all three probes were simultaneously of good quality were identified, these files may be used to perform conventional estimates of the directional spreading. Finally, files which contained freak waves, were identified, as such waves may effect the analysis performed in chapter 7. Here, a freak wave is defined as a wave with height two times the significant wave height H_s [Haver, 2001]. Table 6.3 details the results of the quality control process, showing the total number of passed measurements and files for which all three probes passed, which do not include freak waves. Of the dataset 391 of the files had good quality measurement at all three probes, and 20802 individual measurements of a possible 49266 (16422×3) passed the QC process. A large number of the data are discarded. Although undesirable, this is necessary here owing to the subsequent analysis. The retention of data could be improved by

making use of machine learning, in assessing the fidelity of measurements on a wave-by-wave basis.

6.3 Conclusions

Detailed background information has been provided on to the North Alwyn dataset used in Chapter 7. A method is presented for the quality control of a large volume of free surface elevation measurements. It is understood that this method is severe in the discarding of data; however, this is made necessary by the sensitivity of the analysis performed in Chapter 7 to sudden changes in slope. Further work may include, the implementation of machine learning in the distinction of erroneous and real measurements.

Chapter 7

Estimation of directional spreading from point measurements

Ocean waves have multidirectional components. Most wave measurements are taken at a single point, and so fail to capture directly information about the relative directions of the wave components. Conventional means of directional estimation require a minimum of three concurrent time series of measurements at different spatial locations in order to derive information on local directional wave spreading. Here, the relationship between wave nonlinearity and directionality is utilized to estimate local spreading without the need for multiple concurrent measurements, following Adcock and Taylor [2009], with the assumption that directional spreading is frequency independent. The method is applied to wave elevation observations recorded at the North Alwyn Platform in the northern North Sea, and the results compared against estimates of wave spreading by conventional measurement methods and hindcast data. Records containing freak waves were excluded. It is found that the long-wave method provides accurate estimates of wave spreading over a range of conditions experienced at North Alwyn, despite the noisy chaotic signals that characterise such ocean wave data. The results provide further confirmation that Adcock and Taylor's long-wave method is applicable to metocean data and has considerable future promise as a technique to recover estimates of wave spreading from single point wave measurement devices.

7.1 Introduction

The relative directions in which wave components travel have a substantial effect on their combined kinematics and dynamics, as illustrated in chapter 3. This has significant implications in coastal and ocean engineering, including design codes for offshore oil platforms, ship safety, optimisation of wave energy devices, and the dispersion of oil slicks and plastic contaminants. For the majority of wave observations made in the oceans, the relative directions of the underlying wave components remain unknown because the observations are usually made in isolation as point measurements. The conventional way of overcoming this problem is to use either an array of three or more instruments [Benoit et al., 1997, Forristall and Ewans, 1998] or multi-degree-of-freedom devices [Mitsuyasu et al., 1975, Barstow and Kallstad, 1991, Walsh et al., 1985] such as radar, clover-leaf buoys, and wave-rider buoys.

Another approach is to exploit the relationship between wave nonlinearity and wave directionality. The majority of waves in the ocean are weakly nonlinear; therefore their observed time series will contain second-order nonlinearities Longuet-Higgins [1963]. The connection that exists between nonlinearity and directionality as observed experimentally by Johannessen and Swan [2001], Onorato et al. [2009], and in the field by Forristall and Ewans [1998], and Toffoli et al. [2007], provides a means by which information on local directional spreading can be inferred from the nonlinearites that lie within a single point measurement. To exploit this connection, it is necessary to extract the linear free waves and second-order bound waves from the wave elevation time signal, and then fit second-order wave theory to the bound wave signal using an assumed spreading function, and hence estimate the spreading from the optimal fit. Walker et al. [2004] presented an approximate method for separating out the linear free waves and second-order bound waves contained within an observed free surface elevation

time series, through filtering in the frequency domain and minimizing skewness. For a prescribed wave spreading function involving a combination of interacting freely propagating linear waves, the resulting bound waves can be calculated to second-order using interaction kernels derived for finite depth by Dalzell [1999]. Using this theory, the bound waves associated with a given set of free waves are simply a function of their component directions. By comparing the predicted bound second-order difference waves for an assumed spreading distribution to the actual bound second-order difference waves contained within the original measurement, Adcock and Taylor [2009] derived a method for estimating the local directional spreading for a point measurement. This approach, herein called the 'Long-Wave Method (LWM)' was satisfactorily validated using experimental data obtained by Cornett et al. [2002] and numerically generated data with the addition of random noise. Adcock et al. [2011] used the same approach to infer the conditions that gave rise to the Draupner wave of 1st January, 1995 from information acquired by a single point gauge, and found that directional spreading was of key importance in understanding the extreme event. The results were found to be consistent with other nearby observations [Haver, 2004, Rosenthal and Lehner, 2008].

Here, Adcock and Taylor's method is applied to a large dataset of observations from three measurement devices located on the North Alwyn platform in the northern North Sea. By examining high quality data signals from all three devices, comparison is made between estimates of directional spreading using the single probe LWM and conventional methods. Where data are of insufficient quality from any of the three devices, comparison is drawn with hindcast data obtained from the European Centre for Medium-Range Weather Forecasts (ECMWF).

Year	Storms	Files	QC passed	3 Probes QC passed
1994	1	177	172	124
1995	5	658	595	0
1996	1	71	148	22
1997	5	1241	1659	0
2000	176	5972	7698	185
2001	100	2272	2581	12
2002	108	4019	4792	44
2003	52	2012	3157	4
Total:	448	16422	20802/49266	391/16422

Table 7.1. North Alwyn Dataset: availability of measurements between 1994-2004, and results of quality control process (repeated from Chapter 6)

7.2 Data

The Ocean wave data considered herein were all obtained from single point gauges located on the North Alwyn Platform. This dataset and its quality control are discussed in full in Chapter 6. Table 7.1 summarises the data from North Alwyn that passed the quality control process and were used in this chapter. In addition to observations made at North Alwyn, hindcast data are also utilised.

7.2.1 Hindcast data from European Center for Medium Range Weather Forecasts

The European Center for Medium Range Weather Forecasts (ECMWF) provides publicly available meteorological datasets produced by hindcast models. The data used herein were taken from the ERA-20C model which provided hindcast atmospheric information based on an assimilation of historic global observations for the entire 20th Century. Model outputs included a wide range of meteorological data; of these, the key metocean parameters were hindcast using a WAM model

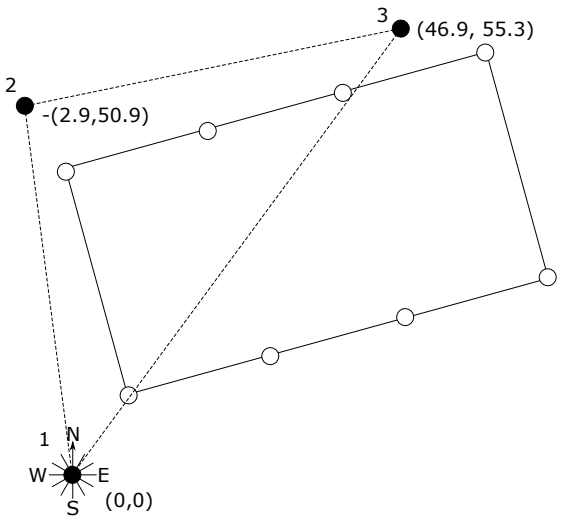

Figure 7.1. Schematic showing arrangement of North Alwyn measurement array in plan

[Poli et al., 2013]. The WAM model outputs spectra, discretized at 36 directions and frequencies. The 'wave spectral directional width' σ_{θ_E} output had a spatial resolution of $\delta x = 28\ km$ and temporal resolution of $\delta t = 3$ h. A full specification of the wave model is given by ECMWF [2016].

7.3 Method

7.3.1 Linearisation

In order to calculate the bound waves for a given time series of free surface elevation above mean water level $\eta(t)$, the linear free waves $\eta^{(1)}$ must first be extracted. The data were linearised following the procedure outlined by Walker et al. [2004]. Second-order difference waves $\eta^{(2)}_{F-}$ were removed by high-pass filtering the data at half the peak frequency. Second-order sum nonlinearity was then removed by adjusting the Stokes' S_{22} parameter to minimise the skewness of the resulting linear time series.

$$\eta^{(1)} = \eta_F - \frac{S_{22}}{h}\left(\eta^2 - \hat{\eta}^2\right) \tag{7.1}$$

where h is the mean water depth, and $\eta^{(1)}$ is the linearised, η_F is the high-pass filtered, and $\tilde{\eta}$ is the Hilbert-transformed, time series obtained from η. Here, $\eta^2 - \hat{\eta}^2$ provides an approximation for the $\cos(2\varphi)$ double frequency term, based on the assumption that the waves are narrow-banded. The skewness of $\eta^{(1)}$ is calculated using

$$\gamma = \frac{1}{N\sigma^3}\sum_{n=1}^{N}(\eta^{(1)})^3, \tag{7.2}$$

where N is the number of data points and σ is the standard deviation of the linearised time series.

7.3.2 Second-order calculations

Wave-wave interaction of linear freely propagating waves causes nonlinear bound waves which occur at increasing order with decreasing amplitude. Second-order bound waves occur as a result of interacting wave pairs, at the sum and difference of their constituents. The sum terms occur in the tail of the spectrum and overlap the linear waves. However, the difference terms occur at the low end of the spectrum where they dominate linear waves, owing to the faster decay of the linear spectrum. This makes it easier to separate out the difference waves.

Here, difference waves resulting from a linear spectrum are calculated using the interaction kernels derived by Dalzell [1999] for finite depth. The method behind these calculations is explained in full in Chapter 2, the essential steps are briefly revisited below.

7.3.3 Spreading estimation

Point Measurement - Long-Wave method

Theoretical difference waves can be produced for any arbitrary spreading distribution using the linearised time series $\eta^{(1)}$, as the interactions of of linear harmonic components where amplitude a, and phase φ are derived from the FFT of the linearised time series $\eta^{(1)}$.

$$\eta^{(2)}_{T-} = \sum_{n=1}^{N_\omega}\sum_{m=1}^{N_\omega}\sum_{i=1}^{N_\theta}\sum_{j=1}^{N_\theta} D(\theta_i)D(\theta_j)a_n a_m B^{-}\left(\mathbf{k}_{n,i},\mathbf{k}_{m,j},\omega_n,\omega_m,h\right)\cos\left(\varphi_{n,i}-\varphi_{m,j}\right)(\delta\omega)^2(\delta\theta)^2, \tag{7.3}$$

Here, the predicted difference waves, $\eta^{(2)}_{T-}$, are compared to observed difference waves, $\eta^{(2)}_{F-}$ that were extracted by filtering the measured free surface time series η, by taking the Euclidean norm,

$$\Delta_{lw} = \frac{\sqrt{\sum\left(\eta^{(2)}_{T-}-\eta^{(2)}_{F-}\right)^2}}{\sqrt{\sum\left(\eta^{(2)}_{F-}\right)^2}}. \tag{7.4}$$

The value of Δ_{lw} is then minimised by varying the assumed spreading distribution. In this case a wrapped-normal distribution is used, where the spreading value σ_θ corresponds to standard deviation of a Gaussian spreading distribution in θ

$$D(\theta) = \frac{D_0}{\sqrt{2\pi}\sigma_\theta}\exp\Big(-\frac{1}{2}\Big(\frac{\theta-\theta_0}{\sigma_\theta}\Big)^2\Big), \qquad \text{for} \qquad -180^\circ \le \theta \le 180^\circ, \tag{7.5}$$

It is assumed that spreading is frequency-independent. The value $\sigma^\star_\theta$ that minimises Δ_{lw} and hence provides the optimum fit between the observed and theoretical difference waves $\eta^{(2)}_{T-}$ and $\eta^{(2)}_{F-}$ is determined as the best estimate of the local spreading.

By performing the foregoing LWM analysis on the entire dataset, any data for which the method did not successfully minimise the long-wave difference between $0 - 90°$ were discarded. Data where freak waves were located were also removed, because such waves have been shown to cause anomalous second-order difference waves [Adcock et al., 2011]. Here, a freak wave is defined as a wave with up or down-crossing height greater than twice the significant wave height H_s [Haver, 2001].

Array Measurements

Where data of sufficiently high quality were simultaneously available from the three gauges at North Alwyn, the Iterative Maximum Likelihood Method (IMLM) [Pawka, 1983] is used to estimate the directional spectrum $D(\theta)s(\omega)$. From this spectrum, the spectrally-weighted frequency-independent spreading distribution $D(\theta)$ is calculated, and a wrapped-normal spreading distribution with standard deviation σ_{θ_D} fitted to $D(\theta)$. The uncertainty of this method is dependent on a number of variables, an attempt to quantify this for this specific situation is made in section 7.5.2.

7.4 Sensitivity

7.4.1 Goodness of fit

The long-wave difference Δ_{lw} is primarily used as a goodness-of-fit parameter, in finding the optimal assumed spreading value $\sigma_\theta^\star$. However, Δ_{lw} also provides information on the quality of fit that was achieved in finding $\sigma_\theta^\star$. High values of Δ_{lw} corresponding to $\sigma_\theta^\star$ imply that the fit may not be particularly satisfactory

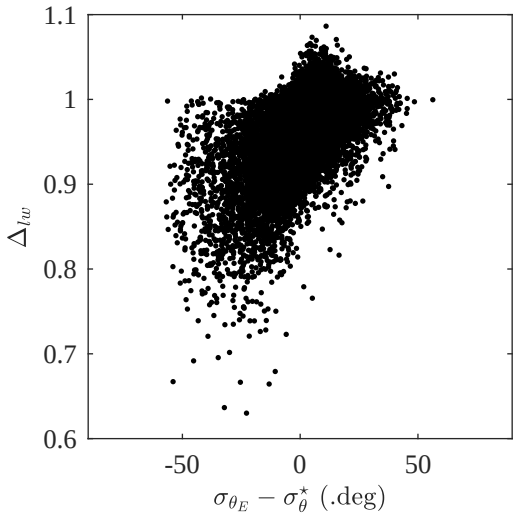

Figure 7.2. Scatter plot of goodness-of-fit Δ_{lw} as a function of spreading error for the LWM compared to the ECMWF hindcast

despite $\sigma^\star_\theta$ being the best fit. Where a good fit is not achieved, the accuracy of $\sigma^\star_\theta$ may be affected adversely. Figure 7.2 shows how Δ_{lw} varies against the spreading error $\sigma_{\theta_E} - \sigma^\star_\theta$, where σ_{θ_E} is the value of spreading predicted by the ECMWF hindcast. In this instance, hindcast data are used for mainly illustrative purposes; the validity of this comparison is discussed in §7.5.1. However suitable the comparison may be, large differences in spreading are clearly indicative of error. For $\Delta_{lw} \gtrapprox 1$, the error $\sigma^\star_\theta - \sigma_{\theta_E} \to +$, meaning $\sigma^\star_\theta < \sigma_{\theta_E}$ and the spreading is underestimated. As $\Delta_{lw} \to 0$, the error also reduces. However, for $\Delta_{lw} < 0.8$, the spreading is over-estimated. In such cases a seemingly good fit is achieved (as indicated by the very low value of Δ_{lw}) despite a large discrepancy in the predicted value of spreading. Visual inspection of the results indicated that this arose from erroneous measurements. Figure 7.3 shows an example of this type of error, where near flat sections or sudden changes in slope that are missed by the quality control process cause pronounced set-ups in the filtered second-order difference waves $\eta^{(2)}_{F-}$. In this example there are two similarly sized waves in $\eta(t)$ occurring at around 580 and 775 s, of crest height ~ 10 m. Both waves cause set-ups in $\eta^{(2)}_{F-}$ as could be expected for large amplitude crests. The set-ups associated

with the waves are of amplitude ~ 2 m and ~ 0.5 m respectively. The flat section measured in the first wave is clearly an error, and not an artefact of the wave profile. This type of error typically occurs when the sensor loses the free surface temporarily and logs the previously recorded value until the surface is found once more. To assess the effect this error has on $\eta^{(2)}_{F-}$, the flat error was artificially smoothed out as shown by the dashed line in Figure 7.4a. Referring to the array shown in Figure 7.1, the solid line corresponds to measurements at Probe 1 and the grey line to Probe 3 for comparison. Measurements at Probe 2 are omitted in Figure 7.3 owing to poor quality.

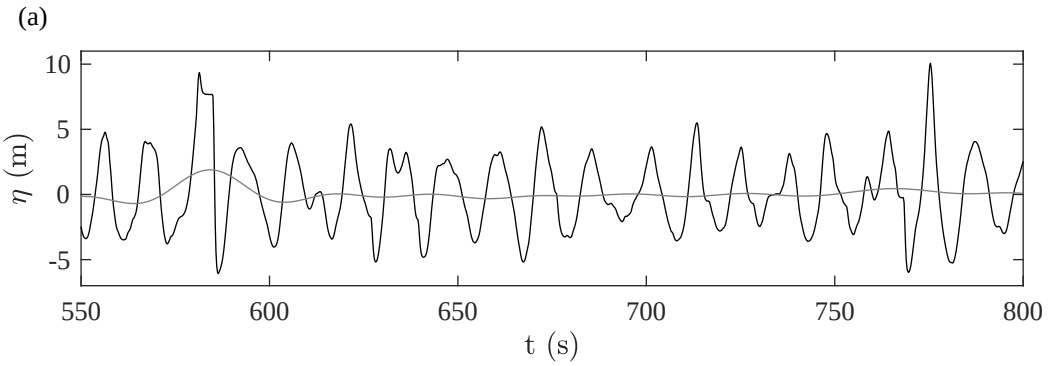

Figure 7.3. Free surface elevation and second-order difference time series at North Alwyn for a selected storm where there is a large set-up in second-order waves owing to measurement error: $\eta(t)$ free surface elevation (black); and $\eta^{(2)}_{F-}(t)$ filtered difference waves (grey).

Linear interpolation was used to remove instrumentation error at the crest of the first large wave, and so the resulting shape of the wave measured at Probe 1 is slightly larger but not dissimilar in shape to the corresponding wave recorded at Probe 3 Figure 7.4a. Filtering the modified time series to obtain $\eta^{(2)}_{F-}$ results in the dashed line shown in Figure 7.4b; the black solid line shows $\eta^{(2)}_{F-}$ for the unmodified time series. The modified time series has an amplitude of ~ 0.65 m, which is comparable to that associated with the second large wave at 775 s.

The LWM spreading estimates from the modified and unmodified time series

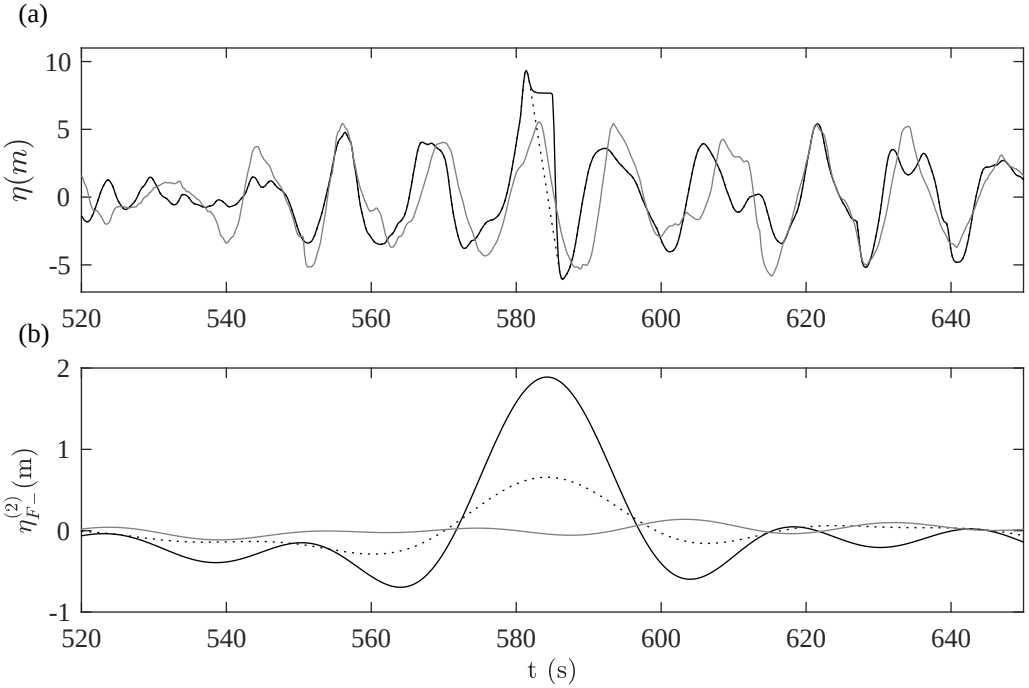

Figure 7.4. Free surface elevation time series at North Alwyn showing unmodified signal (Probe 1, solid black line), smoothed signal (Probe 2, black dashed line), and concurrent measurement from Probe 3 (grey line): a) free surface elevation time series, $\eta(t)$; and b) filtered second-order difference waves $\eta_{-2F}(t)$.

are 34.6°, and 86.3° respectively. The modified value concurs with the prediction made by the ECMWF hindcast of 30.8°, as well as the other values of $\sigma_\theta^\star$ estimated during the rest of the storm.

This approach was extended to Storm 369 of the North Alwyn dataset, discussed in more detail in §7.5.2. This storm was selected because it possesses three outlying results that derive from obvious measurement errors that have passed the QC process. Additionally, 15 measurements taken during the storm allow for IMLM estimation of σ_{θ_D}, which provides further confidence in the expected values of spreading. Again, available concurrent measurements were used as a guide when smoothing out measurement errors. Table 7.2 lists the results obtained after modifying the erroneous time series. The modified estimates of $\sigma_\theta^\star$ lie much closer to the values of both σ_{θ_E} and σ_{θ_D} which indicate that $\sigma \approx 31°$

Outlier	Raw		Modified	
	$\sigma_\theta^\star(.deg)$	Δ_{LW}	$\sigma_\theta^\star(.deg)$	Δ_{LW}
a)	76.6	0.942	39.6	0.971
b)	46.4	0.915	31.1	0.989
c)	52.4	0.839	28.1	0.996

Table 7.2. Error reduction for Storm 369,showing the spreading estimates for the unmodified and modified time series that correspond to the three outliers.

for Storm 369. For all three cases, this relatively simple approach reduces the associated error in predicted spreading, despite reducing the goodness of fit. The interpolation method used to smooth out errors has a significant effect on the estimate of $\sigma_\theta^\star$. As there is no way of establishing for certain the true waveform, it is not suggested that this approach is used as a means of producing spreading estimates. However, the results presented here illustrate a particular source of sensitivity which does not lie with the LWM itself. It is obvious that errors undetected by the quality control process can result in gross overestimation of the spreading. Herein, visual inspection was used. In practice, a more robust means of error detection is desirable.

NewWave comparison

NewWave [Tromans et al., 1991], depicted in Figure 7.5a constitutes a focused wave group where all free wave components are in phase at $x = 0$ and $t = 0$. In practice, this waveform is used as a design wave because it provides an accurate approximation to the shape of the largest waves contained within ocean observations (see e.g. Santo et al. [2013]). Similarly, the second-order difference waves $\eta^{(2)}_{NW-}$ corresponding to this profile can be used to provide an approximation to those expected in large wave events [Adcock and Draper, 2015]. The phasing and shape of actual waves affect the amplitude of $\eta^{(2)}_{F-}$, causing some scatter about

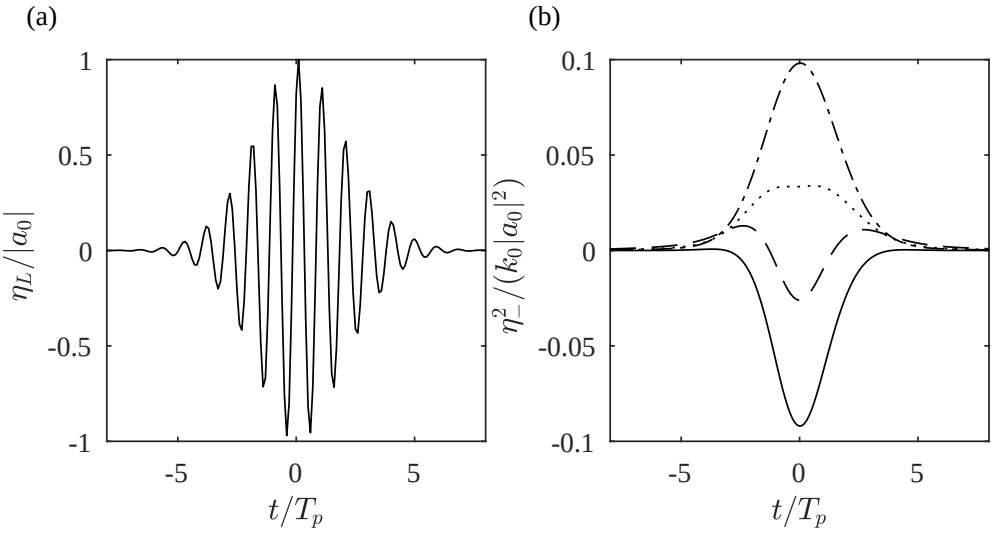

Figure 7.5. NewWave comparison: (a) linear focused wave group free surface elevation time series $\eta^{(1)}$ at $x = 0$; and (b) resulting second-order difference wave time series $\eta_-^{(2)}$ for $\sigma_\theta = 0°$ (solid line), $\sigma_\theta = 15°$ (dashed line), $\sigma_\theta = 30°$ (dotted line), and $\sigma_\theta = 15°$ (dot dashed line).

the NewWave approximation. Even so, this approach provides a general guide to the amplitude that should be expected for a given set of conditions. For a given spectral density $S(\omega)$, the corresponding new wave profile is calculated as

$$\eta_{NW}(t) = \frac{\sum_{n=1}^{N} S(\omega_n) \cos(\omega_n t)}{\sum_{n=1}^{N} S(\omega_n)}, \tag{7.6}$$

in which t is time from focus, located at $x = 0$. Using the linear NewWave profile $\eta_{NW}^{(1)}$, the second-order difference bound waves $\eta_{NW-}^{(2)}$ are calculated using (7.3) as shown in Figure 7.5b. The second-order difference amplitude associated with the NewWave profile normalised by significant wave height $a_{NW-}^{(2)}/H_s$, can then be used to establish whether or not the observed set-up in amplitude $a_{F-}^{(2)}/H_s$ found in $\eta_{F-}^{(2)}$ is feasible. When normalised in this way, the value of $a_{NW-}^{(2)}/H_s$ depends upon peak period T_p and spreading angle, with the assumption that the corresponding linear amplitude of the NewWave profile is $a^{(1)}/H_s = 1$ for a Joint

North Sea Wave Project (JONSWAP) spectrum with peak enhancement factor 3.3. Therefore, a NewWave amplitude can be calculated for each measurement using the appropriate values of T_p and σ_{θ_E}. The ratio of $a^{(2)}_{F-}/H_s$ to $a^{(2)}_{NW-}/H_s$ provides an understanding of whether the set-up in $\eta^{(2)}_{F-}$ is likely to be the result of a large wave or arising from an anomaly. Figure 7.6 shows the effect of using

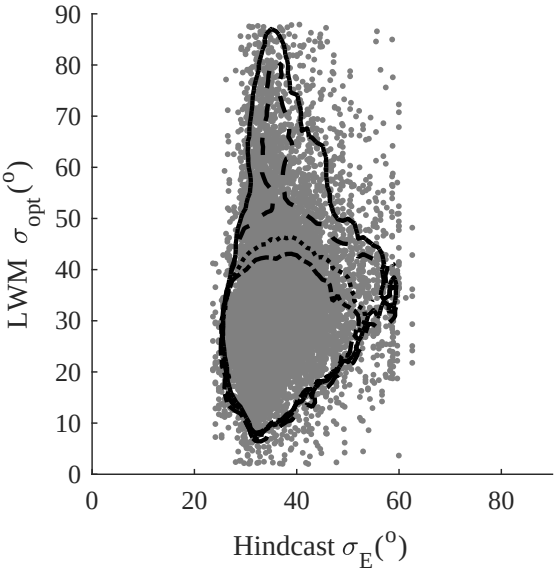

Figure 7.6. Scatter diagram showing LWM estimate spreading values filtered using NewWave amplitude ratio, $a^{(2)}_{-}/a^{(2)}_{NW-}$ plotted against hindcast estimates of spreading (grey dots), with superimposed contours showing 95% confidence values; results screened using amplitude ratio $a^{(2)}_{-}/a^{(2)}_{NW-}$ values < 100 (solid line), < 25 (dashed line), < 10 (dotted line), and < 5 (dot-dashed line).

$a^{(2)}_{F-}/a^{(2)}_{NW-}$ as a quality control parameter. Values of $\sigma^{\star}_{\theta}$ are plotted against the corresponding values of σ_{θ_E}. Overlaid are the 95% contours when the data are screened using decreasing ratios of $a^{(2)}_{F-}/a^{(2)}_{NW-}$ from 100 to 5. At a high ratio of $a^{(2)}_{F-}/a^{(2)}_{NW-}$ the amplitude observed in the measurement is much larger than would reasonably be expected; conversely as the ratio is reduced, results where the long wave estimate is grossly overestimated are progressively filtered out. This further illustrates the method's sensitivity to measurement errors. The

results from the North Alwyn data confirm that NewWave provides an effective *a posteriori* method for error detection.

7.4.2 Cut-off frequency

Abnormal set-ups in the filtered difference waves, $\eta^{(2)}_{F-}$, have been shown above to result from errors in the measured time series η. Moreover, if the linear spectrum does not decay as sharply as expected, large-amplitude linear components arise in $\eta^{(2)}_{F-}$ that can dominate the smaller-amplitude second-order components. The resulting increases in $\eta^{(2)}_{F-}$ amplitude may adversely affect the values estimated by the LWM. To overcome this, the frequency at which the original data η are filtered is reduced in order to obtain $\eta^{(2)}_{F-}$ which is uncontaminated by the effect of any linear components that lie close to the original frequency cut-off. This was examined by applying the LWM to the entire dataset with difference waves filtered at $0.5f_p$, $0.4f_p$, and $0.3f_p$. No difference in the estimated values of $\sigma^{\star}_{\theta}$ was discernible when different frequency cut-offs were used.

7.5 Results

7.5.1 Correlation with ECMWF hindcast

For the majority of the data, measurement quality does not permit conventional directional estimation, and so an indirect means of comparison is necessary. Here, the wave spectral directional width σ_{θ_E} produced by the ECMWF ERA-20C model is used. The indirect nature and low resolution relative to that of the North Alwyn dataset mean that direct comparison between the values of $\sigma^{\star}_{\theta}$ and σ_{θ_E} is of limited use on a measurement by measurement basis. However, as opposed to

comparing individual values, examination as to how the two sets of data correlate in time is much more informative. From Figure 7.6 it is apparent that the values of spreading produced by the hindcast model appear to be limited to the range of approximately $20° \leq \sigma_{\theta_E} \leq 60°$; it is therefore not possible to assess values of $\sigma_\theta^\star < 20°$, through this means of comparison.

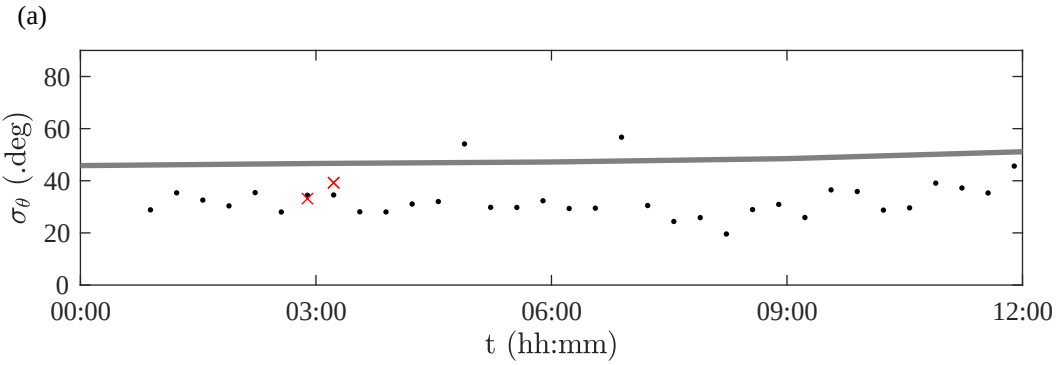

Figure 7.7. Storm 50 of the North Alwyn dataset which shows a bias between ECMWF and LWM estimates of directional spreading: $\sigma_\theta^\star$ (black dots); σ_{θ_E} (grey line); and σ_{θ_D} (red $\times$).

The majority of storms in the North Alwyn dataset are relatively short in duration with an average length of 12 hours, and consequently their spreading shows little temporal variation. For such storms it is difficult to find correlation, and accordingly it is difficult to establish whether either $\sigma_\theta^\star$ or σ_{θ_E} correctly predict spreading if their values are different. Figure 7.7 shows an example of a storm where this is the case. Both the values of $\sigma_\theta^\star$ and σ_{θ_E} show little variation over the duration of the storm, with a gradual increase in spreading as the storm progresses and a mean difference of $\sim 15°$, and it is difficult to draw any immediate conclusions. However, for this particular storm two of the measurement files were suitable for conventional estimation, as shown by the red circles. At about 3 am, the hindcast prediction $\sigma_{\theta_E} = 46.6°$ and the mean of two values either side of 3 am are 36.2 ° and 34.5 ° for σ_{θ_D} and $\sigma_\theta^\star$ respectively. This limited additional information suggests that the values of $\sigma_\theta^\star$ are more likely to be correct, and the hindcast model overestimates the spreading.

When there is variation in spreading predicted by the hindcast model it is possible to establish whether $\sigma_\theta^\star$ is correctly measuring the local spreading. If a strong correlation exists between the values of $\sigma_\theta^\star$ and σ_{θ_E} it is clear that the hindcast is modelling the same conditions as the LWM is measuring. A means of parameterising the correlation observed between the two variables is the correlation coefficient. The covariance of two variables A and B is given by

$$cov(A,B) = \frac{1}{N-1}\sum_{i=1}^{N}\left(A_i - \mu_A\right)\left(B_i - \mu_B\right), \tag{7.7}$$

where μ is the mean value of each signal, and N is the number of samples. The correlation coefficient ρ is then calculated by normalisation, using the standard deviation of both signals,

$$\rho = \frac{cov(A,B)}{\sigma_A \sigma_B}. \tag{7.8}$$

Figure 7.8 shows the temporal behaviour of the 'long wave estimate' of spreading obtained for six storms chosen from the dataset. These storms were selected because they exhibited the strongest correlation between $\sigma_\theta^\star$ and σ_{θ_E} corresponding to the largest values of ρ, whilst having significant temporal variation over their duration. Effects of random uncertainty and/or noise are evident in the values of $\sigma_\theta^\star$. This variability stems from noise that is naturally found in real measurements, causing the standard deviation of the resulting estimates to increase. Adcock and Taylor [2009] used numerically generated examples with artificially added noise to demonstrate that the standard deviation of the resulting values of $\sigma_\theta^\star$ increased as the signal-to-noise ratio decreased. However, the mean value of the estimates remained correct.

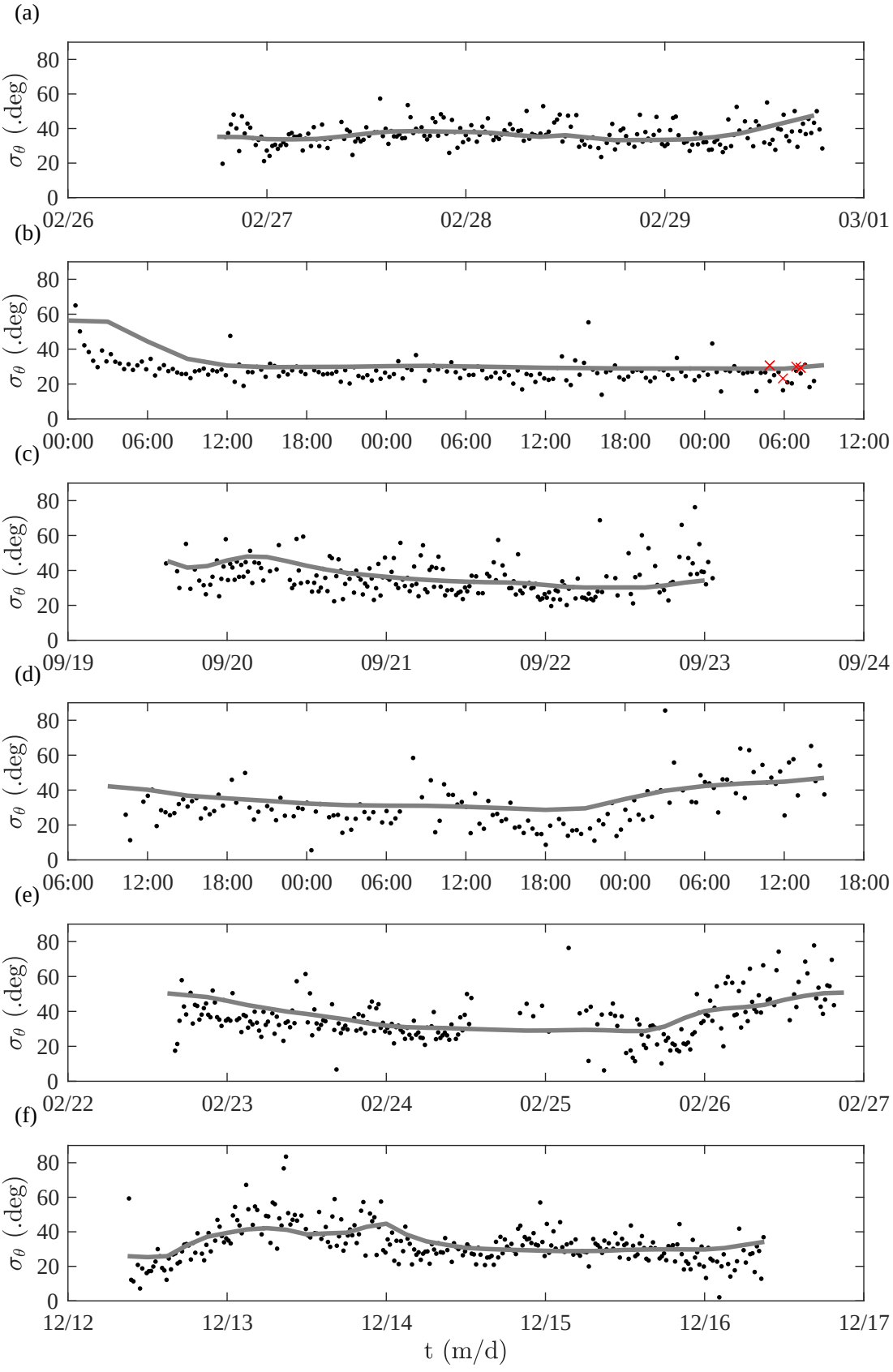

Figure 7.8. LWM spreading estimate and ECMWF hindcast predictions with time. a) Storm 28, b) Storm 30, c) Storm 134, d) Storm 301, e) Storm 320, and f) Storm 435 as detailed in Table 7.3:$\sigma_\theta^\star$ (black dots); σ_{θ_E} (grey line); and where available σ_{θ_D} (red $\times$)

Storm	Start	End	ρ		N
			raw	smoothed	
28	09-Feb-2000 08:58:28	14-Feb-2000 02:39:12	0.268	0.653	207
30	03-Mar-2000 02:14:06	05-Mar-2000 02:34:26	0.528	0.917	166
134	19-Sep-2000 14:47:46	22-Sep-2000 04:32:10	0.316	0.775	196
301	24-Jan-2002 10:21:18	26-Jan-2002 03:21:28	0.648	0.889	140
320	22-Feb-2002 16:09:18	26-Feb-2002 03:29:50	0.494	0.809	222
435	12-Dec-2003 09:12:14	16-Dec-2003 03:32:46	0.566	0.759	265

Table 7.3 Fit parameters of well-correlated storms

Noise contained within the values of $\sigma_\theta^\star$ has an effect on the calculation of ρ. For two perfectly correlated signals where ρ is 1, the introduction of random errors invariably reduces the value of ρ [Emery and Thomson, 2001]. To achieve a better understanding of the true correlation of the results, raw values of $\sigma_\theta^\star$ were smoothed in the time domain with local regression, using weighted linear least squares and a 2nd degree polynomial model. Table 7.3 lists values of ρ for both the smoothed and raw LWM estimates. For the raw results, the values of ρ are relatively low due to noise in the data. Even so, $\rho \gtrapprox 0.5$, except for storms 28 and 134, meaning a weak correlation exists. After data smoothing, all the values of ρ are well above 0.5, with some approaching unity, illustrating a strong correlation between $\sigma_\theta^\star$ and σ_{θ_E}.

Not all of the storms in the dataset show such strong correlation. The indirect nature of the hindcast data means that negative comparisons are fairly inconclusive. However, when the hindcast and measurements exhibit high correlation, this provides conclusive evidence that the LWM is capturing the dynamically changing directional conditions being modelled by the hindcast. It is very unlikely that these two predictions correlate by pure coincidence without being an accurate measure of actual observed conditions.

7.5.2 Comparison with IMLM estimates

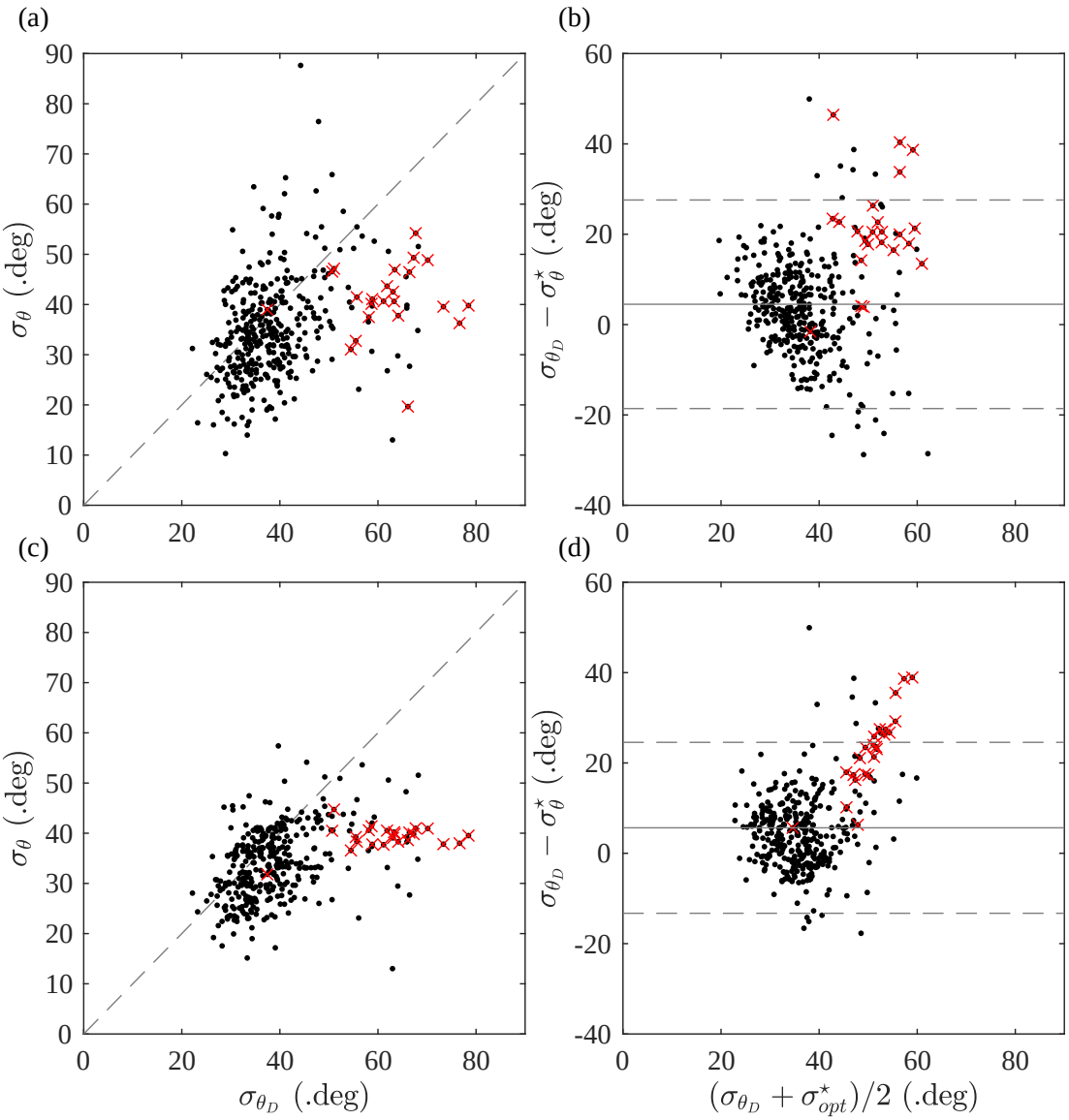

Figure 7.9. Comparison of IMLM and LWM estimates: scatter plot of $\sigma^\star_\theta$ against σ_{θ_D}, a) raw $\sigma^\star_\theta$, and c) smoothed $\sigma^\star_\theta$; and Bland-Altman plot of mean spreading against difference in spreading estimates, b) raw $\sigma^\star_\theta$, and d) smoothed $\sigma^\star_\theta$. Superimposed mean difference (grey solid line), two standard deviation limits of agreement (grey dashed line), all 386 analysed data (black dots), and the results from storm 18 (red crosses).

Of the 448 storms considered herein, 66 storms contain a total of 391 individual measurements for which all three probes pass the quality control process, allowing

estimation of σ_{θ_D}. This represents a very small portion of the entire data set of 16,422 measurements. Unlike the hindcast data estimate σ_{θ_E}, calculation of σ_{θ_D} provides a direct measurement of local spreading. Figure 7.9a shows a direct comparison between the values of σ_{θ_D} and $\sigma_\theta^\star$ calculated for each set of concurrent measurements. The data are scattered about the line $\sigma_{\theta_D} = \sigma_\theta^\star$; as the apparent value of spreading increases, the agreement between the two estimates appears to reduce. Figure 7.9b presents the Bland-Altman plot which displays the difference between σ_{θ_D} and $\sigma_\theta^\star$ against their average value. The Bland-Altman plot illustrates the uncertainty inherent to both sets of estimates and the relationship between magnitude and level of agreement, without assuming that one method is better than the other [Bland and Altman, 1999]. The mean difference for all data, shown by the solid grey line, is 4.98°; this represents the bias between the two methods. As the mean value increases, the agreement between the two methods reduces, and the uncertainty increases. The dashed lines show 95% confidence intervals, which are calculated as twice the standard deviation from the mean; the majority of the data sit within these limits.

Given that the LWM requires only one measurement for each estimate, the number of available estimates means that it is possible to reduce the effects of random uncertainty by smoothing the data in the time domain. Smoothing is achieved using the same approach described in §7.5.1. Figure 7.9 c and 7.9 d show the effect of smoothing the LWM results on the agreement between the two methods. This removes some of the uncertainty associated with $\sigma_\theta^\star$ (as addressed in the previous section) and has two effects. Firstly, the agreement increases for the majority of the data, as evident in Figure 7.9 d where the data are more tightly clustered about the mean. Secondly, it serves to highlight the uncertainty associated with the values of σ_{θ_D}. As the mean value of spreading increases, agreement decreases with a positive bias, owing to the larger values of σ_{θ_D}.

Considering the relatively small sample size, the comparison is sensitive to the

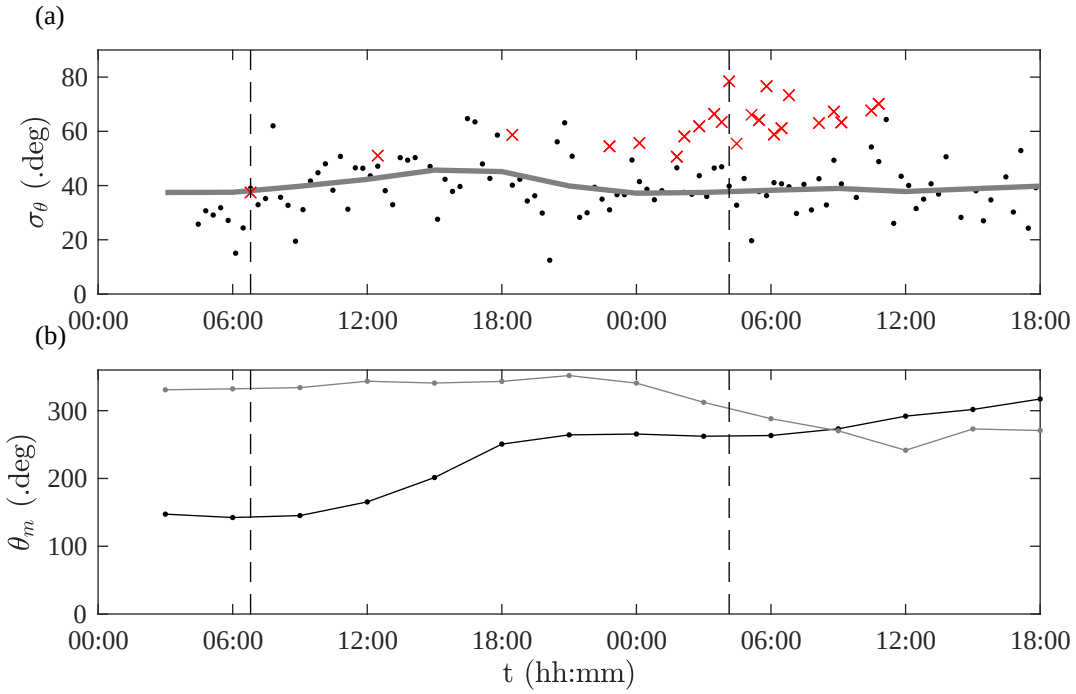

Figure 7.10. Wave spreading results for Storm 18 which exhibit significant disagreement between $\sigma_\theta^\star$ and σ_{θ_D}: a) $\sigma_\theta^\star$ (black dots), σ_{θ_E} (grey line), and σ_{θ_D} (red $\times$); and b) mean directions of wind waves (black) and total swell (grey). Dashed lines in both plots indicate the measurement times of Figures 7.1a & b.

presence of outliers in the data. The majority of outliers stem from Storm 18. Figure 7.10a presents IMLM, LWM, and ECMWF hindcast estimates of spreading over the duration of the storm. In this storm, both $\sigma_\theta^\star$ and σ_{θ_E} follow the same general trend, whereas in the latter half of the storm σ_{θ_D} presents larger values (about 20° greater). The correlation between $\sigma_\theta^\star$ and σ_{θ_E} may suggest that the IMLM is in error in this case. The apparent error in σ_{θ_D} may be a result of crossing-wave conditions. Figure 7.10b shows the mean directions of wind and swell waves predicted by the ECMWF hindcast for Storm 18. The hindcast results suggest that the predominant wind and swell waves were propagating in quite different directions during the storm. Therefore, the complex crossing conditions are being detected by the frequency-dependent IMLM causing an increase in the value σ_{θ_D}. The simplicity of the assumed frequency-dependent spreading distribution used by LWM only allows for the detection of the average

spreading about the mean direction. This is highlighted by Figure 7.11, which shows frequency-dependent directional spectra produced by the IMLM at the start and one day into the storm, indicated by dashed vertical lines in Figure 7.10. Figure 7.11a shows the spectrum calculated from measurements made at 06:47 am on 1st February 2000. At this point in the storm the spectrum has an obvious predominant direction with no signs of major crossing components, and the spreading estimates made by all three sources agree well, as illustrated in Figure 7.10a. Figure 7.11b depicts the spectrum calculated at 04:08 am on the 2nd February 2000. The corresponding spreading estimates shown in Figure 7.10a differ significantly ($\sigma_{\theta_D} = 78.5°$,$\sigma_{\theta_E} = 37.8°$,$\sigma_\theta^\star = 39.8°$) and the directional spectrum exhibits several crossing wind and swell components.

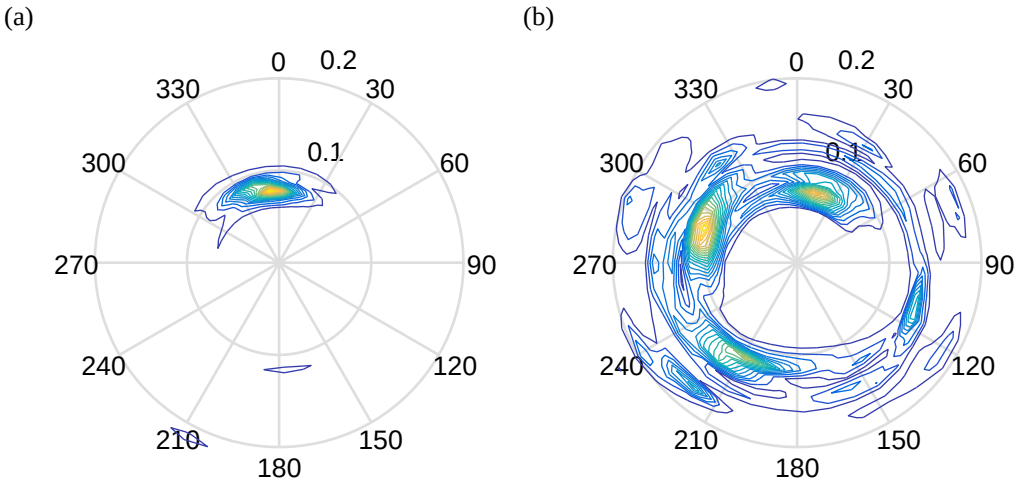

Figure 7.11. Frequency-dependent direction spectra measured during Storm 18, calculated using IMLM: a) 06:47 am 1st February 2000; b) 04:08 am 2nd February 2000.

Figure 7.9 shows that the results from IMLM and LWM have bias of $\sim 5°$, and are in close agreement which reduces slightly as spreading increases. The scatter of results indicates there is uncertainty associated with both methods. Figure 7.12 presents the histograms and kernel density estimates of error between IMLM estimates and both raw, and smoothed LWM results. The histogram in Figure 7.12a, for the raw LWM results, displays symmetry with a normal distribution,

suggesting the errors primarily arise from random noise. The histogram in Figure 7.12b is slightly asymmetric as a result of smoothing $\sigma_\theta^\star$, and exhibits better agreement as a narrowing of the distribution.

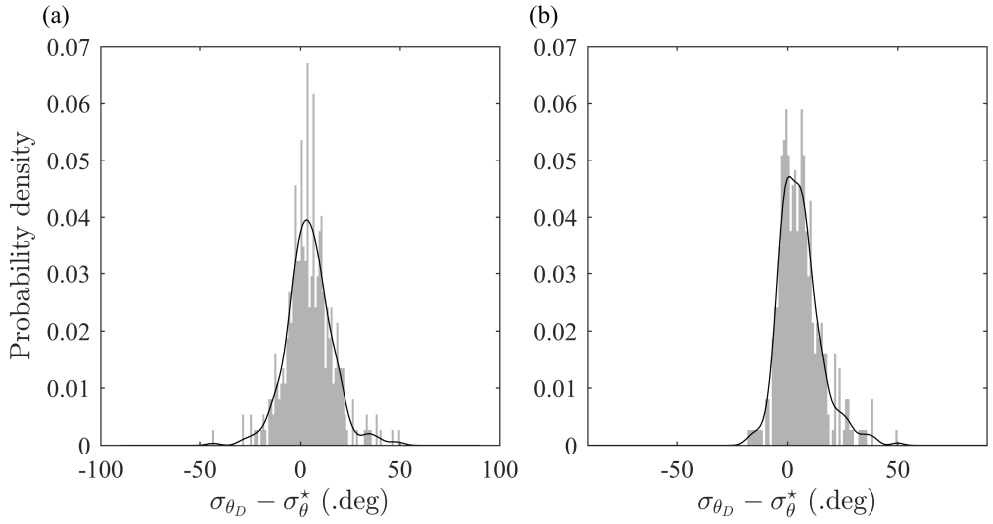

Figure 7.12. Histograms and kernel density of difference in wave spreading estimated by LWM and IMLM methods: a) raw $\sigma_\theta^\star$; and b) smoothed $\sigma_\theta^\star$.

In the dataset there are four storms for which IMLM estimation is possible over their duration and a better understanding can thus be gained of the relative uncertainty of the LWM and IMLM methods. Figure 7.13 displays the four storms detailed in Table 7.4. The first section of Storm 3 was included, and the remainder rejected, in order to preserve data quality and the relative stationarity of spreading. For all four storms, $\sigma_\theta^\star$ (black) and σ_{θ_D} (red $\times$) follow the same trend as the hindcast predictions σ_{θ_E}, with relatively little temporal variation. These examples further reinforce that LWM has correctly estimated the local spreading given that all three estimates are in good agreement. In Figure 7.13d there is a slight time lag between the values of σ_{θ_E} and the other two estimates which are better correlated. This storm also shows slightly more variation in spreading, whereas the other storms remain virtually stationary. Table 7.5 lists values of the mean and standard deviation of the spreading estimates obtained using IMLM

Storm	Start	End	N_{QC}	N_{Dir}
3*	23-Mar-1997 06:19:14	29-Mar-1997 09:26:32	851	110
57	01-Apr-2000 05:38:48	02-Apr-2000 01:58:58	161	36
369	22-Nov-2002 03:40:26	23-Nov-2002 03:20:38	202	15
448	26-Sep-1996 15:58:30	27-Sep-1996 06:38:30	148	22

Table 7.4. Details of selected storms with IMLM directional data, showing the number of high quality time series N_{QC} and directional data N_{Dir}.

Storm	SD			SE			σ_m		
	$\sigma_\theta^\star$	σ_{θ_D}	σ_{θ_E}	$\sigma_\theta^\star$	σ_{θ_D}	σ_{θ_E}	$\sigma_\theta^\star$	σ_{θ_D}	σ_{θ_E}
3	8.87	3.29	0.919	0.820	0.208	0.255	38.1	36.3	33.7
57	7.90	2.94	0.496	0.987	0.298	0.175	30.6	32.2	29.8
369	4.39	3.93	0.819	0.450	0.744	0.237	27.9	30.5	31.8
448	9.93	4.61	4.92	1.20	0.610	1.64	33.5	35.7	36.6

Table 7.5. Fit parameters of IMLM storms, standard deviation (SD), standard error (SE), and mean σ_m for all three estimates of spreading.

and LWM for the four storms. Where the value of spreading remains constant, the standard deviation of each set of estimates provides a satisfactory analogue to uncertainty associated with the particular method employed, assuming that a near-constant value of spreading is a true representation of the actual conditions. Dividing the standard deviation by the square root of the number of samples gives the standard error (SE), which is a measure of variability accounting for the number of samples [Thiébaux, 2013]. The standard error of $\sigma_\theta^\star$ is roughly two to three times that of σ_{θ_D} for all but Storm 369 where $\sigma_\theta^\star$ is just over half the value of σ_{θ_D}. This storm happens to have the lowest spreading value predicted by both methods.

Making the assumption that the smoothed value of $\sigma_\theta^\star$ for each storm is the actual local spreading, the data can be de-trended and a similar analysis performed on

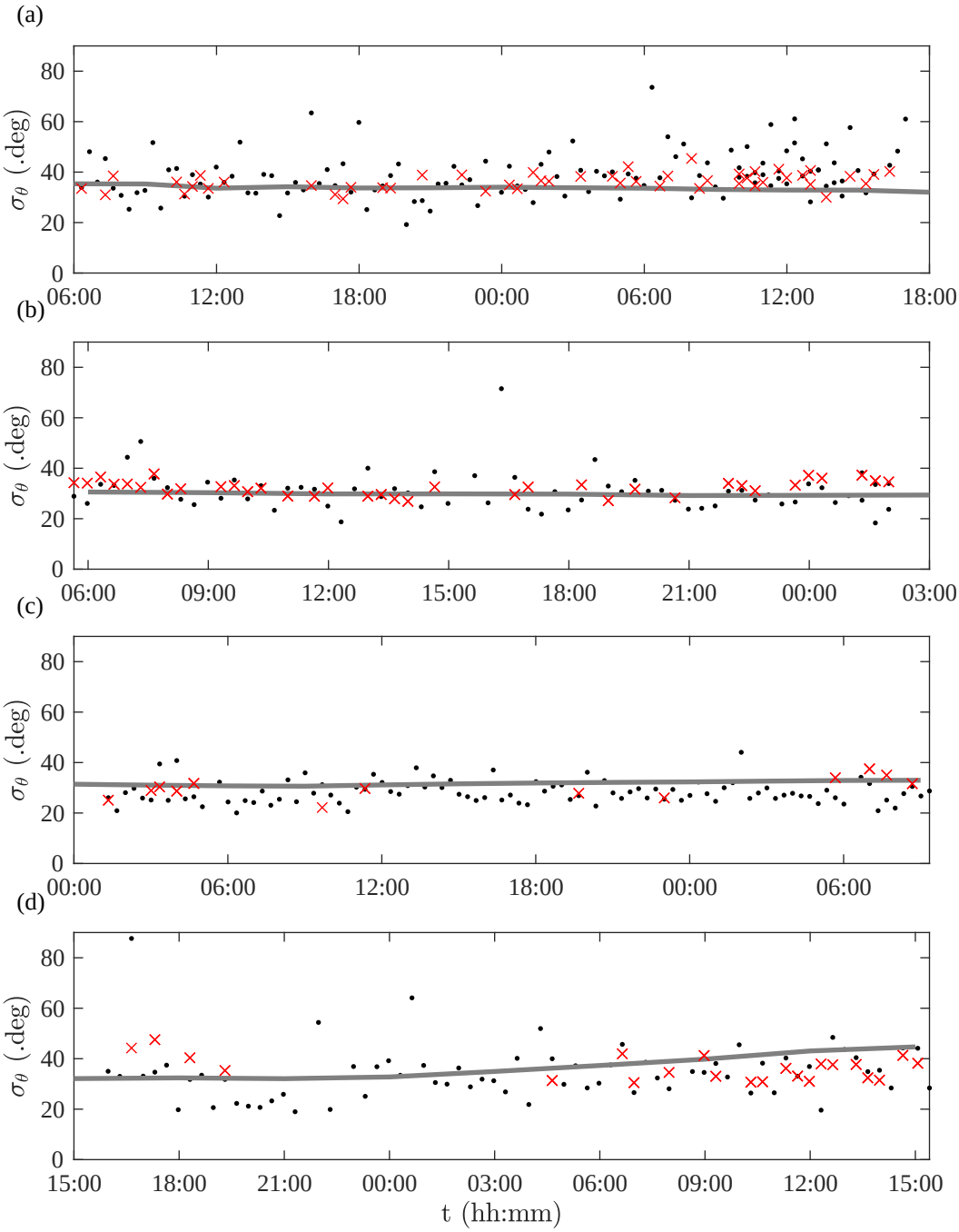

Figure 7.13. LWM, IMLM, and ECMWF hindcast predictions of wave spreading for a) Storm 3, b) Storm 57, c) Storm 369, and d) Storm 448 as detailed in Table 7.4: $\sigma_\theta^\star$ (black dots), σ_{θ_D} (red $\times$), and σ_{θ_E} (grey line).

the entire dataset. Figure 7.14 shows how the standard error of $\sigma_\theta^\star$ varies with the mean value of $\sigma_\theta^\star$ over the duration of each storm plotted as grey dots. The values

for the four storms plotted in Figure 7.13 and listed in Table 7.4 are overlaid. There is a clear positive correlation between the predicted spreading and the standard error. This is an intuitive result because the simplified assumption of frequency-independent wrapped-normal spreading becomes less valid as spreading increases.

As discussed in section 7.5.1 there are a number of estimates $\sigma_\theta^\star < 20°$ which are not within the range of σ_{θ_E}. Figure 7.9a also shows values of $\sigma_\theta^\star < 20°$; however after smoothing the number reduces (Figure 7.9b). Figure 7.14 shows that no storms with multiple concurrent measurements have a mean value of $\sigma_\theta^\star < 20°$, therefore these values are most likely the result of noise.

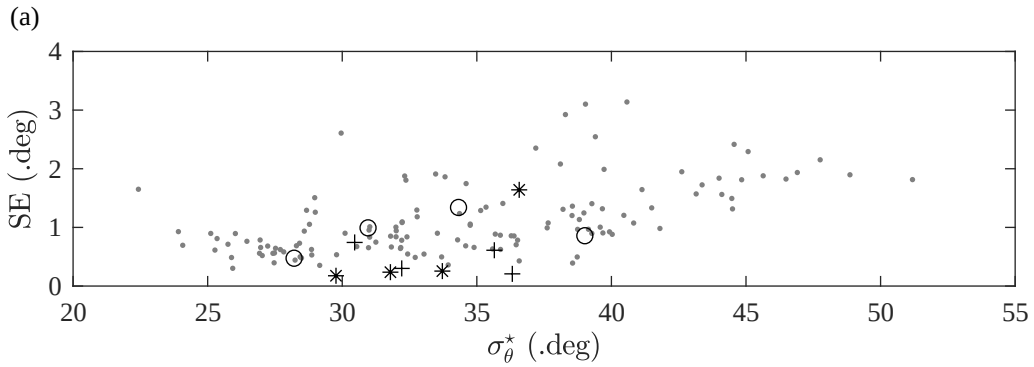

Figure 7.14. Uncertainty measured by standard error versus mean predicted value of spreading for each storm: mean $\sigma_\theta^\star$ (grey dots); Storms from Table 7.4 $\sigma_\theta^\star$ ($\circ$), σ_{θ_D} ($+$), and σ_{θ_E} ($\times$).

7.6 Conclusions

Adcock and Taylor [2009] devised a means of determining directional spreading, called the long-wave method (LWM), which they verified for several deterministic cases and later applied to the 1st January 1995 Draupner wave [Adcock et al., 2011]. Herein, we extend the approach of the LWM to a large dataset of *in situ* ocean observations of free surface elevation obtained from the North Alwyn

Platform in the northern North Sea. The approach taken to implement the LWM, greatly reduced its computational cost. The LWM analysis was based on an assumption that directional spreading was independent of frequency, and excluded records containing freak waves. A method for detecting the influence of erroneous measurements is also presented, which allows *a posteriori* identification of spurious values of estimated spreading. The results of the LWM are compared to values predicted by the ECMWF hindcast model using the North Alwyn data. Despite the indirect nature of this comparison, good temporal correlation is found between the two estimates of spreading for selected storms. This provides confidence in the ability of the LWM to track dynamically-varying directional spreading conditions. By comparing results using a small sample of the overall dataset, it is found that close agreement is achieved between the spreading estimates made by LWM and the iterative maximum likelihood method (IMLM), with the former giving smaller values indicating a slight bias. The LWM exhibits slightly greater uncertainty than the IMLM; however, given that LWM requires only a single measurement, the uncertainty can be reduced by averaging. To gain better understanding of the small bias that exists between the two measurement approaches the performance of LWM at values of $\sigma < 20°$, it is recommended to extend the analysis in future to a dataset containing a much higher proportion of accurate, concurrent measurements. This would enable a quantitative assessment of the relative uncertainty of both methods. The present study has demonstrated that the LWM can be effectively extended to noisy real sea observations, such as prevail at North Alwyn. Available additional information has been used to provide confidence in the accuracy of the results. As with the conventional IMLM method, the LWM is susceptible to the effects of noise which manifests itself in the form of random uncertainty. However, where sufficient results exist, averaging effectively removes uncertainty without requirement of further post-processing. In short, the study has provided further confirmation that the LWM is a viable alternative to conventional means of directional spreading estimation. In practice, LWM offers

a very promising opportunity to gain vital directional information on ocean waves from single-point measurements.

Chapter 8

Conclusions

8.1 Summary and Conclusions

In this thesis the relationship between nonlineartiy and directionality has been experimentally investigated and applied as a tool obtain directional information from oceanographic data. All the work carried out in the foregoing chapters relied upon calculations and predictions based on second-order wave theory. In Chapter 2, the basic principles of linear and second-order theory were presented. A time-saving numerical implementation of the interaction kernels method for calculating second-order bound harmonics was presented. This implementation resulted in a vast reduction in the amount of computation required to calculate the second-order difference waves resulting from a measured linear time series. This in turn, reduced the time required for single calculation from approximately half an hour to under a second. Accuracy of the second-order model was verified and validated using a range of test cases presented in Chapter 2. Firstly, the present method, was compared to the results of other nonlinear wave models; a potential flow model formulated by Bateman et al. [2001] and implemented by Gibbs and Taylor [2005],

and the separation-of-scales method presented in Appendix A. All three methods agreed well under unidirectional conditions, however, for directional conditions the separation-of-scales approach did not agree. Secondly, the model was then used to calculate the second-order difference waves for the linearised Draupner time series. The results compared well to the previous analysis of data by Adcock et al. [2011], providing confidence in the ability of the present implementation to calculate accurately and quickly second-order difference waves. This improved implementation made possible the analysis in Chapter 7.

In Part I experiments were carried out in the FloWave Ocean Research Facility. These experiments investigated the wave-averaged surface elevation of directionally spread and crossing wave groups, and in particular how this can change from negative hole under the group, known as a set-down, to a positive hump or set-up. The formation of a set-up was first investigated for individual directionally spread focused wave groups in Chapter 4. Starting with a unidirectional wave group, where the classical set-down was observed, which may be predicted using a separation-of-scales approach and the simple relation (3.1). As directional spreading was gradually introduced, the magnitude of this set down decreased, approaching zero. Then for degrees of directional spreading $\sigma_\theta^\star \gtrsim 30 - 40°$ the wave averaged surface elevation becomes positive in magnitude, and a set-up began to form. These observations compared very well to predictions made using multi-component second-order theory.

Having successfully reproduced a set-up experimentally, a second series of test, was carried out to measure the spatial structure of individual directionally spread waves. Here, the transition between a set-up and set-down was captured in space, showing the formation of a set-up. From these observations the formation of the set-up was found to be the result of a standing wave localised in space that forms along the direction of propagation. This behaviour is in contrast to that of the

set-down which propagates in space, travelling with and varying on the slow scale of the linear group group.

The set-up produced in Chapter 4 required a large degree of directional spreading, which is unlikely to be experienced ever in extra-tropical storms. However, it is common for extra-tropical storms to occur with separated wind and swell systems. When wind and swell systems travel in different directions crossing wave groups can occur. In Chapter 5 directionally spread crossing focused wave groups were created. Here, groups crossing with an angle of separation greater than $50 - 70°$ exhibited a pronounced set-up in wave-averaged surface elevation. This presents a much more likely scenario for the observation of a pronounced set-up under large or freak waves measured in the oceans. These experimental observations are compared to existing multi-component second-order theory and a modified separation-of-scales approach for crossing wave groups. Excellent agreement was found between multi-component second-order theory and experiments, this was also the case for the separation-of-scales approach when the set-up dominates and the groups were directionally well separated.

The spatial structure of the wave-averaged surface elevation of two crossing wave groups differs significantly from that of a single directionally spread wave group, taking a form which is fast varying in space on the scale of the linear waves as opposed to the group itself.

The experiments detailed in Part I provided further confidence in the ability of the second-order wave model implemented in Chapter 2 to correctly predict wave-averaged surface elevation. In Chapter 7, the model was applied to the North Alwyn dataset as a tool to estimate the degree of directional spreading. Prior to this analysis, the North Alwyn dataset was first subjected to a strict quality control process, as described in Chapter 6. The 'long-wave method' of directional spreading estimation first implemented by Adcock and Taylor [2009],

was then used to estimate the degree of directional spreading for the 20802 time series contained within the North Alwyn dataset that passed the quality control process. The results of this analysis were then compared to the hindcast data of the ECMWF ERA-20C model. This comparison highlighted the sensitivity of the method to measurement errors in the form of sudden changes in slope that were missed by the quality control process. An *a posteriori* method of detecting such errors was presented by screening the results using the expected amplitude of wave-averaged surface elevation for a New Wave group. The indirect nature of this comparison made it difficult to draw conclusions upon the accuracy of the long-wave method on a measurement by measurement basis. However, when observing collections of measurements made during individual storms as a time series, it was possible to gain insight into the effectiveness of the method by calculating the correlation coefficient. A number of storms were presented for which a high degree of correlation was observed, providing confidence that both the hindcast and measurements were capturing the same conditions.

For 391 of the measured records made at the the North Alwyn platform, all three probes were simultaneously of good quality. For these measurements it was possible to estimate the degree of directional spreading using conventional multi-probe methods. This allowed for a direct comparison of methods. A good level of agreement was found between both methods with a slight bias of around 5°. The majority of significant discrepancies stemmed from a single storm. Upon further inspection, it was observed that such discrepancies resulted from crossing directional spectra observed by both the hindcast and frequency independent IMLM spreading estimates. The uncertainty associated with the long wave method was found to be slightly larger but comparable to the multi-probe method. However, a larger number of measurements where multiple concurrent measurements are available is required to fully understand this. The uncertainty was also found to be proportional to the predicted degree of directional spreading.

8.2 Limitations and future work

The present implementation of Dalzell's second-order interaction kernels, provides a significant improvement in computational efficiency. The time saving simplifications are, however, limited to calculations of the second-order terms at the point of measurement. For example to calculate the theoretical difference waves in space, as done in Chapter 3, it was necessary to carry out the full quadruple sum. The analysis of the North Alwyn dataset carried out in Chapter 7, was considerably more time consuming, so that time saving simplifications for a calculations in the time domain at a fixed point in space were of primary concern. Improvement could be made to the numerical implementation detailed in Chapter 2, to reduce the time required for calculations in space. The implementation also assumed frequency-independent spreading, this is not fully representative of real conditions. For the long-wave spreading analysis this assumption reduced the number of variables, and made comparison between methods more straightforward. However, for a situation where more *a priori* information about spreading conditions, or data from a greater number of probes is available, it would be possible to test the method for more representative frequency dependant spreading distributions.

Part I

The experiments undertaken in Chapter 3 successfully captured the formation of the set-up in wave-averaged surface elevation for directionally spread and crossing wave groups. From this foundation, there are several logical extensions. Firstly, a set-up has been demonstrated for somewhat idealised conditions. To understand fully whether a set-up is an indication of freak wave formation owing to crossing

wave groups, irregular waves with crossing groups similar to the simulations carried out by Adcock et al. [2011] should be examined.

When crossing directional spectra are generated in the ocean, they are often the result of separate swell and wind systems. In such cases, it is likely that the wind components will be of higher frequency. It would be informative to test how the interaction of wave groups with different peak frequencies affects the amplitude of the wave-averaged surface elevation.

It is also the case for wind waves in the oceans that directional spreading is a function of frequency, as shown by Ewans [1998] for extra-tropical and by Young [2006] for tropical storms. In both scenarios it is possible to have waves in the tail of the spectrum travelling in different directions to the peak and exhibiting significantly different degrees of directional spreading. The complex, frequency-dependent spectra generated in actual storms will effect the the resulting second-order bound waves. It is therefore, necessary to implement representative frequency dependent spreading distributions, to understand fully the second-order crest height contributions of extreme waves generated in tropical and extra-tropical storms.

Part II

The quality control procedure presented in Chapter 6 is effective in removing the majority of measurement errors. This does, however, come at the cost of potentially discarding significant amounts of data unnecessarily. It is also observed in Chapter 7 that some spurious measurements, that were clearly not artefacts of actual waves, remained undetected. Fundamentally, to avoid either eventuality, some manual inspection is required. This could be improved upon through the use of machine learning in the identification of spurious wave forms.

The long-wave method estimate is shown to be a viable means of approximating the degree of directional spreading for point measurements. This was achieved using Eulerian measurements made by infra-red lasers. A large number of quasi-Lagrangian wave measurement instruments exist and a number are installed in the ocean, some of which also record heave pitch and roll allowing for directional spreading estimation. This may present an opportunity to address the uncertainty of the long-wave method as here there are potentially two direct means of estimating spreading. It is however, uncertain if a quasi-Lagrangian device will capture the second-order harmonics [Longuet-Higgins, 1986]. Therefore, in order to achieve this such devices may require accompanying Eulerian measurements. Alternatively Eulerian measurement paired with a device such as an acoustic Doppler velocitmeter would also allow direct measurement of the directional spectrum.

Having estimated the spreading of measurements without freak waves, and increased confidence in the effectiveness of the long wave method, measurements from the North Alwyn that do contain freak waves should be analysed. Performing the foregoing analysis may allow for the identification of freak waves that have formed as a result of the crossing of wave groups as presented by Adcock et al. [2011] for the Draupner wave.

Appendix A

Derivations

A.0.1 Governing equations

A three-dimensional body of water of depth d and indefinite lateral extent is assumed with a coordinate system (x,y,z), where x and y denote the horizontal coordinates, and z the vertical coordinate measured from the undisturbed water level upwards. Inviscid, incompressible and irrotational flow is assumed and, as a result, the velocity vector can be defined as the gradient of the velocity potential $\mathbf{u} = \nabla\phi$. The governing equation within the domain of the fluid is then Laplace:

$$\nabla^2\phi = 0 \quad \text{for } -d \leq z \leq \eta(x, y, t), \tag{A.1}$$

where $\eta(x, y, t)$ denotes the free surface. The kinematic and dynamic free surface boundary conditions are, respectively:

$$w - \frac{\partial\eta}{\partial t} - u\frac{\partial\eta}{\partial x} - v\frac{\partial\eta}{\partial y} = 0, \quad g\eta + \frac{\partial\phi}{\partial t} + \frac{1}{2}|\nabla\phi|^2 = 0 \quad \text{at } z = \eta(x, y, t), \tag{A.2}$$

where gravity g acts in the negative z direction and $|\nabla\phi|^2 = u^2+v^2+w^2$. Finally, there is a no-flow bottom boundary condition requiring that $\partial\phi/\partial z = 0$ at $z = -d$. By retaining up to quadratic terms in the amplitude of the waves, the two free surface boundary conditions in (A.2) can be combined into two forcing equations for the mean flow and the wave-averaged free surface, respectively:

$$\left(\frac{\partial}{\partial z}+\frac{1}{g}\frac{\partial^2}{\partial t^2}\right)\phi_-^{(2)}\Big|_{z=0} = \overline{\nabla_{\mathrm{H}}\cdot\left(\mathbf{u}_{\mathrm{H}}^{(1)}\big|_{z=0}\eta^{(1)}\right)-\frac{1}{g}\frac{\partial}{\partial t}\Big(\frac{\partial^2\phi^{(1)}}{\partial z\partial t}\Big|_{z=0}\eta^{(1)}+\frac{1}{2}|\nabla\phi|^2_{z=0}\Big)}, \tag{A.3}$$

$$\eta_-^{(2)} = \frac{-1}{g}\left(\frac{\partial\phi_-^{(2)}}{\partial t}\Big|_{z=0}+\overline{\Big(\frac{\partial^2\phi^{(1)}}{\partial z\partial t}\Big|_{z=0}\eta^{(1)}+\frac{1}{2}|\nabla\phi|^2\big|_{z=0}\Big)}\right), \tag{A.4}$$

where the superscripts denote the order in amplitude and the subscripts signify that we only retain wave-averaged terms here, as also indicated by the overlines on the right hand side. We specify our definition of wave-averaging below. Finally, the subscript H denotes horizontal components only.

A.0.2 A single narrowly spread wave group: set-down

We first consider a single wave group travelling in the positive x-direction, which has the linear signal:

$$\eta^{(1)} \overset{\mathrm{Re}}{=} A(X,Y)e^{\imath(k_0x-\omega_0t)}, \quad \phi^{(1)} \overset{\mathrm{Re}}{=} -\imath\frac{\omega_0}{k_0}A(X,Y)e^{k_0z+\imath(k_0x-\omega_0t)}, \tag{A.5}$$

where we have assumed the linear wave travels in deep water ($k_0d \gg 1$). The linear dispersion relationship becomes $\omega_0^2 = gk_0$, and the pre-factor on $\phi^{(1)}$ has been chosen so that the linearized boundary conditions (A.2) are satisfied. To leading-order in the multiple-scales parameter $\epsilon_x \equiv 1/(k_0\sigma_x)$, with σ_x denoting the characteristic spatial scale of the group in its direction of propagation, the group is a function of the slow variables: $X \equiv \epsilon_x\big(x - c_{g,0}t\big)$ and $Y \equiv \epsilon_y y$, where $c_{g,0} = d\omega_0/dk_0 = \omega_0/(2k_0)$ is the group velocity. We define $\epsilon_y \equiv 1/(k_0\sigma_y)$ and set

$O(\epsilon_y) = O(\epsilon_x)$ or smaller, where $\epsilon_y = \epsilon_x$ corresponds to a round envelope ($\sigma_y = \sigma_x$) and $\epsilon_y \to 0$ to a long-crested or unidirectional wave group. By transforming into the reference frame of the group, neglecting the higher-order (in ϵ_x) double time derivative on the left hand side of (A.3) and substituting the linear solutions (A.5) on the right hand side, the mean flow forcing equation (A.3) becomes (cf. Dysthe [1979]):

$$\frac{\partial \phi_-^{(2)}}{\partial z}\Big|_{z=0} = \frac{1}{2}\omega_0 \epsilon_x \partial_X |A|^2, \tag{A.6}$$

where only the divergence of the Stokes transport $\overline{\nabla_{\mathrm{H}} \cdot \left(\mathbf{u}_{\mathrm{H}}^{(1)}(z=0)\eta^{(1)}\right)}$ on the right hand side of (A.3) contributes for deep water ($k_0 d \gg 1$) and the small degree of directional spreading captured by the slow variation of the envelope in the direction normal to propagation (Y). For quasi-monochromatic wave groups, the problem is steady, and the return flow is simply the irrotational and incompressible response to the divergence of the Stokes transport (cf. 'Stokes pumping') in the reference frame of the group, as is well known (see van den Bremer and Taylor [2016] for a discussion of the generally small effects of dispersion and a comparison of the multiple-scales solution with the original solution of Longuet-Higgins and Stewart [1962]). Solving the Laplace equation $\nabla^2 \phi_-^{(2)} = 0$, subject to the bottom boundary condition and the forcing equation (A.6) in Fourier-space, gives (cf. van den Bremer and Taylor [2015]):

$$\phi_-^{(2)} = \frac{\imath \omega_0 |a_0|^2 \sigma_x \sigma_y}{8\pi} \int_{-\infty}^{\infty}\int_{-\infty}^{\infty} \frac{\kappa \cosh\left(\sqrt{\kappa^2+\lambda^2}(z+d)\right)}{\sqrt{\kappa^2+\lambda^2}\sinh\left(\sqrt{\kappa^2+\lambda^2}d\right)} e^{-(\kappa\sigma_x)^2/4-(\lambda\sigma_y)^2/4} e^{\imath(\kappa\tilde{x}+\lambda\tilde{y})} d\kappa d\lambda, \tag{A.7}$$

where we have chosen a Gaussian envelope, $A = a_0 \exp(-\tilde{x}^2/(2\sigma_x^2) - \tilde{y}^2/(2\sigma_y^2))$ with $\tilde{x} = x - c_{g,0}t$ and $\tilde{y} = y$, for illustrative purposes. Turning to the wave-averaged surface forcing equation (A.4), it can be shown by substituting the linear solutions (A.5) on the right hand side that for a single wave group in deep water ($k_0 d \gg 1$) only the mean flow term $(-(1/g)\partial\phi_-^{(2)}/\partial t)$ makes a non-zero contribution. Transforming into the group reference frame and substituting

(A.7), equation (A.4) becomes:

$$\eta_-^{(2)} = \frac{-|a_0|^2\sigma_x\sigma_y}{16\pi}\int_{-\infty}^{\infty}\int_{-\infty}^{\infty}\frac{\kappa^2}{\sqrt{\kappa^2+\lambda^2}\tanh\left(\sqrt{\kappa^2+\lambda^2}d\right)}e^{-(\kappa\sigma_x)^2/4-(\lambda\sigma_y)^2/4}e^{\imath(\kappa\tilde{x}+\lambda\tilde{y})}d\kappa d\lambda. \tag{A.8}$$

If we we further assume $d/\sigma_x \ll 1$, namely that the return flow is shallow, equation (A.8) simplifies to:

$$\eta_-^{(2)} = \frac{-|a_0|^2\sigma_x\sigma_y}{16\pi d}\int_{-\infty}^{\infty}\int_{-\infty}^{\infty}\frac{\kappa^2}{\kappa^2+\lambda^2}e^{-(\kappa\sigma_x)^2/4-(\lambda\sigma_y)^2/4}e^{\imath(\kappa\tilde{x}+\lambda\tilde{y})}d\kappa d\lambda, \tag{A.9}$$

In the limit of a long-crested or unidirectional wave group $R \equiv \sigma_x/\sigma_y \to 0$, we can recover (3.1), which in turn corresponds to the well-known result by Longuet-Higgins and Stewart [1964] ((16), p. 549) resulting from horizontal gradients in radiation stresses. It is evident that in this limit ($R \to 0$ and $d/\sigma_x \ll 1$), the wave-averaged set-down inherits the spatial structure and shape of the wave group. For a non-shallow return flow ($d/\sigma_x = O(1)$), the set-down is accompanied by two positive humps in front and behind, as is evident from the black lines in figure A.1a. For directionally spread groups, these humps are generally larger and the set-down less deep, as is illustrated by the comparing the continuous and dashed lines in this figure. For arbitrary wave group aspect ratio, the integral (A.9) can be explicitly evaluated at the centre of the group:

$$\eta_-^{(2)}(\tilde{x}=0,\hat{y}=0) = \frac{-|a_0|^2}{4d}\frac{1}{1+R} \quad \text{with} \quad R \equiv \frac{\sigma_x}{\sigma_y}. \tag{A.10}$$

It is evident then from (A.10) that the magnitude of the set-down of the wave-averaged free surface reduces for more directionally spread groups. This results from a reduction of the magnitude of return flow straight underneath the group, as the response to the 'Stokes pumping' can now not only return below, but also around the group, a phenomenon more generally known as "remote-recoil" in wave-mean flow interaction theory Bühler and McIntyre [2003]. Related to this,

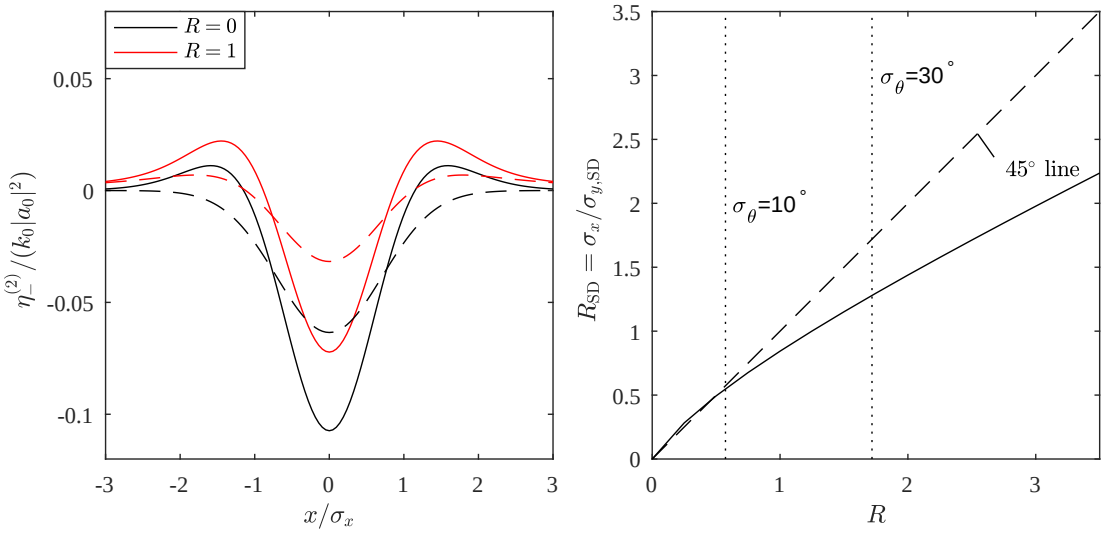

Figure A.1. Various theoretical aspects of the wave-averaged free surface: (a) set-down profile for a single wave group, showing the set-down for $d/\sigma_x = 1.2 = O(1)$ (continuous lines) and in the shallow return flow limit $d/\sigma_x \to 0$ (dashed line); (b) aspect ratio of the wave-averaged free surface R_{SD} as a function of the aspect ratio of the group for a single group R.

figure A.1b illustrates the aspect ratio of the wave-averaged set-down computed from (A.9) as a function of the aspect ratio of the group itself $R = \sigma_x/\sigma_y$, demonstrating that the set-down in generally wider than the group.

A.0.3 Two crossing groups: set-up and set-down

We now consider two quasi-monochromatic wave groups that cross at $x = y = 0$ (at $t = 0$): group 1 with envelope A_1 travelling in the positive x-direction and group 2 with envelope A_2 travelling at an angle $\Delta\theta$, with $\Delta\theta$ measured anti-clockwise from the positive x-axis. For simplicity, we assume the two groups are entirely equivalent with the exception of their amplitudes and directions of travel, and have for the linear surface elevation:

$$\eta^{(1)} \overset{\mathrm{Re}}{=} A_1(X_1, Y_1)e^{\imath(k_0 x - \omega_0 t)} + A_2(X_2, Y_2)e^{\imath(k_0 x\cos(\Delta\theta) + k_0 y\sin(\Delta\theta) - \omega_0 t)}, \qquad \text{(A.11)}$$

where group 1 is a function of the slow scales $X_1 = \epsilon_x(x - c_{g,0}t)$ and $Y_1 = \epsilon_y y$ and group 2 of $X_2 = \epsilon_x(x\cos(\Delta\theta) + y\sin(\Delta\theta) - c_{g,0}t)$ and $Y_1 = \epsilon_y(-x\sin(\Delta\theta) + y\cos(\Delta\theta))$, so that X_1 and X_2 are in the direction of propagation of their respective groups. Substitution of (A.11) and its velocity potential counterpart $\phi^{(1)}$ into the mean flow forcing equation (A.3) gives after some manipulation and to leading-order in the multiple-scales parameter ϵ_x:

$$\frac{\partial \phi_-^{(2)}}{\partial z}\Big|_{z=0} = \underbrace{F_{\text{A1A1}} + F_{\text{A2A2}} + F_{\text{A1A2}}}_{\equiv\, F}, \tag{A.12}$$

where the forcing is provided by the divergence of the Stokes transport of group 1 $A_1 = |A_1|\exp(\imath\varphi_1)$ (F_{A1A1}), group 2 $A_2 = |A_1|\exp(i\varphi_2)$ (F_{A2A2}) and their interaction (F_{A1A2}):

$$\begin{aligned}
F_{\text{A1A1}} =& \frac{1}{2}\omega_0\epsilon_x\partial_{X_1}|A_1|^2,\\
F_{\text{A2A2}} =& \frac{1}{2}\omega_0\epsilon_x\partial_{X_2}|A_2|^2,\\
F_{\text{A1A2}} =& \frac{1}{2}\omega_0\Bigg(\frac{\epsilon_x\big(1+3\cos(\Delta\theta)\big)}{2}\Big(|A_1|_{X_1}|A_2| + |A_1||A_2|_{X_2}\Big) + \epsilon_y\sin(\Delta\theta)\Big(|A_1|_{Y_1}|A_2| - |A_1||A_2|_{Y_2}\Big)\\
&\cos\big(k_0x(1-\cos(\Delta\theta)) - k_0y\sin(\Delta\theta) + \varphi_1 - \varphi_2\big).
\end{aligned} \tag{A.13}$$

The forcing and its response are no longer steady. Avoiding the prohibitively cumbersome Fourier transforms of F_{A1A2}, we immediately assume the return flow is shallow ($d/\sigma_x \ll 1$), so that we can solve the two-dimensional Laplace equation subject to distribution of sources and sinks (A.12-A.13) in physical space:

$$\phi_-^{(2)}(x,y,t) = -\frac{1}{4\pi d}\int_{-\infty}^{\infty}\int_{-\infty}^{\infty} F(x^*,y^*,t)\log\Big((x-x^*)^2 + (y-y^*)^2\Big)dx^*dy^*. \tag{A.14}$$

It can readily be shown that for $\Delta\theta = 0$, (A.14) reduces to the mean flow of a single group (A.7) with $A = A_1 + A_2$. Turning to its forcing equation (A.4), we

decompose the wave-averaged surface elevation into a set-down η_{SD} and a set-up η_{SU}:

$$\eta_{-}^{(2)} = \underbrace{\eta_{\mathrm{SD,A1A1}} + \eta_{\mathrm{SD,A2A2}} + \eta_{\mathrm{SD,A1A2}}}_{=\eta_{\mathrm{SD}}} + \eta_{\mathrm{SU}}. \tag{A.15}$$

The set-down arises purely in response to the return flow (i.e. through $-(1/g)\partial\phi_{-}^{(2)}/\partial t$ in (A.4)) and can be decomposed into three terms corresponding to the three forcing terms in (A.13). Corresponding to F_{A1A1}, we have after transforming into the reference frame of group 1:

$$\eta_{\mathrm{SD,A1A1}}(\tilde{x}_1,\tilde{y}_1) = \frac{|a_1|^2}{4d}\frac{1}{\pi\sigma_x^2}\int_{-\infty}^{\infty}\int_{-\infty}^{\infty}\frac{e^{-(\tilde{x}_1^*)^2/\sigma_x^2-(\tilde{y}_1^*)^2/\sigma_y^2}\tilde{x}_1^*(\tilde{x}_1-\tilde{x}_1^*)}{(\tilde{x}_1-\tilde{x}_1^*)^2+(\tilde{y}_1-\tilde{y}_1^*)^2}d\tilde{x}_1^*d\tilde{y}_1^*, \tag{A.16}$$

where we have assumed a Gaussian envelope as before, $A_1 = a_1\exp(-\tilde{x}_1^2/(2\sigma_x^2) - \tilde{y}_1^2/(2\sigma_y^2))$ with $a_1 = |a_1|\exp(\imath\varphi_1)$, $\tilde{x}_1 = x - c_{g,0}t$ and $\tilde{y}_1 = y$. By replacing ($\tilde{x}_1$,$\tilde{y}_1$) with ($\tilde{x}_2$,$\tilde{y}_2$) and $|a_1|^2$ by $|a_2|^2$, we can find an equivalent expression for the set-down $\eta_{\mathrm{SD,A2A2}}$ associated with group 2. Although the set-downs for the two individual groups are steady in their respective reference frames, their interaction is unsteady, and we have:

$$\eta_{\mathrm{SD,A1A2}}(\tilde{x},\tilde{y}) = \frac{1}{4d}\frac{1}{\pi}\int_{-\infty}^{\infty}\int_{-\infty}^{\infty}\frac{1}{g}\frac{\partial F_{\mathrm{A1A2}}(x^*,y^*,t)}{\partial t}\log\Big((x-x^*)^2+(y-y^*)^2\Big)dx^*dy^*, \tag{A.17}$$

where the forcing can be obtained by differentiating F_{A1A2} in (A.13c) with respect to time:

where we use a mix of coordinate systems for notational convenience. Apart from the set-down terms, the two terms on the right hand side of (A.4) give rise to an

additional term, which we will refer to as the set-up:

$$\begin{aligned}\eta_{\text{SU}} &= \frac{-1}{g}\overline{\Big(\frac{\partial^2\phi^{(1)}}{\partial z\partial t}\Big|_{z=0}\eta^{(1)} + \frac{1}{2}|\nabla\phi|^2\big|_{z=0}\Big)} \\ &= \frac{1}{2}(1-\cos(\Delta\theta))k_0|A_1||A_2|\cos\Big(k_0(\underbrace{x\big(1-\cos(\Delta\theta)\big)) - y\sin(\Delta\theta)}_{=\tilde{x}_1-\tilde{x}_2}) + \varphi_1 - \varphi_2\Big).\end{aligned} \tag{A.18}$$

The averaging in the first equation of (A.18) is over the fast time scales only; a standing wave pattern with lines of constant phase at an angle $\Delta\theta/2$ to the x-axis, namely the bisection of the paths of travel of the two groups. It varies rapidly in space and is slowly modulated in time and space by the product of amplitude envelopes of the two groups (see figure 3.5i-l). It is evident from (A.18) that η_{SU} is zero for $\Delta\theta = 0$ and largest when the two groups collide head-on ($\Delta\theta = 180°$). Whether η_{SU} actually manifests itself as a set-up of the wave-averaged free surface at the location of linear focus ($x = y = 0$) depends trivially on the relative phases of the two groups: $\cos(\varphi_1 - \varphi_2)$. It is noteworthy that (provided $k_0 d \gg 1$) the magnitude of the set-up is not a function of the magnitude of the depth relative to the scale of the group, unlike the set-down, which decreases in magnitude with increasing d/σ_x. .

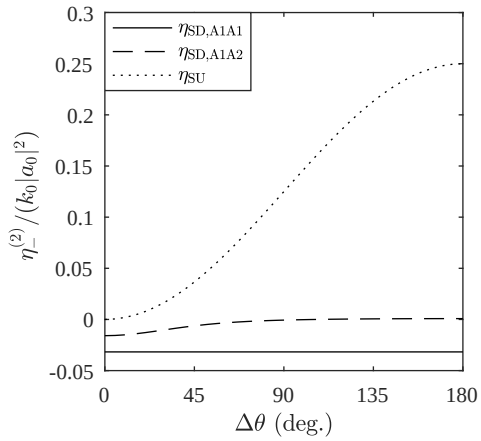

Figure A.2. Different contributions to the total wave-averaged free surface at the focus point and time as a function of the crossing angle $\Delta\theta$ for two in-phase ($mu_1 = \mu_2 = 0$), round ($R = 1$) wave groups ($\epsilon_x = 0.30$ and $d/\sigma_x = 1.2$).

Appendix B

Sum waves

As well as the wave-averaged surface elevation, the second-order super harmonics $\eta_+^{(2)}$ that result from a given set of linear waves may be calculated [Dalzell, 1999]:

$$\eta_+^{(2)} = \sum_{n=1}^{N_\omega}\sum_{m=1}^{N_\omega}\sum_{i=1}^{N_\theta}\sum_{j=1}^{N_\theta} D(\theta_i)D(\theta_j)a_n a_m B^+(\mathbf{k}_{n,i},\mathbf{k}_{m,j},\omega_n,\omega_m,h)\cos\left(\varphi_{n,i}+\varphi_{m,j}\right), \tag{B.1}$$

where the interaction kernel B^+ is given is:

$$\begin{aligned} B^+ = {} & \frac{\omega_n^2+\omega_m^2}{2g} - \frac{\omega_n\omega_m}{2g}\left(1-\frac{\cos(\theta_i-\theta_j)}{\tanh(|\mathbf{k}_{n,i}|h)\tanh(|\mathbf{k}_{m,j}|h)}\right) \\ & \times\left(\frac{\left(\omega_n+\omega_m\right)^2+g|\mathbf{k}_{n,i}+\mathbf{k}_{m,j}|\tanh\left(|\mathbf{k}_{n,i}+\mathbf{k}_{m,j}|h\right)}{C^+\left(\mathbf{k}_{n,i},\mathbf{k}_{m,j},\omega_n,\omega_m,h\right)}\right) \\ & + \frac{\left(\omega_n+\omega_m\right)}{2gC^+\left(\mathbf{k}_{n,i},\mathbf{k}_{m,j},\omega_n,\omega_m,h\right)}\left[\frac{\omega_n^3}{\sinh^2(|\mathbf{k}_{n,i}|h)}+\frac{\omega_m^3}{\sinh^2(|\mathbf{k}_m|h)}\right], \end{aligned} \tag{B.2}$$

with

$$C^+\left(\mathbf{k}_{n,i},\mathbf{k}_{m,j},\omega_n,\omega_m,h\right) = \left(\omega_n+\omega_m\right)^2 - g|\mathbf{k}_{n,i}+\mathbf{k}_{m,j}|\tanh\left(|\mathbf{k}_{n,i}+\mathbf{k}_{m,j}|h\right), \tag{B.3}$$

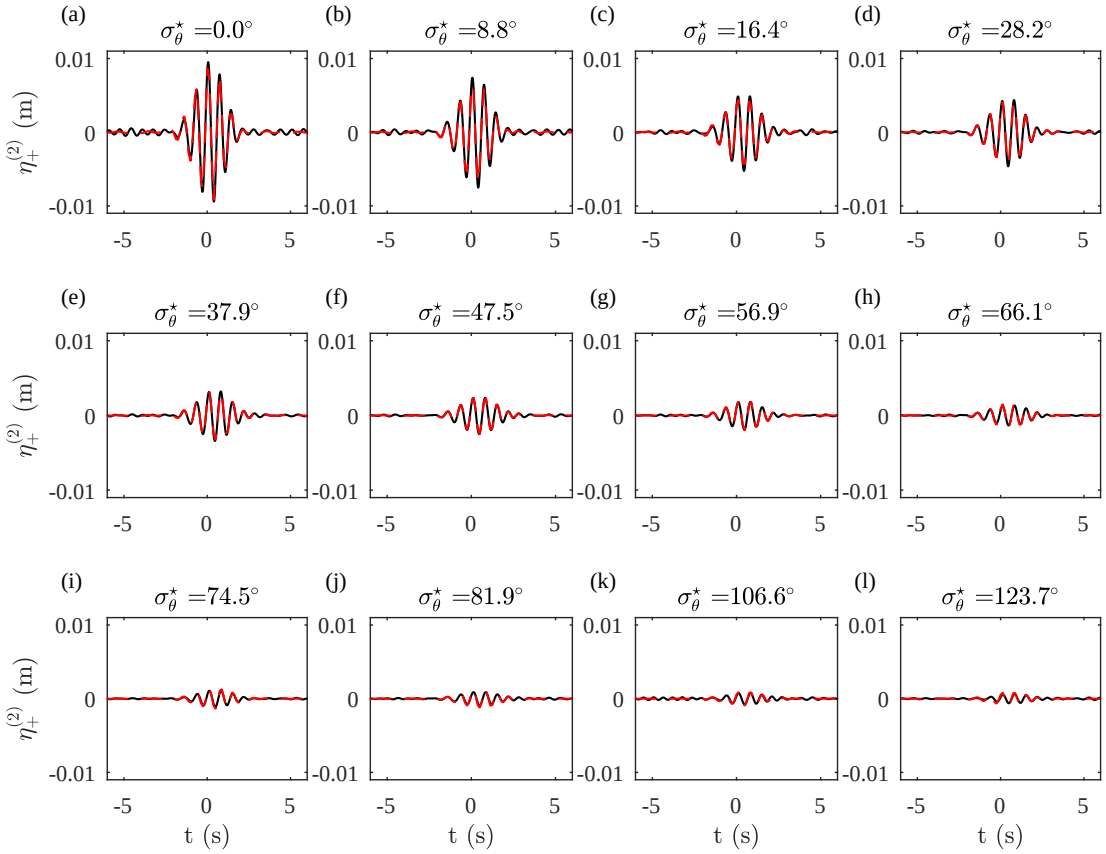

Figure B.1. Second-order sum waves $\eta_+^{(2)}$ at the central probe ($x = 0$, $y = 0$) for the spreading tests (category A), showing measured waves $\eta_{M+}^{(2)}$ (black lines) and theoretical predictions $\eta_{T+}^{(2)}$ (red dashed lines) for input amplitude $a_0 = 0.1$ m. The different panels correspond to increasing degrees of input spreading $\sigma_\theta = 0 - 180°$, and the captions denote the estimated degree of spreading $\sigma_\theta^\star$ used for the theoretical predictions of $\eta_{T+}^{(2)}$.

The time series of measured $\eta_{M+}^{(2)}$ and predicted $\eta_{T+}^{(2)}$ sum waves are compared in figures B.1 to B.3. As with wave-averaged surface elevation presented in Part I, agreement between measurements and theory of second-order sum waves is also very good for all categories of test.

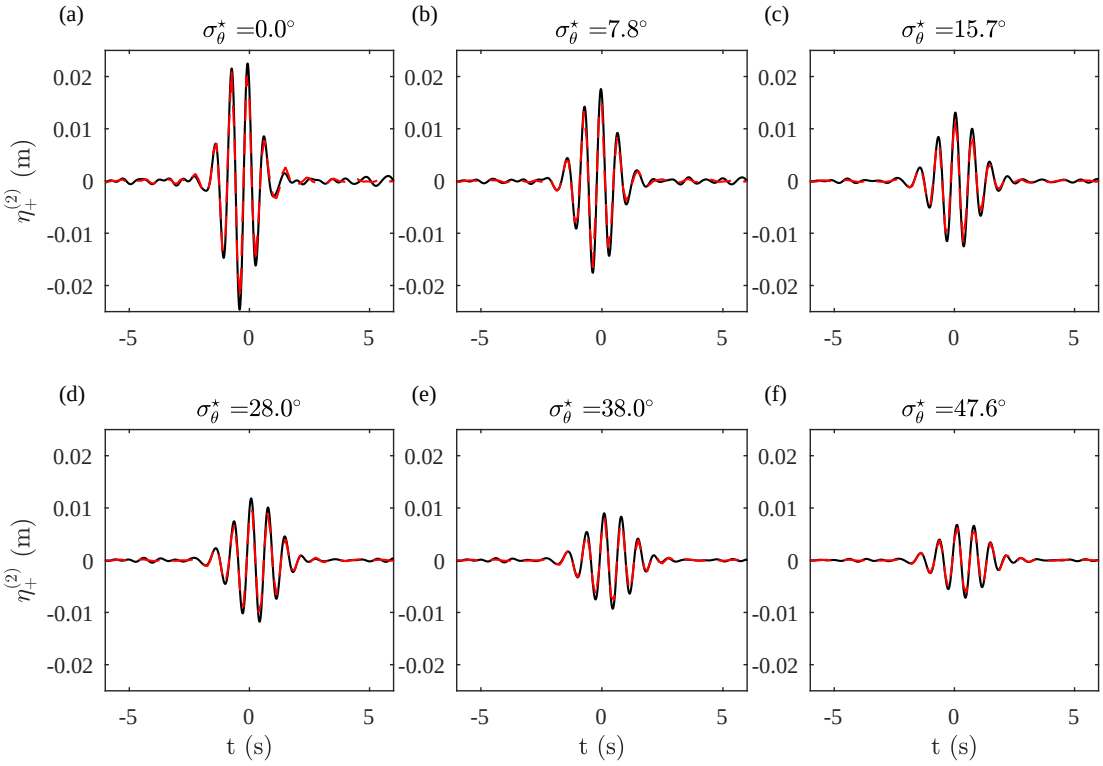

Figure B.2. Second-order sum waves $\eta_+^{(2)}$ at the central probe ($x = 0$, $y = 0$) for the spreading tests (category A), showing measured waves $\eta_{M+}^{(2)}$ (black lines) and theoretical predictions $\eta_{T+}^{(2)}$ (red dashed lines) for linear input amplitude $a_0 = 0.15$ m. The different panels correspond to increasing degrees of input spreading $\sigma_\theta = 0 - 50°$, and the captions denote the estimated degree of spreading $\sigma_\theta^\star$.

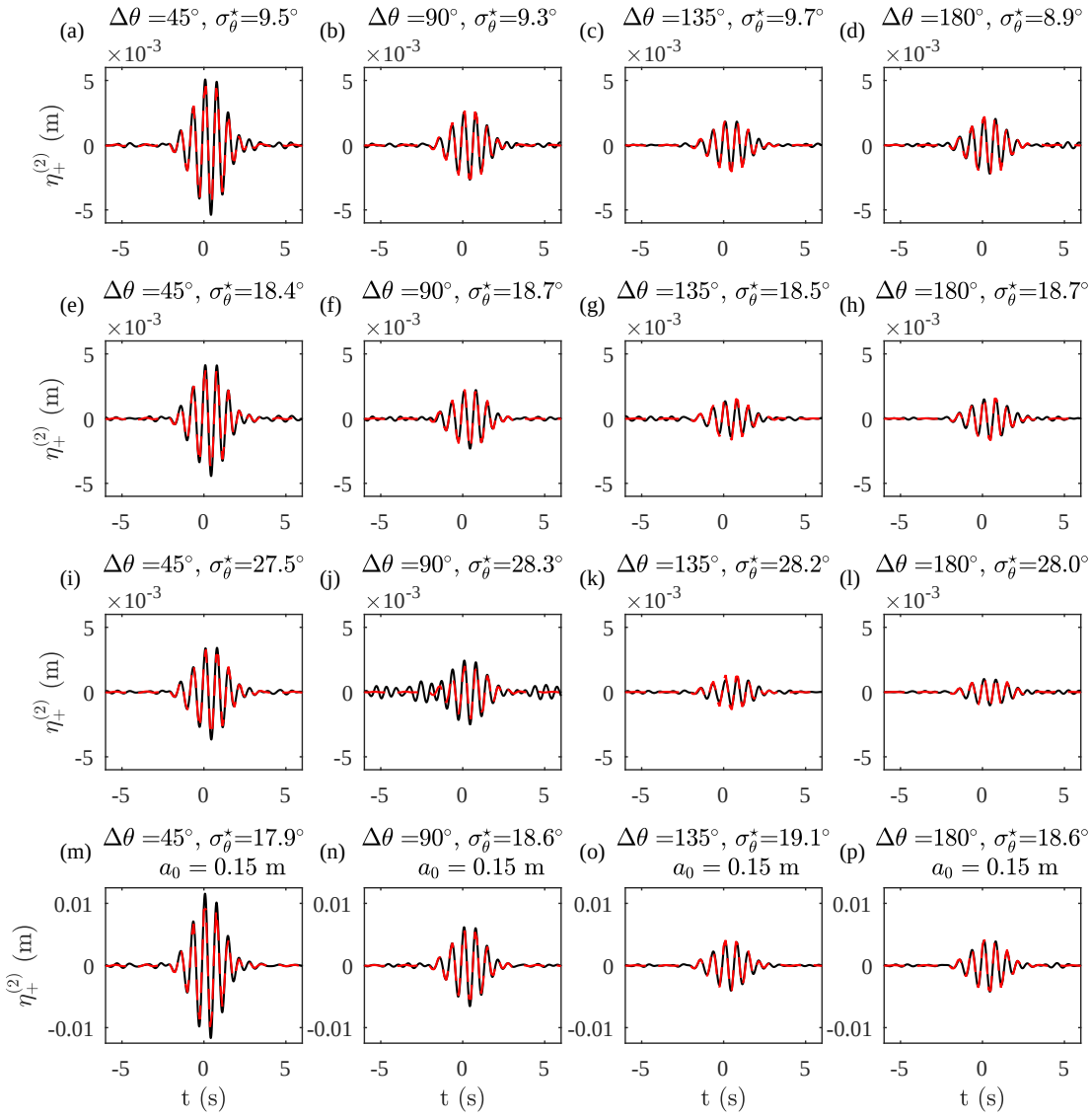

Figure B.3. Second-order sum waves $\eta_+^{(2)}$ at the central probe ($x = 0$, $y = 0$) for the crossing tests (category C), showing measured waves $\eta_{M+}^{(2)}$ (black lines) and theoretical predictions $\eta_{T+}^{(2)}$ (red dashed lines) for input amplitude $a_0 = 0.1$ m. The different panels correspond to increasing values of crossing angle $\Delta\theta = 0-180°$ for degrees of input spreading $\sigma_\theta = 10, 20, 30°$, and the captions denote the estimated degree of spreading $\sigma_\theta^\star$.

Literature references

T.A.A. Adcock and S. Draper. The second-order contribution to wave crest amplitude - random simulations and New Wave. In *The Twenty-fifth International Offshore and Polar Engineering Conference*, 2015.

T.A.A. Adcock and P.H. Taylor. Estimating ocean wave directional spreading from an Eulerian surface elevation time history. *Proc. R. Soc. A*, 465:3361–3381, 2009.

T.A.A. Adcock and P.H. Taylor. The physics of anomalous ('rogue') ocean waves. *Rep. Prog. Phys.*, 465:3361–3381, 2014.

T.A.A. Adcock, P.H. Taylor, S. Yan, Q.W. Ma, and P.A.E.M. Janssen. Did the Draupner wave occur in a crossing sea? *Proc. R. Soc. A*, 467:3004–3021, 2011.

G.B. Airy. *Tides and waves.* London, 1841.

T.E. Baldock, C. Swan, and P.H. Taylor. A laboratory study of nonlinear surface waves on water. *Philos. T. Roy. Soc. A*, 354:649–676, 1996.

S.F. Barstow and T. Kallstad. Field trials of the directional waverider. In *Proceedings of the First International Offshore and Polar Engineering Conference*, pages 55–63, Edinburgh, UK, 1991.

W.J.D. Bateman, C. Swan, and P.H. Taylor. On the efficient numerical simulation of directionally spread surface water waves. *J Comput. Phys.*, 174:277–305, 2001.

T.B. Benjamin and J.E. Feir. The disintegration of wave trains on deep water. *J. Fluid Mech.*, 27:417–430, 1967.

M. Benoit, P. Frigaard, and H.A. Schäffer. Analysing multidirectional wave spectra: a tentative classification of available methods. In *Proceedings IAHR Seminar on Multidirectional Waves and their Interaction whith Structurese*, pages 131–154, San Fancisco, USA, 1997.

J. M. Bland and D. G. Altman. Measuring agreement in method comparison studies. *Stat. Methods in Med. Res.*, 8:135–160, 1999.

O. Bühler and M. E. McIntyre. Remote recoil: a new wave-mean interaction effect. *J. Fluid Mech.*, 492:207–230, 2003.

L. Cavaleri, J.-H.G.M. Alves, F. Ardhuin, A. Babanin, M. Banner, K. Belibassakis, M. Benoit, M. Donelan, J. Groeneweg, T.H.C. Herbers, P. Hwang, P.A.E.M. Janssen, T. Janssen, I.V. Lavrenov, R. Magne, J. Monbaliu, M. Onorato, V. Polnikov, D. Resio, W.E. Rogers, A. Sheremet, J. McKee Smith, H.L. Tolman, G. van Vledder, J. Wolf, and I. Young. Wave modelling–the state of the art. *Prog. Oceanogr.*, 75:603–674, 2007.

L. Cavaleri, L.F. Barbariol, A. Benetazzo, L. Bertotti, J.-R. Bidlot, P.A.E.M Janssen, and N. Wedi. The draupner wave: a fresh look and the emerging view. *J. Geophys. Res.-Oceans*, 128:6061–6075, 2016.

A. Chabchoub, N.P. Hoffmann, and N. Akhmediev. Rogue wave observation in a water wave tank. *Phys. Rev. Lett.*, 106:204502, 2011.

A. Chabchoub, N.P. Hoffmann, M. Onorato, and N. Akhmediev. Super rogue waves: observation of a higher-order breather in water waves. *Phys. Rev. X*, 2: 011015, 2012a.

A. Chabchoub, N.P. Hoffmann, M. Onorato, A. Slunyaev, A. Sergeeva, E. Pelinovsky, and N. Akhmediev. Observation of a hierarchy of up to fifth-order rogue waves in a water tank. *Phys. Rev. E.*, 86:1–6, 2012b.

M. Christou and K. Ewans. Examining a comprehensive dataset containing thousands of freak wave events: Part 1description of the data and quality control procedure. In *ASME 2011 30th International Conference on Ocean, Offshore and Arctic Engineering*, pages 815–826, San Fancisco, USA, 2011. American Society of Mechanical Engineers.

M. Christou and K. Ewans. Field measurements of rogue water waves. *J. Phys. Oceanogr.*, 44:2317–2335, 2014.

A. Cornett, V. Morin, and N. Durand. Model tests to select deck elevations for the PA-B and Lun-A platforms. technical report hyd-ctr-008. 2002.

J.F. Dalzell. A note on finite depth second-order wave–wave interactions. *App. Ocean Res.*, 21:105–111, 1999.

A. Davey and K. Stewartson. On three-dimensional packets of surface waves. *Proc. R. Soc. A*, 338:101–110, 1974.

K.B. Dysthe. Note on a modification to the nonlinear Schrodinger equation for application to deep water waves. *Proc. R. Soc. A*, 369:105–114, 1979.

K.B. Dysthe and H.E. Krogstad P. Müller. Oceanic rogue waves. *Annu. Rev. Fluid Mech.*, 40:287–310, 2008.

R. Eatock Taylor and M.P. Kernot. On second order wave loading and response in irregular seas. *Adv. Coastal Ocean En.*, 5:155–212, 1999.

ECMWF. IFS documentattion Cy40r1 operational implementation, part VII : ECMWF wave model. Technical report, 2016.

W.J. Emery and R.E. Thomson. *Chapter 3 - Statistical Methods and Error Handling*. 2001.

K.C. Ewans. Observations of the directional spectrum of fetch-limited waves. *J. Phys. Oceanogr.*, 28:495–512, 1998.

F. Fedele, J. Brennan, S.P. De León, J. Dudley, and F. Dias. Real world ocean rogue waves explained without the modulational instability. *Scientific Reports*, 6:27715 EP, 2016.

C.J. Fitzgerald, P.H. Taylor, R. Eatock Taylor, J. Grice, and J. Zang. Phase manipulation and the harmonic components of ringing forces on a surface-piercing column. *Proc. R. Soc. A.*, 470:20130847, 2014.

M. Folley and T.J.T. Whittaker. Analysis of the nearshore wave energy resource. *Renew. Energ.*, 34:1709–1715, 2009.

N. Fonseca, C.T. Stansberg, A. Nestegård, A. Bøckmann, and R. Baarholm. The exwave jip: Improved procedures to calculate slowly varying wave drift forces on floating units in extreme seas. In *ASME 2016 35th International Conference on Ocean, Offshore and Arctic Engineering*, pages V001T01A037–V001T01A037, 2016.

G.Z. Forristall. Wave crest distributions: Observations and second-order theory. *J. Phys. Oceanogr.*, 30:1931–1943, 2000.

G.Z. Forristall and K.C. Ewans. Worldwide measurements of directional wave spreading. *J. Atmos. Ocean Tech.*, 15:440–469, 1998.

R.H. Gibbs and P.H. Taylor. Formation of walls of water in fully nonlinear simulations. *App. Ocean Res.*, 27:142–157, 2005.

K. Gunn and C. Stock-Williams. Quantifying the global wave power resource. *Renew. Energ.*, 44:296–304, 2012.

M. Hann, D. Greaves, and A. Raby. A new set of focused wave linear combinations to extract non-linear wave harmonics. In *Twenty-ninth Int. Workshop on Water Waves and Floating Bodies*, pages 61–64, Osaka, Japan, 2014.

K. Hasselmann. On the non-linear energy transfer in a gravity-wave spectrum part 1. general theory. *J. Fluid Mech.*, 12:481–500, 1962.

K. Hasselmann. On the spectral dissipation of ocean waves due to white capping. *Bound.-Lay. Meteorol.*, 6:107–127, 1974.

S. Haver. Evidences of the existence of freak waves. In *Rogue waves 2000*, pages 129–140, Ifremer, Brest, France, 2001.

S. Haver. A possible freak wave event measured at the draupner jacket january 1 1995. In *Rogue waves 2004*, pages 1–8, Ifremer, Brest, France, 2004.

T.H. Herbers, S. Elgar, and R.T. Guza. Infragravity-frequency (0.0050.05 hz) motions on the shelf. part i: Forced waves. *J. Phys. Oceanogr.*, 24:917–927, 1994.

D. Ingram, R. Wallace, A. Robinson, and I. Bryden. The design and commissioning of the first, circular, combined current and wave test basin. *Flow3d. com*, 2014.

T.B. Johannessen and C. Swan. A laboratory study of the focusing of transient and directionally spread surface water waves. *Proc. R. Soc. A*, 457:971–1006, 2001.

C. Kharif and E. Pelinovsky. Physical mechanisms of the rogue wave phenomenon. *Eur. J. Mech. B-Fluid.*, 22:603–634, 2003.

H.E Krogstad. Maximum likelihood estimation of ocean wave spectra from general arrays of wave gauges. *Modelling, Identification and Control*, 1988.

B.M. Lake, H.C. Yuen, H. Rungaldier, and W.E. Ferguson. Nonlinear deep-water waves: theory and experiment. Part 2. Evolution of a continuous wave train. *J. Fluid Mech.*, 83:49–74, 1977.

M. Latheef, C. Swan, and J. Spinneken. A laboratory study of wave crest statistics and the role of directional spreading. volume 473, page 20160290, 2013.

B. Le Méhauté. *An introduction to hydrodynamics and water waves*. Springer-Verlag, New York, 1976.

Michael S Longuet-Higgins. Eulerian and lagrangian aspects of surface waves. *J. .Fluid Mech.*, 173:683–707, 1986.

M.S. Longuet-Higgins. The effect of non-linearities on statistical distributions in the theory of sea waves. *J. Fluid Mech.*, 17:459–480, 1963.

M.S. Longuet-Higgins and R.W. Stewart. Radiation stress and mass transport in gravity waves, with applications to 'surf beats'. *J. Fluid Mech.*, 13:481–504, 1962.

M.S. Longuet-Higgins and R.W. Stewart. Radiation stresses in water waves; a physical discussion, with applications. *Deep-sea Res.*, 2:529–562, 1964.

C. Lopez-Pavon, R.A. Watai, F. Ruggeri, A.N. Simos, and A. Souto-Iglesias. Influence of wave induced second-order forces in semisubmersible fowt mooring design. *J. Off. Mech. Arct.*, 137:031602, 2015.

Y. Ma. The perturbed plane-wave solutions of the cubic Schrödinger equation. *Stud. App. Math.*, 60:43–58, 1979.

P.W. Marshall. Dynamic and fatigue analysis using directional spectra. In *Offshore Technology Conference*, Dallas, Texas, 1976.

M. E. McIntyre. On the wave momentum myth. *J. Fluid Mech.*, 106:331–347, 1981.

H. Mitsuyasu, F. Tasai, T. Suhara, S. Mizuno, M. Ohkusu, T. Honda, and K. Rikiishi. Observations of the directional spectrum of ocean waves using a coverleaf buoy. *J. Phys. Oceanogr.*, 5:750–760, 1975.

J. Oberhagemann and O. El Moctar. Numerical and experimental investigations of whipping and springing of ship structures. In *The Twenty-first International Offshore and Polar Engineering Conference*, 2011.

M. Okihiro, R.T. Guza, and R.J. Seymour. Bound infra-gravity waves. *J. Geophys. Res.*, 97:453–469, 1992.

M. Onorato, L. Cavaleri, S. Fouques, O. Gramstad, P.A.E.M Janssen, J. Monbaliu, A.R. Osborne, C. Pakozdi, M. Serio, and C.T. Stansberg. Statistical properties of mechanically generated surface gravity waves: a laboratory experiment in a three-dimensional wave basin. *J. Fluid Mech.*, 627:235–257, 2009.

M. Onorato, S. Residori, U. Bortolozzo, A. Montina, and F.T. Arecchi. Rogue waves and their generating mechanisms in different physical contexts. *Physics Reports*, 528:47–89, 2013.

S.S Pawka. Island shadows in wave directional spectra. *Journal of Geophysical Research: Oceans*, 88:2579–2591, 1983.

P. Poli, H. Hersbach, D. Tan, D. Dee, J. Thépaut, A. Simmons, C. Peubey, P. Laloyaux, T. Komori, P. Berrisford, R. Dragani, Y. Trémolet, E. Hlm, M. Bonavita, L. Isaksen, and M. Fisher. The data assimilation system and initial performance evaluation of the ECMWF pilot reanalysis of the 20th-century assimilating surface observations only (era-20c). *ERA report series*, 14, 2013.

W. Rosenthal and S. Lehner. Rogue waves: Results of the maxwave project. *J. Offshore Mech. Arct.*, 130:21006, 2008.

H. Santo, P. H. Taylor, R. Eatock Taylor, and Y. S. Choo. Average properties of the largest waves in hurricane camille. *J. Offshore Mech. Arct.*, 135:0116021–0116027, 2013.

T. Sawaragi. *Coastal engineering-waves, beaches, wave-structure interactions*, volume 78. 1995.

J.N. Sharma and R.G. Dean. Second-order directional seas and associated wave forces. *Soc. Petrol. Eng. J.*, 21:129–140, 1981.

G.G. Stokes. On the theory of oscillatory waves. *Trans. Camb. Philos. Soc.*, 8: 441–455, 1847.

T.M.A. Taklo, K. Trulsen, H.E. Krogstad, and J.C.N Borge. On dispersion of directional surface gravity waves. *J. Fluid Mech.*, 812:681–697, 2017.

H.J. Thiébaux. *Statistical Data Analysis for Ocean and Atmospheric Sciences*. Elsevier, 2013.

Z. Tian, M. Perlin, and W. Choi. Frequency spectra evolution of two-dimensional focusing wave groups in finite depth water. *J. Fluid Mech.*, 688:169–194, 2011.

A. Toffoli, M. Onorato, and J. Monbaliu. Wave statistics in unimodal and bimodal seas from a second-order model. *Eur. J. Mech. B-Fluid.*, 25(5):649–661, 2006.

A. Toffoli, J. Monbaliu, M. Onorato, A.R. Osborne, A.V. Babanin, and E.M. Bitner-Gregersen. Second-order theory and setup in surface gravity waves: a comparison with experimental data. *J. Phys. Oceanogr.*, 37:2726–2739, 2007.

A. Toffoli, O. Gramstad, K. Trulsen J. Monbaliu, E.M. Bitner-Gregersen, and M. Onorato. Evolution of weakly nonlinear random directional waves: laboratory experiments and numerical simulations. *J. Fluid Mech.*, 664:313–336, 2010.

A. Toffoli, E.M. Bitner-Gregersen, A.R. Osborne, M. Serio, J. Monbaliu, and M. Onorato. Extreme waves in random crossing seas: Laboratory experiments and numerical simulations. *Geophys. Res. Lett.*, 38:L06605, 2011.

P. S. Tromans, A.R. Anatruk, and P. Hagemeijer. New model for the kinematics of large ocean waves application as a design wave. In *The First International Offshore and Polar Engineering Conference*. International Society of Offshore and Polar Engineers, 1991.

T. S. van den Bremer and P. H. Taylor. Estimates of Lagrangian transport by wave groups: the effects of finite depth and directionality. *J. Geophys. Res.*, 120(4):2701–2722, 2015.

T.S. van den Bremer. *The induced mean flow of surface, internal and interfacial gravity wave groups.* PhD thesis, University of Oxford, 2014.

T.S. van den Bremer and P. H. Taylor. Lagrangian transport for two-dimensional deep-water surface gravity wave groups. *Proc. R. Soc. A*, 472(20160159), 2016.

D.A.G Walker, P.H. Taylor, and R. Eatock Taylor. The shape of large surface waves on the open sea and the Draupner new year wave. *App. Ocean Res.*, 26: 73–83, 2004.

E. J. Walsh, D. W. Hancock III, D. E. Hines, R. N. Swift, and J. F. Scott. Directional wave spectra measured with the surface contour radar. *J. Phys. Oceanogr.*, 15:566–592, 1985.

J. Wolfram, G. Feld, and J. Allen. A new approach to estimating environmental loading using joint probabilities. In *7th International Conference on Behavior of Offshore Structures*, pages 701–704, Boston, USA, 1994. Pergamon.

T.R. Young. Directional spectra of hurricane wind waves. *J. Geophys. Res. Oceans*, 111, 2006.